F. I. Kaya

I give permission for public access to my thesis for any copying to be done at the discretion of the archives librarian and/or the College librarian.

FIK, 28 Dec 2015

F. I. Kaya

Thesis: Simulations on Ferromagnetic Nanostructures

Fikriye Idil Kaya[1]

Department of Physics, Mount Holyoke College, South Hadley, MA, 01075,

USA

(Dated: 28 Dec 2015)

F. I. Kaya

ABSTRACT

Understanding domain wall (DW) motion in ferromagnetic nanostructures is crucial for realizing proposed magnetic data storage and logic devices. Simulations offer time-wise and cost-wise efficiency when testing theories of magnetism, which structure the nucleation, movement, and annihilation of DWs. During my work with the Aidala Group as summarized by this thesis, we have explored two topics: One constituted the effects of curvature on DW motion in elliptical nanorings, and the other did the nucleation of 360° DWs in a wire by using a local circular field.

In this thesis, we investigate the effects of curvature on DW pinning and motion by studying elliptical rings via micromagnetic simulations.[1] Elliptical rings with constant width have varying curvature: The minor axis has the lowest curvature and the major the greatest. We can nucleate DWs anywhere along the ellipse by applying the appropriate uniform magnetic field. However, DWs do not pin at all locations along the ellipse once the field is removed. We study the pining and depinning of DWs by applying a slowly increasing elliptical magnetic field to determine the magnitude of the field at which DWs begin to move. By varying the major to minor axis ratio, we examine the effects of curvature on DW pinning: A larger field is requisite for moving DWs in regions of higher curvature (near the major axis) than that for lower curvature (near the minor axis). Overall, increasing the major to minor axis ratio of elliptical nanorings requires an increasing field strength to depin the DWs along the major axis.

Furthermore, our simulations demonstrate the feasibility of nucleating a 360° DW at a specific location along a ferromagnetic wire by applying a local circular field that is cen-

tered in close proximity to the wire. We simulate the field strength as if from a current carrying wire, which we can experimentally realize by passing current through the tip of an AFM.[2] The successful nucleation of a 360° DW depends on the dimensions of the ferromagnet, on the strength of the circular field, and on the distance of the center of the field from the wire. Once a 360° is nucleated, its position shifts with time. We use notches to pin the 360° DWs. We explore the optimal size and spacing of notches that allow the greatest packing density with control over the nucleation and annihilation of individual DWs.

Thesis Supervisor: Katherine E. Aidala (Associate Professor of Physics;

Department of Physics, Mount Holyoke College, South Hadley, MA, 01075, USA)

F. I. Kaya

ACKNOWLEDGEMENTS

F. I. Kaya

CONTENTS

F. I. Kaya

F. I. Kaya

Appendix A: Complementary Energy Formulations

I. DERIVATIONS OF ZEEMAN, EXCHANGE, AND MAGNETOSTATIC ENERGIES

2

F. I. Kaya

Appendix B: The Angle Finder

Appendix C: The Curvature Finder

Appendix D: The Energy Finder

F. I. Kaya

I. INTRODUCTION

On the look for perfection in data storage, experts have been searching for a non-volatile, fast, and cheap data storage device. Non-volatility is needed for stored data to not disappear when we turn the computer off. Speed becomes handy when we want to store, retrieve, or move large amounts of data. In addition, we want everything to be as cheap as possible without cutting down on quality.

We seek magnetic data storage as an alternative to the Static or the Dynamic Random Access Memory (SRAM or DRAM) and to the commercially available solid state drives. The SRAM and DRAM are fast since they can retrieve data from storage *randomly*, meaning without reading through the entire stored data to find the intended piece of information. They are considerably cheap and are already in the market as parts of most personal computers. However, they are volatile; they need a constant supply of power to store data, so when we turn the computer off, the data eventually disappear. On the other hand, solid state drives available to public are fast and non-volatile, but they are expensive.

We deem magnetic storage promising to become *optimal*, meaning non-volatile, fast, and relatively cheap, given today's technology. Thus, we study its underlying physics in order to support the engineers or applied scientists of the field with relevant knowledge so that they can realize such an optimal magnetic data storage device.

F. I. Kaya

A. Properties of Ferromagnets

In this section we portray the basics of ferromagnets. The ferromagnetic properties relate to a myriad of physical phenomena including the magnetic moment, energy dynamics, domain wall (DW) formation, magnetic fields, and hysteresis; all of which we are to elucidate. Then we present two introductory sections, on the nucleation of $360°$ DWs and on curvature, in order to familiarize the reader with the concepts, which we will handle in detail in the following chapters. Furthermore, we describe the basics of micromagnetic simulations we used to obtain the data that we convey in this thesis. Subsequently, we impart a few examples in literature that use DWs to store data.

1. Magnetic dipole moment

The *magnetic dipole moment*, or *magnetic moment*, is a means of measuring the torque that a magnetically polarized body feels in order to align with the effective magnetic field: The greater the magnetic moment is, the greater the torque is on moments under an external field. The magnetic moment can be represented as a dipole between two magnetic charges if they existed.

The net magnetic moment of a material consists of the spin magnetic moment, μ_s, and the orbital magnetic moment, μ_o. μ_s and μ_o relate to the electronic properties of the material. (Specifically, these electronic properties are quantum mechanical, and for a better understanding see Appendix A). We can write the net magnetic moment as

$$\vec{\mu} = \vec{\mu}_s + \vec{\mu}_o \quad .$$

μ_s is associated with the *spin*, or the *spin angular momentum*, of the electrons inside the material such that

$$\vec{\mu}_s = -\frac{e}{m_e}\mathbf{S} \quad ,$$

where $\mathbf{S}$ is the spin, e is the elementary charge $(1.60 \times 10^{19}$ C$)$, and m_e is the mass of an electron $(9.11 \times 10^{-31}$ kg$)$. Replacing $\mathbf{S}$ with its component along a generic u axis, e.g., with S_z along the z-axis, we obtain

$$\mu_{s,u} = -\frac{e}{m_e}S_u = \pm\frac{eh}{4\pi m_e} \quad ,$$

where we let u denote the single axis, and h is Planck's constant. The magnitude of $\mu_{s,u}$ is an approximation of the *Bohr magneton*, which, being a dipole measure itself, is the closest magnetic counterpart of an electric charge in the creation of an electric field.

μ_o is associated with the *orbital angular momentum* of the electrons inside the material such that

$$\vec{\mu}_o = -\frac{e}{2m_e}\mathbf{L} \quad ,$$

where $\mathbf{L}$ is the orbital angular momentum, and e and m_e are the elementary charge and the electronic mass with previously stated values.

Hence, the magnetic moment becomes

$$\vec{\mu} = \left(-\frac{e}{m_e}\mathbf{S}\right) + \left(-\frac{e}{2m_e}\mathbf{L}\right) \quad .$$

F. I. Kaya

We represent the sum of magnetic moments (sometimes called *magnetization*, see section I A 3) in a ferromagnet as

$$\mathbf{M} = \frac{\sum \vec{\mu}}{V} \quad ,$$

where V is the volume of the ferromagnet.

2. *Energies and interactions*

The interactions within a ferromagnetic material result in states of the system that minimize the total energy of the system, where we consider the system to be the entirety of the ferromagnetic material. This self-alignment of moments to minimize the total energy is intrinsic of a ferromagnet, both before and after perturbations (e.g., after an external field is applied). We can call this the *principle of energy minimization* (PEM).

The Zeeman Energy (ZE), Exchange Energy (EE), and Magnetostatic Energy (ME) are the principal energy contributions to the Total Energy (TE) of the ferromagnetic system. It costs energy whenever a moment does not align with the external magnetic field, its neighbor, or its boundaries. Taking these contributions into account, the Total Energy is thus

$$E_{tot} = U_{Zee} + U_{exc} + U_{mag} \quad ,$$

where U_{Zee} is the *Zeeman* (or *external field*) *energy*, U_{exc} is the *exchange energy*, and U_{mag} is the *magnetostatic* (or *stray field*) *energy*.

We can rewrite the total energy with the energy terms as integrals over whole space as

$$E_{tot} = \left(-\mu_0 \int \mathbf{H}_{ext} \cdot \mathbf{M} \, d\tau \right) + \left(-\mu_0 \int A \, \mathbf{M} \cdot \mathbf{M} \, d\tau \right) + \left(-\mu_0 \int \frac{1}{2} \mathbf{H}_{mag} \cdot \mathbf{M} \, d\tau \right) \quad ,$$

14

where μ_0 is the permeability of free space, $\mathbf{H}_{ext}$ is the external magnetic field, $\mathbf{M}$ is the sum of magnetic moments, A is the exchange constant with a value depending on material parameters, and $\mathbf{H}_{mag}$ is the magnetostatic field.

Let us inspect each term mathematically: When $\mathbf{H}_{ext}$ and $\mathbf{M}$ lie in parallel, moments align in the direction of the external magnetic field, so the ZE is minimized, since the dot product is maximized and since there is a negative sign. Similarly, the EE is minimized when the two moment integrals lie in parallel, hence when moments align in parallel with the neighboring moments. Lastly, the magnetostatic energy is minimized when $\mathbf{H}_{mag}$ and $\mathbf{M}$ lie in parallel, hence when moments align with the boundaries of the structure. This is because: When moments align with the boundaries of the structure, so do their magnetostatic field contributions, resulting in the moments lying in parallel with the magnetostatic field. (For derivations of ZE, EE, and ME, for other TE contributions, and for our justification of why we ignore these contributions, see Appendix A).

While approaching a total energy minimum, as a consequence of their direction, magnetic moments group in partitions in the magnetic material. These regions, where the local magnetization assumes a maximum value and moments generally point in the same direction, are called *domains*.[3] *Domain walls* (DWs) are regions, where moments diverge with respect to their neighbors (see section I A 5 for details). Fig. 1 depicts a DW separating two domains, where the moments of the first domain mostly point in the opposite direction to the moments of the second domain.

DWs separate domains from one another and by doing so minimize ME. There is lower

F. I. Kaya

FIG. 1. Domains and DW on a ferromagnet. The DW is circled in orange; it separates the first domain pointing in $-\hat{x}$ (blue) from the second domain pointing in $\hat{x}$ (red).

ME cost when moments align with the boundaries of the material, but in some cases (e.g., initialization of an ellipse, see the following case study), DWs form and they cost higher exchange energy. In addition, a cost of ZE arises due to the moments not lining up with the external field. Hence, one needs to consider the trade-off between the exchange, the magnetostatic, and the Zeeman energies. In all cases, moments align themselves in the configuration that results in the minimum total energy.

3. Hysteresis

We can characterize a state by the alignment of its magnetic moments. Ferromagnets innately have their magnetic moments line up with an external magnetic field such that when it is removed the moments relax to a new state of magnetization, under PEM. The new state is either *uniform*, if all moments point in the same direction, or *composite*, if DWs have formed. The starting state of the moments (before the external field) has a role in determining the final state that the moments obtain (after the external field); the external field perturbs the starting state and converts it into the final one. As a defining behavior of the ferromagnets, the moments align themselves with the neighboring moments and with the constraints of the material they are in, having also been influenced by the external magnetic field that was just removed. All these influences define the final state. This final state, also known as the *lowest energy state*, is perpetual such that the moments do not return to one

of the previous states. Since the final state is field-dependent, the material "remembers" the applied external magnetic field after it has been removed. This phenomenon is called *hysteresis* and is the basis of memory devices that embody ferromagnets.

When the external magnetic field is removed, there still exists an internal magnetic field due to the moments within a magnetic material. We refer to this internal magnetic field, which emerges as a result of the external magnetic field, as the *magnetization*, $\mathbf{M}$, of the material. The magnetization relates to the magnetic moment such that $\mathbf{M}$ and $\vec{\mu}$ point in the same direction.

We can write the net magnetic field on the material, $\mathbf{B}_{mat}$, as

$$\mathbf{B}_{mat} = \mathbf{B}_{ext} + \mu_0\mathbf{M} = \mu_0(\mathbf{H}_{ext} + \mathbf{M}) \quad ,$$

where μ_0 is the permeability of free space ($4\pi \times 10^{-7}$ Hm^{-1}), $\mathbf{H}_{ext}$ is the intensity of $\mathbf{B}_{ext}$ at given coordinate of the material, $\mathbf{H}_{ext}$ and $\mathbf{M}$ are in Amperes per meter (Am^{-1}), and $\mathbf{B}_{mat}$ is in Teslas (T).

We can plot the magnetization of a system as a function of the applied magnetic field. Fig. 2 captures such a plot with M as the magnetization of a ferromagnet and H as the externally applied magnetic field.

The plot in Fig. 2 constitutes a *hysteresis loop*, on which we can find the saturation magnetization (at $dM/dH = 0$), the remanent magnetization, and the coercive field at which the magnetization switches direction (at $M = 0$).[4] The *saturation magnetization* is the magnetization the ferromagnet acquires when it is fully saturated by the external field such that
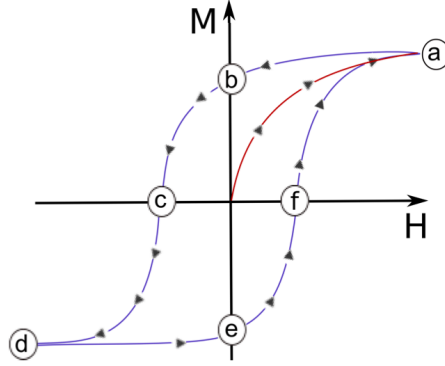
FIG. 2. Hysteresis on a ferromagnet[4] (a) Positive saturation (b) Positive remanent magnetization (c) Negative coercive field (d) Negative saturation (e) Negative remanent magnetization (f) Positive coercive field

all moments align with the field direction. Once the ferromagnet arrives at its saturation magnetization, the field is turned off, and the structure obtains its *remanent magnetization.* For more details, see Licht 2011.[4]

4. Initialization under uniform in-plane field

We need to control our starting state any time we run a simulation, so we always specify how we *initialize* the material: Generally, we apply a uniform in-plane field on a ferromagnet with randomized moments. We initialize our ferromagnets under a uniform in-plane magnetic field set at 800 mT (our default value) or at 160 mT (sufficient to initialize most runs in section 2). Once the external magnetic field saturates the ferromagnet, the field is turned off, and the ferromagnet consequently reaches its remanent magnetization.

A) Dipole state for wires

We initialize our linear ferromagnets under an in-plane field pointing in $-\hat{x}$ (see Fig. 3). Once we remove the field, the moments relax under zero field, and in the end they mostly align in $-\hat{x}$, towards the direction of the prior external field (Fig. 3*c*). This state, on which

the moments in majority point along the long axis, is the typical dipole state, where we can define $-\hat{x}$ as the North pole and $\hat{x}$ as the South.

FIG. 3. Linear ferromagnet initialized in $-\hat{x}$. Red bits correspond to moments pointing in $\hat{x}$ and the blue in $-\hat{x}$.

(a) Initial state: The moments point in random directions. (b) Resulting state after reaching saturation magnetization (under 160 mT). The external field is turned off after this state. (c) Resulting state after reaching remanent magnetization, under zero field

B) Onion state for rings

We initialize our elliptical ferromagnets along $\hat{x}$ (at $\theta = 0°$ in polar coordinates), along $\hat{y}$ (at $\theta = 90°$), or along singular axes (at $\theta = 30°$, $45°$, or $60°$).

Once we turn the field off, the moments relax under zero field. Thereafter, moments in majority align in parallel with the geometric boundaries except where two DWs form (Fig. 4c). This is a consequence of PEM and topology (see next subsection). In the final state (Fig. 4c), two domains have formed: The domain on the left-hand side (LHS) points CW and the domain on the right-hand side (RHS) points CCW.

Let us consider this elliptical ferromagnet as our system, and study the case when we place the system under a strong in-plane magnetic field (800 mT in $\hat{y}$). The plot in Fig. 5 shows

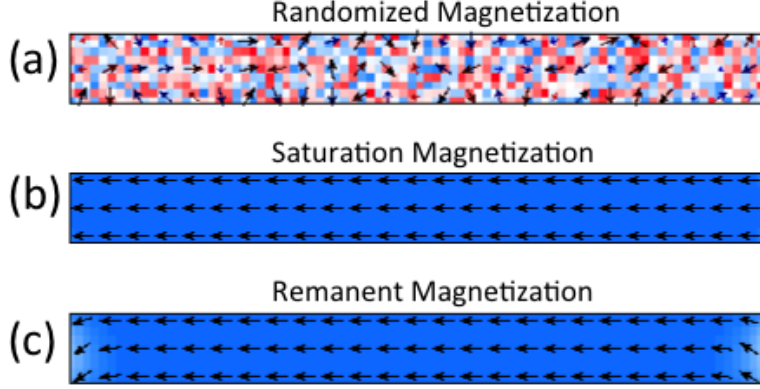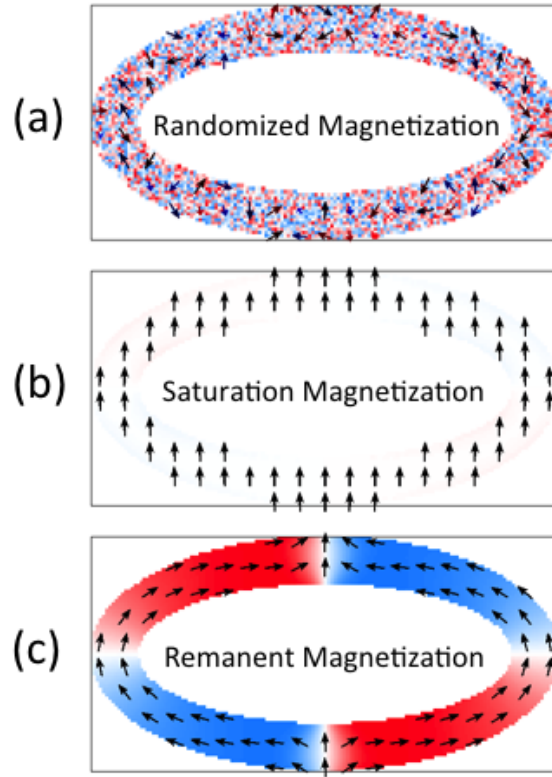**FIG. 4.** Elliptical ferromagnet initialized in $\hat{y}$. Red bits correspond to moments pointing in $\hat{x}$ and the blue in $-\hat{x}$. (a) Initial state, where the moments point in random directions (b) Resulting state after the structure is fully saturated (c) Resulting state after the external field is turned off and the structure has attained its remanent magnetization (see section 1.1.4E)

the change in the energy of the system.

At step 0, which is before the magnetic field is turned on, all moments point in a random direction. Starting with step 1, the magnetic field is on, and the moments feel the torque, as a result begin to rotate, and hence gradually align with the field. Energies drop in this process, and by step 1000, the moments become fully aligned.

Next, the field is turned off as marked in green in Fig. 5. This immediately reduces the Zeeman energy to zero, pulling TE higher (although the graph connects the two points with dashed lines); the system relaxes under zero field until the change in the magnetization of
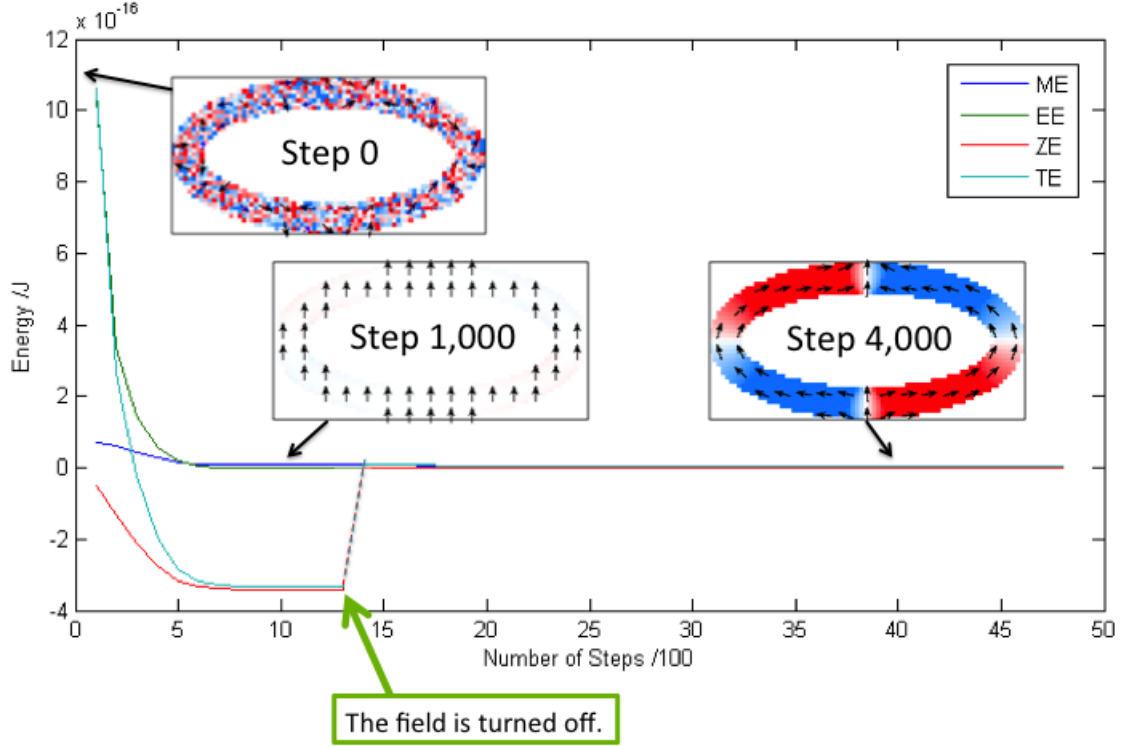
FIG. 5. Plot of energy vs. iteration. ME stands for Magnetostatic Energy, EE for Exchange Energy, ZE for Zeeman Energy, and TE for Total Energy. On the elliptical ferromagnets, the red bits correspond to moments pointing in $\hat{x}$ and the the blue in $-\hat{x}$.

the moments falls under a threshold value ($\frac{dM}{dt} < 0.1$ deg/ns). Meanwhile, moments align themselves with the edges of the ellipse and with their neighbors so that two domain walls are formed. At this point, energies have approached a new minimum under PEM, at a value close to 0 J as in Step 4,000. During the formation of the two DWs, there occurs a decrease in ME and a smaller increase in EE (Fig. 6). As a result, from the point the field is turned off to when DWs have fully formed, TE approaches a minimum. This is the reason why DWs have formed: They minimize the TE of the system in its new state.

Hereafter, the state retains its energies and direction of moments, with trivial changes, until the run ends. The ending state with two DWs is called the *onion state* (Fig 7).
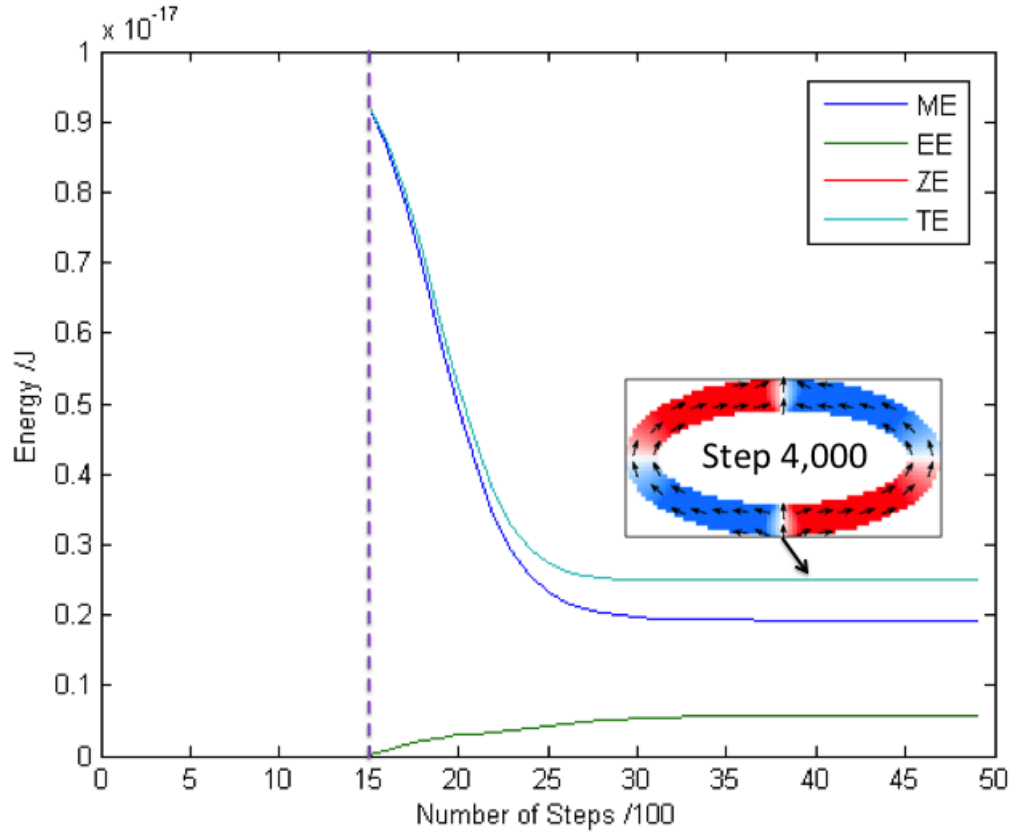
FIG. 6. Plot of energy vs. iteration after Step 1,500 (see Fig. 5). ME stands for Magnetostatic Energy, EE for Exchange Energy, ZE for Zeeman Energy, and TE for Total Energy. On the elliptical ferromagnets, the red bits correspond to moments pointing in $\hat{x}$ and the the blue in $-\hat{x}$.

5. *Domain Walls*

A Domain Wall (DW) is an area on a magnetic structure where the magnetization and hence the moments representing the magnetization change direction. Similar to walls separating rooms, DWs separate domains. We consider two types of DWs: The 180° DW and the 360° DW.

A) 180° **DW and** 360° **DW basics**

In Fig. 8*a* as we move from left to right, each emerging moment has an angle higher than
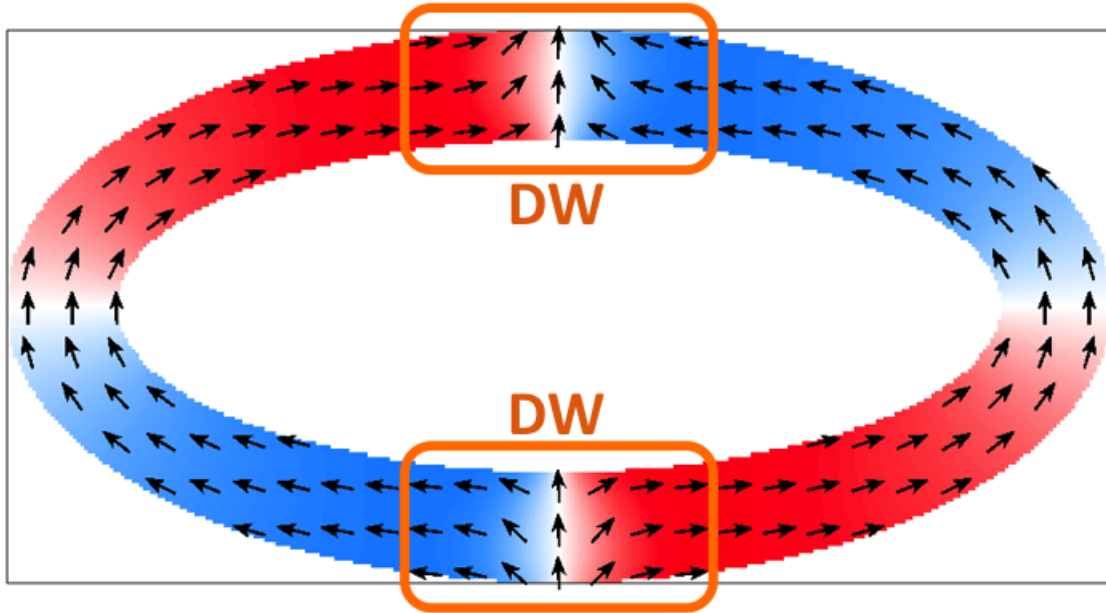
FIG. 7. Onion state of an elliptical ferromagnet. Red bits correspond to moments pointing in $\hat{x}$ and the blue in $-\hat{x}$. Two domain walls separate two domains: The domain on the left half of the figure has moments rotating CW; the domain on the right half of the figure has moments rotating CCW.
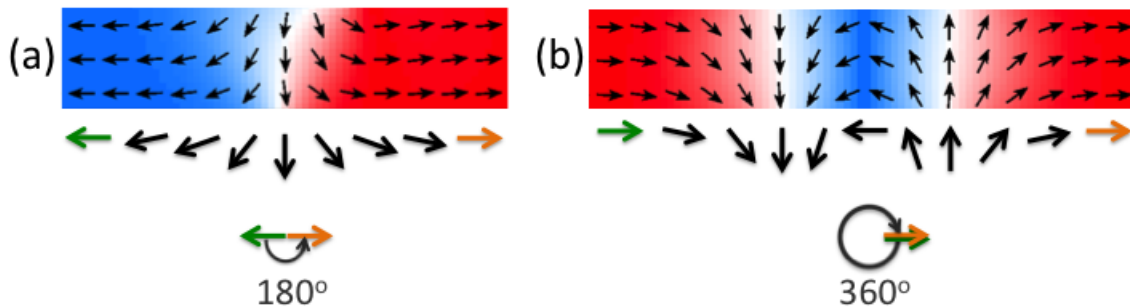
FIG. 8. Types of DWs on a nanowire. Red bits correspond to moments pointing in $\hat{x}$ and the the blue in $-\hat{x}$. (a) A 180° DW: Moments rotate through 180° while going from the state in green to the state in orange. (b) A 360° DW: Moments rotate through 360° while going from the state in green to the state in orange.

that of the previous one with respect to $\hat{x} = 0°$. From the moment pointing in the direction of the green arrow to the one pointing in that of the orange one, the moments rotate through 180°. We say we have a 180° DW, where the moments rotate 180° along the domain wall. As the moment in the middle of the domain wall points *down* (in $-\hat{y}$) on the linear nanowire, we call this a *down* 180° DW. We can also have an *up* 180° DW if the moment in the middle

23

points up (in $\hat{y}$). In Fig. 8*b* from the moment pointing in the direction of the green arrow

to the one pointing in that of the orange one, the moments rotate through 360°. We say we

have a 360° DW, where the moments rotate 360° along the domain wall. This particular 360°

DW is a CW (or *down-up* by the orientation of constituent 180° DWs from left to right) 360°

DW since the moments rotate CW as they travel along the DW, from left to right. We can

also have a CCW (or *up-down*) 360° DW if moments rotate CCW as they traverse through

the 360° DW (Fig. 9).
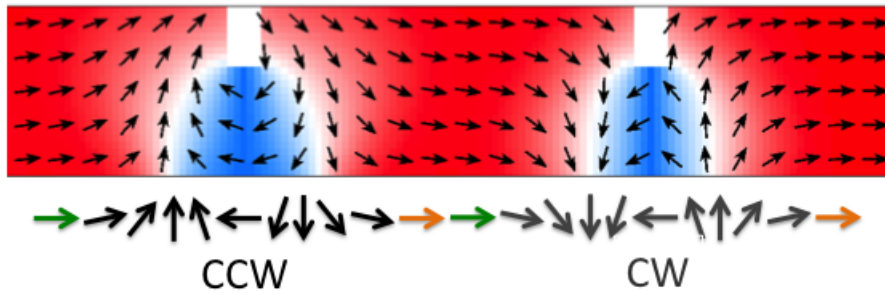
FIG. 9. A CCW and a CW 360° DW. Each DW is pinned at a notch. The wire is 100 nm wide; the notches are 16×32 nm^2.

B) Stray field

Regarding a domain wall, let us consider the field created by the moments. If we extend each

magnetic moment as part of a cumulative magnetic field, we obtain the stray field diagram

of a domain wall.

The net stray field is maximized where moments do not align with the geometric boundaries

of the structure; therefore, stray field is maximized whenever magnetostatic energy is maxi-

mized.

Due to their stray field that extend along the ferromagnet, e.g., as a continuation of field lines

F. I. Kaya
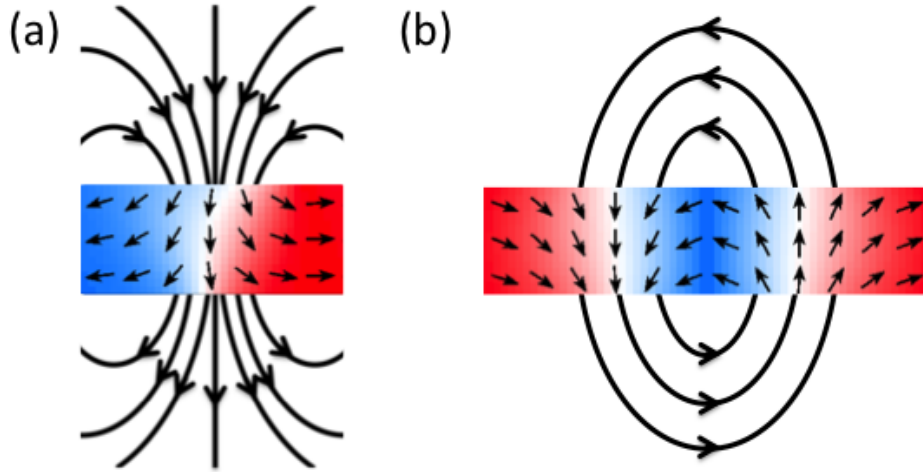
FIG. 10. Approximate stray field diagrams (a) of a 180° DW and (b) of a 360° DW on a ferromagnet. Red bits correspond to moments pointing in $\hat{x}$ and the the blue in $-\hat{x}$. The stray field due to moments outside of the DWs is omitted from the figure.

in Fig. 10a, 180° DWs interact with other moments, especially with those of neighboring 180° DWs. In comparison, 360° DWs have a closed stray field composition, hence tending less to interact with the neighboring moments (Fig. 10b). 180° DWs interact on shorter length scales than 360° DWs do. On these length scales, 180° DWs attract one another, thus restricting the control over their movement along a wire.

On the other hand, we can pack 360° DWs densely along a wire; they do not interact with the neighboring 360° DWs in ways leading to deformation (due to topology, see next section).

C) Topological edge defects

Let us consider the angle, ϕ, between a set axis and a magnetic moment to be an order parameter. By calling ϕ an order parameter, we mean the medium, which is the ferromagnet, approaches its maximum order state if all of its moments have the same order parameter

25

(ϕ), hence if all the moments point in the same direction (as in Fig. 11).
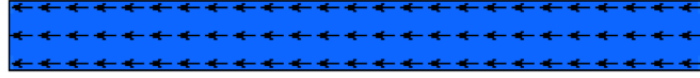
FIG. 11. A Linear ferromagnet with maximum order

At certain points in a ferromagnet we cannot define ϕ (e.g. point P in Fig. 12). We call these points, without a given ϕ value (hence without a given direction), *singularities*. We name these singularities *topological edge defects* (TEDs).
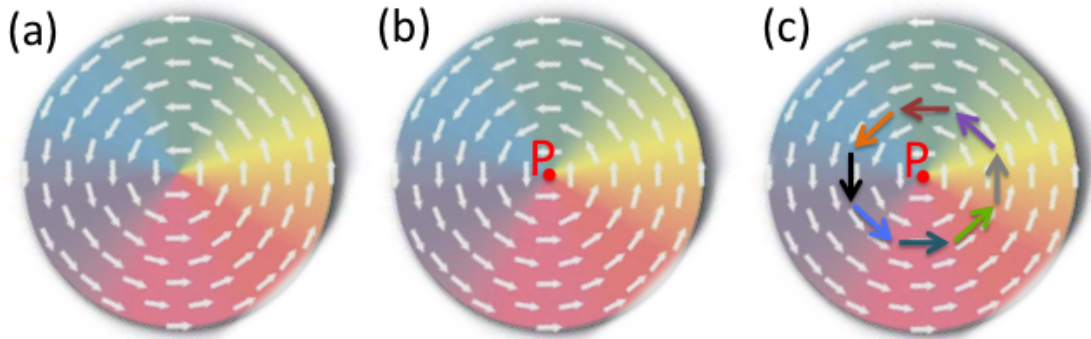
FIG. 12. Topological edge defect on a ferromagnet[5] (a) A circular ferromagnet with magnetic moment integrals indicated as white arrows. (b) A TED is present at point P. At this singularity, the direction of moments is undefined. (c) The pattern of moment integrals around a TED; having a different color corresponds to pointing in a different direction.

In Fig. 12 we investigate a topological edge defect on a circular ferromagnet. All through the ferromagnet, except at point P, moments have defined directions. In particular, we can assign an order parameter, ϕ, to each of the moments represented with white arrows. Each of these arrows indicates an integral of moments on a unit area $\Delta x \times \Delta y$ of the ferromagnet, thus making it easier for us to plot the magnetization on such a ferromagnet. On this ferromagnet if we close in at point P, then we see the pattern of moments being present as

F. I. Kaya

the colored arrows in Fig. 12b except when we get close enough that at an area $\delta x \times \delta y$ at point P, the magnetization will have an undefined ϕ value (or in Cartesian coordinates, the x and y direction of the moment vector will be zero). This means that a TED is present at point P. This specific TED has a +1 charge assigned to it.[6] The positive sign means each subsequent magnetic moment has a greater ϕ than the previous one. 1 means moments evolve in a loop; if we start by the orange moment in Fig. 12c and go around the TED in CCW direction, we eventually reach at the orange moment again.
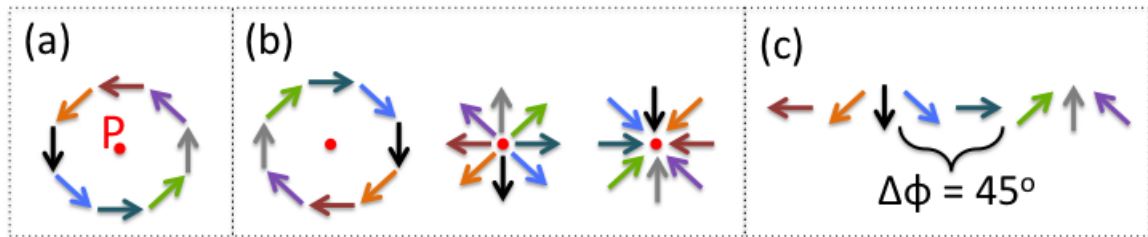
FIG. 13. Topological edge defects with +1 charge (a) Moments circulate CCW around the TED at point P. (b) Three other configurations for a TED with +1 charge. (c) ϕ increases with each subsequent moment in a CCW traversal around the TED; $\Delta\phi = 45°$ from red to orange, orange to black, etc..

In Fig. 13a and b the change in ϕ is positive for each emerging dipole moment integral as one moves CCW around the TED (as in Fig. 13c). This defines the sign of TED's charge as positive: +1.
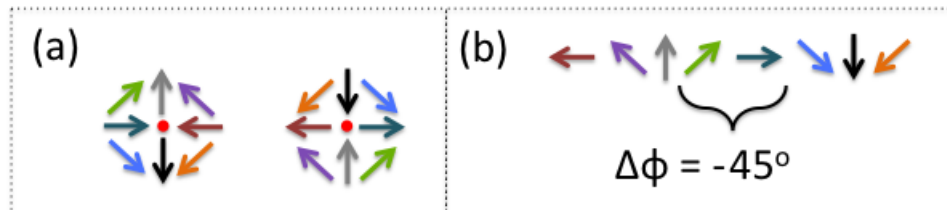
FIG. 14. Topological edge defects with −1 charge (a) Configurations for TED with −1 charge (b) ϕ decreases with each emerging moment in a CCW traversal around the TED; $\Delta\phi = -45°$ from red to orange, orange to black, etc..

In Fig. 14*a* the change in ϕ is negative for each emerging dipole moment integral as one moves CCW around the TED (as captured in Fig. 14*b*). This defines the sign of TED's charge as negative: -1.

i) Principles of counting TED charges on ferromagnets
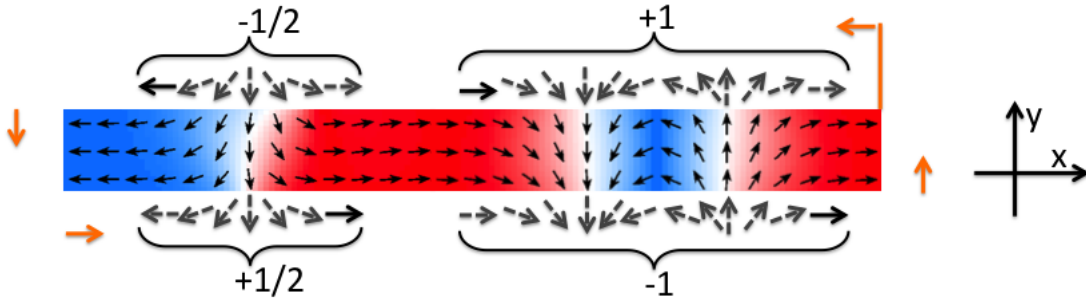
FIG. 15. Topological edge defects on a linear ferromagnet. Orange arrows indicate the direction of traversal when counting TED charges. Blue bits have moments point in $-\hat{x}$ and the red in $\hat{x}$.

If we assume a linear ferromagnet exists in the state in Fig. 15, then we can count the charges of TEDs by starting at the upper right corner, where the orange line is, and traverse CCW around the ferromagnet, following the orange arrows. We classify the magnitude of *TED charges* (or *topological edge charges*) as a 1 if moments go through a full $360°$ rotation around a TED and as a $1/2$ if moments go through a $180°$ rotation. In this sense we assign a topological edge charge to a TED due to the rotation of moments around it, in multiples of $360°$: A $180°$ rotation corresponds to a $180°/360°=1/2$ charge and a $360°$ rotation corresponds to a $360°/360°=1$ charge.

We set $\phi = 0°$ along the $\hat{y}$ axis. Then, for instance, ϕ is $-90°$ before the first TED, it increments as we move along the TED (hence each emerging moment has rotated CCW with

respect to the previous moment), and it approaches $-90°$ again at the end of the first TED. When measured in Cartesian coordinates, the sum of charges of TEDs, being measured at boundaries of the ferromagnet, always add upto zero. Also note that each 360° DW or 180° DW alone has its TED charges sum to zero; $+1 - 1 = 0$ for the 360° DW and $-\frac{1}{2} + \frac{1}{2} = 0$ for the 180° DW in Fig. 15.

With circular and elliptical ferromagnets, we set $\phi = 0°$ along the radial vector at the point of measurement in order to better study the topology of each DW.
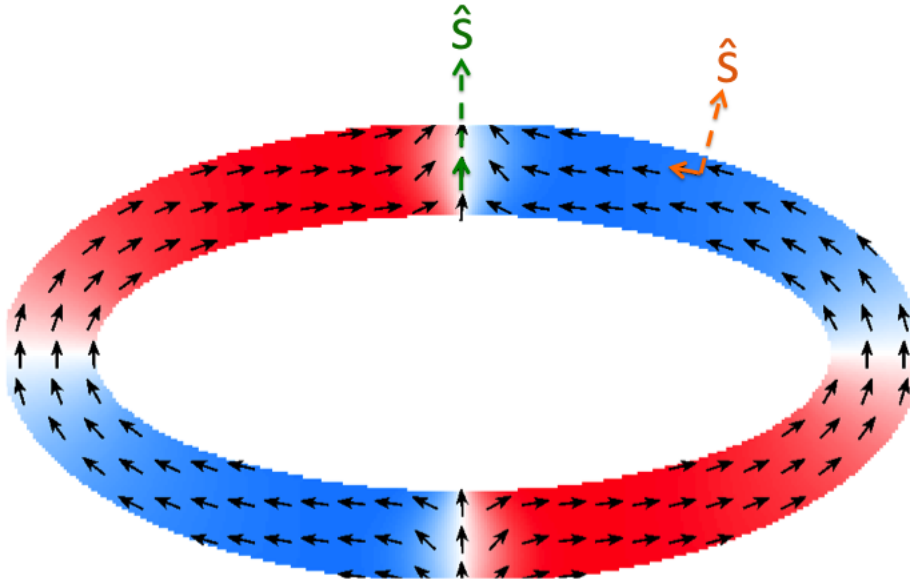
FIG. 16. Radial vector on an elliptical ferromagnet

In Fig. 16 we show two radial vectors $\hat{s}$, one in green and the other in orange. The angle between the green moment and the radial vector along the moment is 0°, so we define $\phi = 0°$ for the green moment. On the other hand, the angle between the orange moment and the radial vector along the moment is 90°, so we define $\phi = 90°$ for the orange moment.
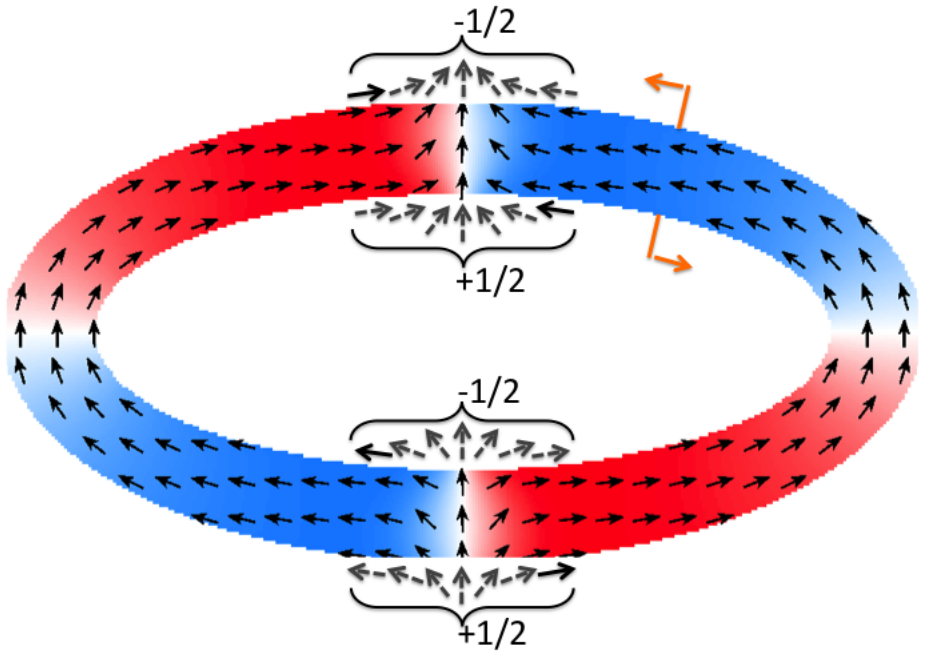
FIG. 17. Topological edge defects on an elliptical ferromagnet. Orange arrows indicate the direction of traversal when counting TED charges. Blue bits have moments point in $-\hat{x}$ and the red in $\hat{x}$.

Fig. 17 demonstrates how we count TED charges on elliptical ring ferromagnets. We traverse the outside boundary of the ferromagnet CCW and the inside boundary CW. (This principle holds for ferromagnets of any shape). Setting $\phi = 0$ in the radial direction (along a vector normal to the surface of the ferromagnet, pointing away from the elliptical center), we observe that moments rotate $\Delta\phi = 180°$ along a 180° DW and $\Delta\phi = 360°$ along a 360° DW.

D) Pinning, de-pinning, and re-pinning

Obeying PEM, a DW *stabilizes* at sites where its energy is reduced in comparison to the surroundings. We call these sites *pinning sites*. Pinning sites we use are notches and curved surfaces. In comparison to the rest of the wire, the shortening of the DWs at notches reduces the energy of DWs and lets DWs become pinned at notches (see section 2). The
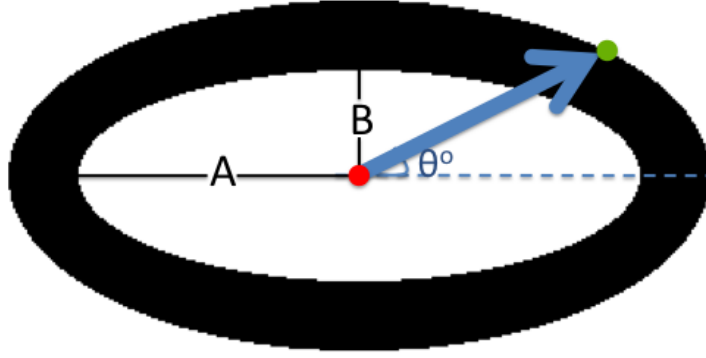
FIG. 18. An elliptical ferromagnet with major axis A and minor axis B. Red dot spots the origin of the ellipse; the green dot marks the point of curvature measurement. θ defines the angle with respect to $\hat{x}$ along which the point of measurement lies.

change in curvature also affects pinning strength (see section 3). Since a DW stabilizes at a pinning site, we need a higher magnetic field or spin transfer torque to move it than to move an un-pinned DW. (For details in current induced motion of DWs, see Zhang et al.[7]).

B. Basics of Curvature on Ferromagnets

In this section we consider ellipses with eccentricity greater than or equal to 1 ($A/B \geq 1$ in Fig. 18). When the eccentricity is 1, the ellipse is a circle with constant curvature. When the eccentricity is greater than 1, curvature varies along the ellipse.

As in Fig. 18 let r be the length of a vector that points from the origin (red) of the ellipse to the point of measurement (green). This vector $\vec{r}$ is depicted as the blue arrow in Fig. 18. Then, we define the order parameter θ as the angle between $\vec{r}$ and $\hat{x}$, which is captured in Fig. 18 along the blue dashed line. This way, we can define $\vec{r}$ as a function of θ such that

$$r(\theta) = A\,B\left(\,(B\,cos\theta)^2 + (A\,sin\theta)^2\,\right)^{1/2}\quad,$$

where A is the length of the major axis and B is that of the minor.

Let $r' = dr/d\theta$ be the first derivative of r with respect to θ and $r'' = d^2r/d\theta^2$ the second derivative likewise. Then, we can define curvature, κ, as a function of θ such that

$$\kappa(\theta) = \frac{|\ r^2 + 2\,(r')^2 - r''r\ |}{(\ r^2 + (r')^2\ )^{3/2}} \quad .$$

We define eccentricity to be the ratio A/B. On an ellipse with eccentricity greater than 1, meaning the major axis is longer than the minor axis, the curvature is maximized along the major axis and minimized along the minor axis.

We can use curvature along a ferromagnet to pin domain walls. By varying curvature along a ferromagnet, e.g., by assigning an elliptical geometry to a ferromagnet, we can see the change in energy as a function of curvature. This approach to curvature has not been preceded in literature.

We have devised elliptical magnetic fields on OOMMF simulations. Simulating the application of elliptical fields, we have explored the de-pinning and re-pinning mechanisms of domain walls on elliptical ferromagnets in a novel way (see section 3).

C.   Simulations on Ferromagnets

1.   *Magnetic Force Microscopy*

A ferromagnet's topographic properties can be mapped by using an Atomic Force Microscope (AFM), which embodies a cantilever that oscillates at its own resonant frequency as it scans across a surface (for details, see Goldman 2010). Setting the tip of the AFM at a preferred height, we can perform a Magnetic Force Microscope (MFM) scan to map out the ferromagnet's magnetic features.

The MFM technique involves scanning a ferromagnet by utilizing a magnetized tip attached to a small cantilever that lets the tip move up and down in response to the stray field of a domain wall. The bending of the cantilever is recorded and analyzed to obtain a measurement of domain wall characteristics on the ferromagnet. Thinking of the tip as a magnetic dipole, during the scanning, it experiences a force determined by the gradient of the magnetic field along the z direction. This force is generally the largest above a domain wall, where the space derivative of the stray field is the largest.

We can use MFM simulations to investigate domain wall features on ferromagnets.

Fig. 19 provides the result of a sample simulation, depicting an elliptical ferromagnet in the onion state (same state as in Fig. 17). The MFM image is generated on MatLab by inputting the vectors of magnetization pertaining to the structure. The plot consists of the derivative of the stray field in $\hat{z}$ at a given height. For more detail on the MFM technique and simulations, see Goldman 2010.

F. I. Kaya
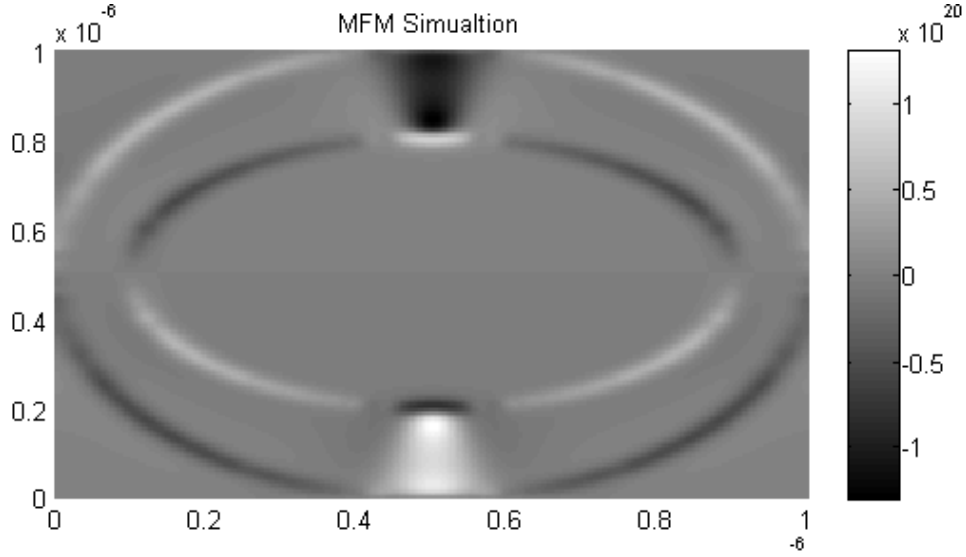
FIG. 19. MFM simulation picture of elliptical ferromagnet, simulated as if captured at 30 nm height

2. *OOMMF software*

We use the Object Oriented Micro-Magnetic Framework (OOMMF) Software by NIST to run micromagnetic simulations.[1] OOMMF iteratively solves the Landau-Lifshitz-Gilbert equation, which is

$$\frac{d\mathbf{M}}{dt} = -\gamma \mathbf{M} \times \mathbf{H} + \frac{\alpha}{M_{sat}} \mathbf{M} \times (\mathbf{M} \times \mathbf{H}) \quad,$$

in order to minimize the energies of magnetic structures. Here, M_{sat} is the saturation magnetization, $\mathbf{M}$ is the magnetization of the ferromagnet, $\mathbf{H}$ is the effective field ($\mathbf{H} = \mathbf{H}_{ext} + \mathbf{M}$), γ is the gyromagnetic ratio, and α is a damping constant. The gyromagnetic and damping factors relate as

$$\gamma = \frac{\gamma_G}{1 + \alpha_G^2} \quad, \qquad \alpha = \gamma \alpha_G \quad,$$

where G denotes Gilbert, $\gamma_G \approx 2.213 \times 10^5$ m A^{-1} s^{-1}, and the Gilbert damping constant α_G is measured for each ferromagnet.[8]

F. I. Kaya

The LLG equation describes how magnetization of a ferromagnet evolves in time, including its precession and damping.
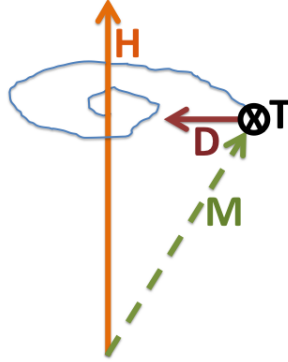
FIG. 20. The damped precession of a magnetic moment $\mathbf{M}$ under an effective field $\mathbf{H}$. $d\mathbf{M}/dt = \mathbf{T} + \mathbf{D}$, where $\mathbf{T}$ contributes to torque and $\mathbf{D}$ to damping. The blue line shows the path that $\mathbf{M}$ follows as it aligns with $\mathbf{H}$.

In Fig. 20 we represent the LLG equation as $d\mathbf{M}/dt = \mathbf{T} + \mathbf{D}$, where $\mathbf{T} = -\gamma\,\mathbf{M} \times \mathbf{H}$ represents the vector that creates the torque on the moment, and $\mathbf{D} = \frac{\alpha}{M_{sat}}\mathbf{M} \times (\mathbf{M} \times \mathbf{H})$ represents the vector that creates the damping. The two vectors in combination cause the damped precession of the moment; it starts rotating around the effective field vector $\mathbf{H}$, and its radius of rotation decreases in time until it aligns closely with $\mathbf{H}$. The rough nature of the blue path line that M follows, while it goes under damping and precession, takes small perturbations into account, e.g., due to temperature. To avoid such disturbances in our calculations, we set our simulations at 0 K. Furthermore, we set the material parameters to the typical parameters of a Fe-Ni permalloy so that the exchange constant is $A = 1.3 \times 10^{-11}$, and the saturation magnetization is $M_{sat} = 8 \times 10^5$ A/m.

The solution to the LLG equation is numeric for units of volume of ferromagnetic material, and OOMMF lets us obtain three-dimensional matrices, e.g., of magnetization or of field values. We can then assign an RGB value to each xyz vector value in the matrix to convert

the output files to bitmaps in order to visualize them. In all OOMMF-data-to-bitmap conversions we use color coding due to either the direction of moments or to their divergence along the geometry. (We will demonstrate this in detail in the relevant sections).

Initially, moments experience relatively large torques under the external field. They begin to rotate. Ultimately, the change in their magnetization with respect to time, as they try to align with the field, falls under a threshold value. We set each run to terminate when dM/dt reaches 0.1 deg/ns. Then, the field is turned off, and the structure relaxes to its final state under zero field, again, until dM/dt reaches its threshold value. We call this last process *relaxation.*

3.   *Angle Finder*

In order to calculate the exact angle of a DW on an elliptical ring ferromagnet, we wrote the MatLab code *Angle Finder*, which finds the maximum magnetization in $\hat{z}$ and determines its polar coordinates (see Appendix B for details). This approach works since the magnetization in $\hat{z}$, M_z, approaches a maximum at the center of a domain wall (See Fig. 21 and Fig. 22).

As captured in Fig. 21, the maximum magnetization in $\hat{z}$ corresponds to the same angular coordinate as where the domain wall is on an elliptical ring ferromagnet (see Fig. 22).

Looking at Fig. 22, we can clearly see that the MFM, OOMMF, and Angle Finder plots match, leaving it to our preference to work with either.

While working with the Angle Finder, one thing to pay attention to is finding $M_{z,max}$ at a
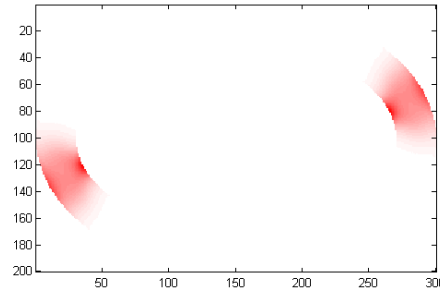
FIG. 21. Plot of magnetization magnitude in $\hat{z}$, of elliptical ring ferromagnet with $A/B = 1.5$, after is has been initialized at $\theta = 60°$ and relaxed under zero field. Darker red corresponds to a higher magnetization value.
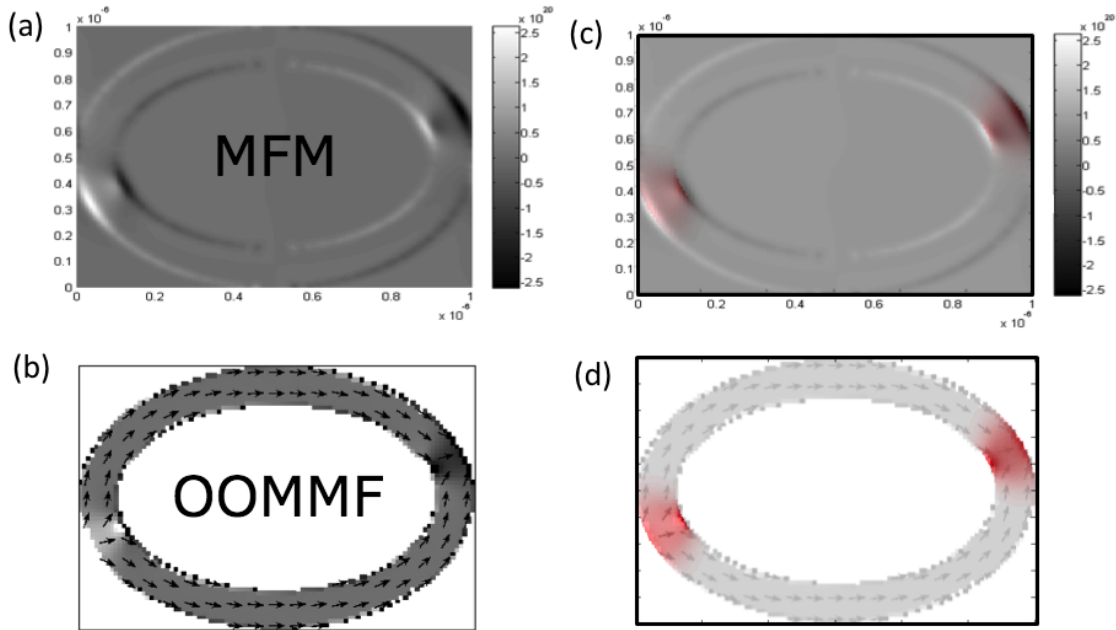
FIG. 22. Correspondence between the Angle Finder plot and plots of MFM and OOMMF simulations for elliptical ring ferromagnet with $A/B = 1.5$, initialized at $\theta = 60°$ and then relaxed (a) MFM plot at 25 nm height (b) OOMMF plot of divergence (c) Overlap of MFM plot with Angle Finder plot (d) Overlap of OOMMF plot with the Angle Finder plot

fixed width along the ellipse. The radial coordinate (e.g., whether M_z hits a max on the inner or outer edge of the ring) sometimes varies in a run or from run to run. In order to avoid changes in angle measurements due to this radial switching of $M_{z,max}$, we generally specify angle measurements of $M_{z,max}$ to be at the outer half of the width of the ellipse (Fig. 23), and this produces $M_{z,max}$ values along the outermost ring of the elliptical ferromagnet (the

outermost ring has unit thickness introduced by the simulation program).
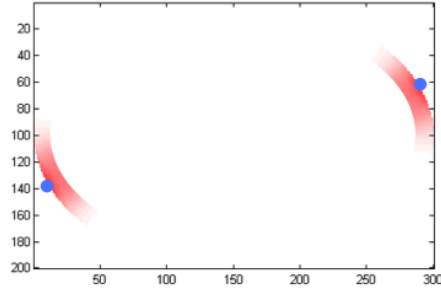
FIG. 23. Angle Finder finds $M_{z,max}$ on the outer half of the width of the elliptical ferromagnet. Blue dots mark approximate coordinates of $M_{z,max}$. Measurements in the quadrants I and III yield the same angle. Darker red corresponds to a higher magnetization value in $\hat{z}$.

D. Literature on DWs in Data Storage

In this section we first introduce and then elaborate on proposals for magnetic data storage.

Domain walls have been proposed for data storage applications since the 1980s, and one of the earliest proposals is the *Bloch line memory*, which uses pulsed magnetic fields.[9] Another is the *racetrack memory* as proposed by IBM, using current pulses (also known as *spin torque transfer*).[10,11] There have also been proposals to use DWs in ring-shaped devices, and the one most commonly known is the *nanoring memory*, which uses just the Oersted field from a central wire, sometimes in addition to spin torque transfer, to control the switching of the domain(s) on a ring-shaped ferromagnet.[12,10]

Gonzalez-Oyarce et al. more recently proposed to use 360° DWs in a strip, where either they place the domain walls at notches and use current pulses to move them, or they nucleate

F. I. Kaya

360° DWs via a pad at one end of the wire and then move them along the wire by using spin-polarized current.[13]

We detail the two most commonly cited proposals using DWs in data storage, below.

1. Racetrack memory

Racetrack memory proposes a *write* mechanism to nucleate DWs and a *read* mechanism to read the configuration of domains, which are separated by 180° DWs, as information bits; e.g., encode 1 if domains point in $\hat{x}$ and encode 0 if they point in $-\hat{x}$. The *read* head uses a tunneling magneto-resistance (TMR) sensor.
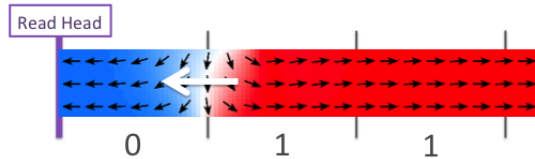
FIG. 24. Bits along a track of ferromagnetic wire. A domain with moments pointing in $\hat{x}$ (in red) codes for a 1 and a domain with moments in $-\hat{x}$ (in blue) for a 0. The white arrow indicates the direction of movement of the 180° DW under spin current, which is required for the *read* mechanism. The *read* head usually contains a TMR sensor.

Along a long ferromagnetic nanowire, which is similar to and hence called a *race-track*, a *read* head reads the orientation of domains as domain walls move along the structure under spin-polarized current (Fig. 24).

Fig. 25 is Parkin et al.'s main figure, where they explain the mechanism.[11] Tracks are composed of ferromagnetic nanowires, and they encode data in the pattern of domains. Blue domains have moments point in the opposite direction to the moments in the red domains.
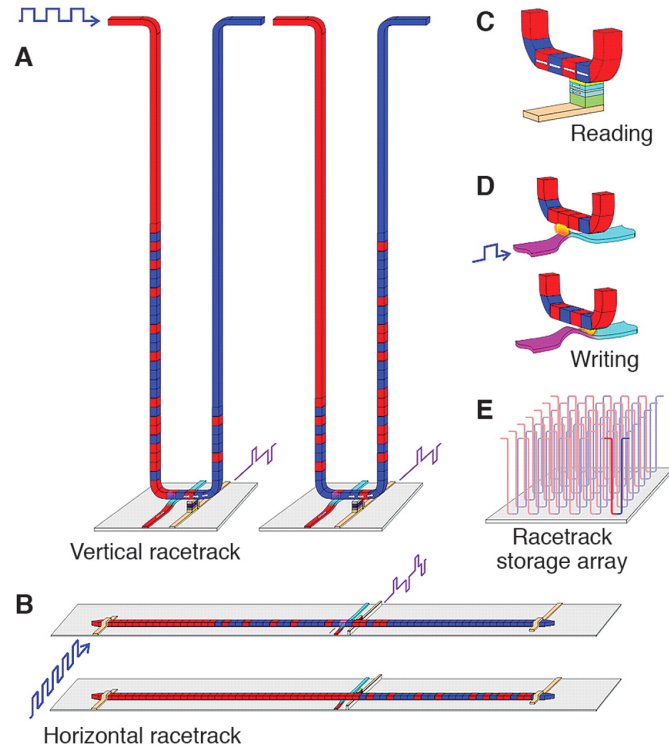
FIG. 25. Mechanism for racetrack memory[11] (**A**) Two states of a U-shaped *vertical* track, with a few of the DWs having moved past the read and write mechanisms along the horizontal plane (*plane of the substrate*), onto the opposite wing (**B**) Two states of a *horizontal* track, with a few of the DWs having moved past the read and write mechanisms, which are placed on the horizontal plane (*plane of the substrate*), in perpendicular to the racetrack (**C**) Reading mechanism with a magnetic tunnel junction unit (**D**) Writing mechanism relies on the stray field of DWs embedded and mobile on a second nanowire, which lies in perpendicular to the racetrack and on the same horizontal plane. (**E**) A mechanism for information storage using an array of racetracks on a chip

The red and blue domains are separated by 180° DWs, which can coherently move along the tracks by pulses of spin-polarized current. In part A as the DWs move to the opposite wing of the U-shaped track, they are *read* or *written* via the mechanisms along the horizontal part of the track. The substrate, which structures the *read* and *write* mechanisms, lies on the horizontal axis. This vertical U-track, as Parkin et al. suggest, bears the highest capacity for information storage. In B the racetrack lies on the substrate plane. In both parts A and B the *read* and *write* mechanisms perpendicularly intersect the racetrack on the horizontal plane. In C a magnetic junction unit connects to the racetrack and the *read*

mechanism measures its tunnel magnetoresistance. In D a second nanowire lies along the horizontal plane and normal to the racetrack and contains two 180° DWs, e.g., one on the left of the racetrack and the other on its right. Via moving one of these 180° DWs towards the racetrack, we can switch the magnetization in a domain on the racetrack to align with the direction of the stray field of the 180° DW on the second nanowire, where the stray field is a local magnetic field. In E, Parkin et al. propose that by constructing an array of racetracks on a chip, we can achieve high-density data storage.

If we wanted to implement the mechanism in Fig. 25, we would have to consider the interaction of two 180° DWs in the writing mechanism; the writing mechanism suggested in Fig. 25D might not work on a racetrack array as densely packed as in Fig. 25E.

2. Nanoring memory

Nanoring memory proposes to use an array of nanorings as a memory device, where the magnetic state of a reversible ferromagnetic ring codes for a 1 or a 0, hence encoding binary information. The magnetic state depends on the orientation of moments along the ring, e.g., CW vs. CCW.

In Muratov et al.'s proposal, a magnetic state with moments oriented mostly CW on a reversible ferromagnetic nanoring codes for a 1 (or a 0), whereas the state with mostly CCW moments codes for a 0 (or a 1).[12]

In Fig. 26 each nanoring in the array is composed of multilayers, two of which are ferromagnetic. The bottom ferromagnetic layer keep the orientation of its moments fixed while
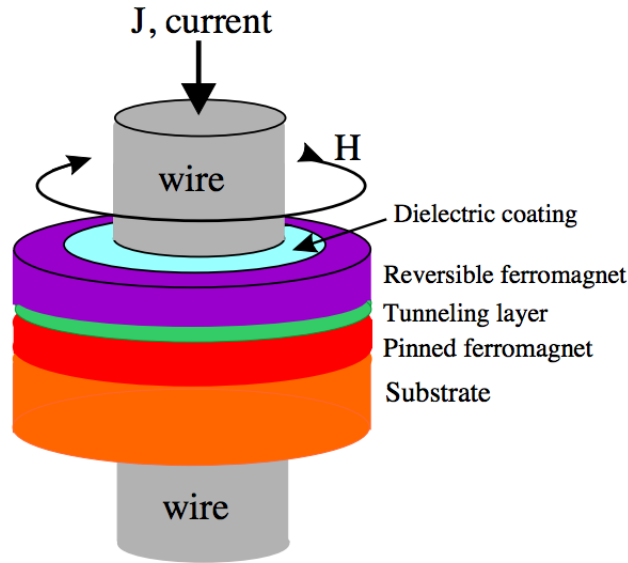
FIG. 26. Proposed nanoring memory device.[12] The magnetization of the *reversible ferromagnet* codes for a 1 or a 0. The orientation of moments in the *pinned ferromagnetic* layer is fixed.

current J, which passes through the middle of the nanoring, switches. As a consequence, the magnetization of the top layer changes, e.g., from mostly CW to mostly CCW. Since the magnetization of the bottom layer is fixed while the top layer changes magnetization, the overall magnetoresistance changes value, and so we can detect the switching of the domains by reading the magnetoresistance of the structure. Muratov et al.'s proposal, however, does not include such a read mechanism, and they would need additional contacts on the wire to use magnetoresistance if they intended to read states.[12] (We will discuss this in Zhu et al.'s proposal details, right after Muratov et al.'s).[10]

Fig. 27 shows the divergence plot of a magnetic state with moments traversing the nanoring, of 90 nm width and 450 nm outer radius, in mostly CW orientation. Under Muratov et al.'s proposal, if we assume that this state codes for a 1, then in order to create the state that codes for a 0, we need to apply a CW field co-centered with the ring. Such a field unwinds the 360° DW into two 180° DWs, moves the 180° DWs separately to the opposite side of

F. I. Kaya
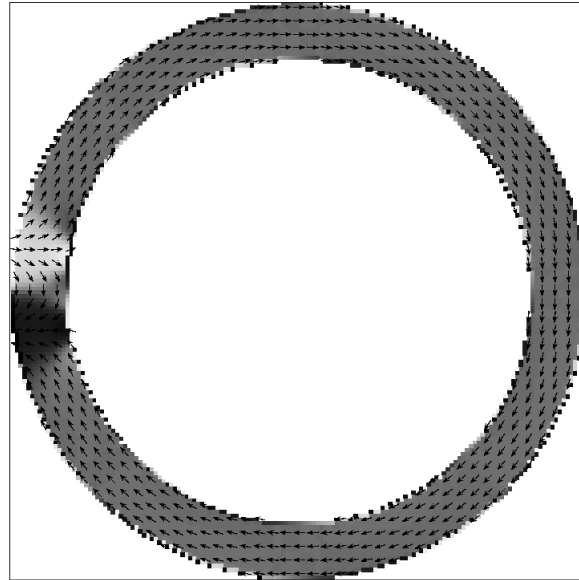
FIG. 27. Magnetic state in a nanoring with moments aligned mostly CW

the ring, where they recombine into a 360° DW. This results in a state where the moments

point in CCW orientation except where the 360° DW is, e.g., Step 180 in Fig. 28.

FIG. 28. Initialization and switching process on a proposed nanoring memory device.[12] Each time-step depicts a different orientation of moments on a nanoring during the process.

Fig. 28 presents time-steps during the initialization and switching of magnetic states of the

proposed nanoring memory device. At step 0, all moments point in $\hat{y}$. As they relax to the state in step 40, total energy is minimized. Step 50 is a snapshot in time while two 180° DWs move to the LHS of the nanoring under a CCW field that is co-centered with the nanoring. Step 60 shows a 1 (or a 0) magnetic state configuration, where a 360° DW sits on the LHS of the nanoring and the moments along the ring point mostly CW. This state corresponds to the state in Fig 27. Then, through steps 120 to 180, the 360° DW unwinds into two 180° DWs, which separately move to the RHS of the nanoring under a CW field co-centered with the nanoring and recombine into a new 360° DW there.

In Zhu et al.'s proposal, a magnetic state with moments oriented entirely CW on a reversible ferromagnetic nanoring codes for a 1 (or a 0), whereas the state with CCW moments codes for a 0 (or a 1).[10]
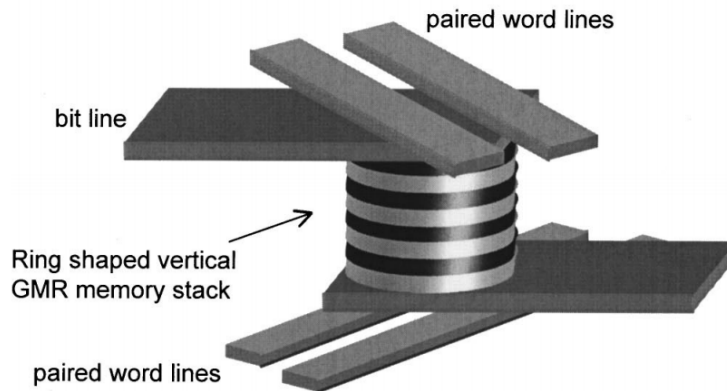
FIG. 29. Proposed mechanism of a memory cell using an array of ferromagnetic nanorings[10] The lightly colored rings are *soft magnetic layers*; the darkly colored are *hard magnetic layers*.

The mechanism as proposed in Fig. 29 has an array of nanorings in addition to a *bit line* and *paired word lines*. This specific combination of the hard and soft layers is proposed in order to minimize the switching current and the energy needed to operate the *write* and the *read*

mechanisms. The hard ferromagnetic layers require a relatively high magnetic field to reverse their orientation, e.g., from CW to CCW, whereas the soft ferromagnetic layers require a relatively low one to do so.[10] Produced by passing current through the bit line nanowire and concurrently through the paired word line nanowires (current points in the opposite direction on each pair), a composite magnetic field changes the magnetization of both layers. Then, for instance, by passing a low current to only switch the magnetization of the soft layers, we can read the magnetoresistance of the structure to detect the magnetization state of the hard layers.
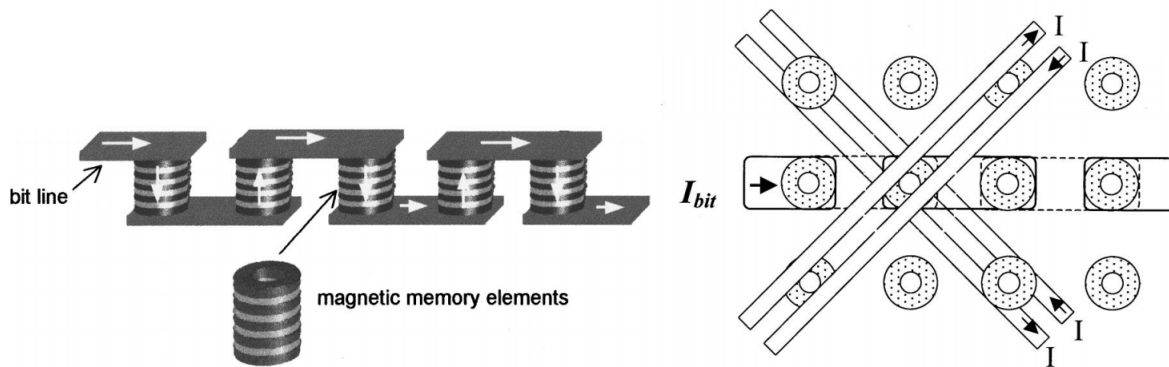
FIG. 30. A proposed array of nanorings as memory elements on a chip.[10]

Fig. 30 shows the proposed mechanism with the array of nanowires, each *magnetic memory element* coding binary information with a 1 or a 0. The 1 state vs. the 0 state depends on the orientation of moments along the hard ferromagnets (Fig. 31).

Fig. 31 depicts the process of switching of magnetic states, e.g., from a binary code 1 in state A with all moments aligning CW to a binary code 0 in state D with all moments aligning CCW.
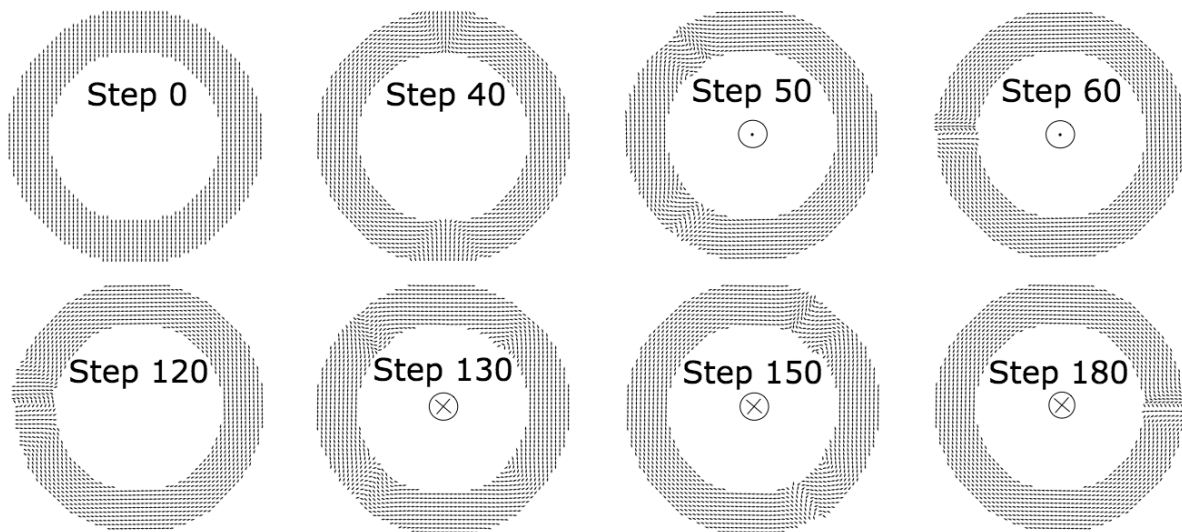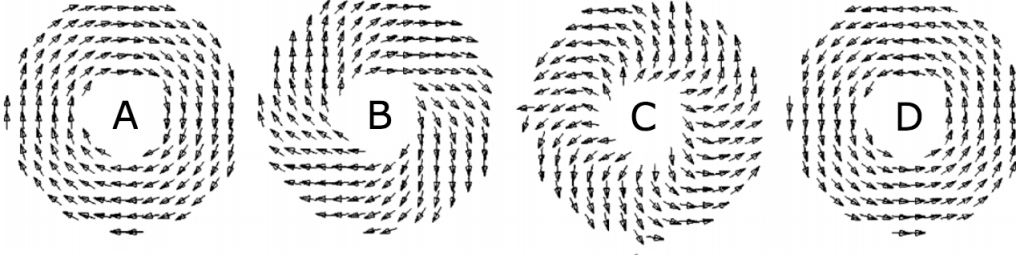
FIG. 31. Initialization and switching process on a proposed nanoring memory device.[10] Each state depicts a different orientation of moments on a nanoring during the process.

II. PACKING WIRES WITH $360°$ DWS

By manipulating DWs in ferromagnets, we can study their behavior relating to magnetic data storage. In this section we present our proposal for a new mechanism, where we use circular magnetic fields to nucleate and pack $360°$ DWs, thus achieving high-density data storage. This new technique, if further developed, can lead to new logic and sensing devices[14,15] and data storage of higher density than that of any current data-storage techniques.[11]

Topology is what determines whether two $180°$ DWs that unite annihilate or form a $360°$ DW; e.g., if the charges on TEDs of the $180°$ DWs add up to zero, then they annihilate.[6,16]

We prefer $360°$ DWs over $180°$ DWs, because due to the closed flux structure of the $360°$ DWs, we predict to pack them more densely than $180°$ DWs. The motion of $360°$ DWs under spin-transfer torque may differ from that of $180°$ DWs, but this has not been experimentally confirmed.[15,17]

Our proposal involves a versatile technique, where we can nucleate $360°$ DWs at arbitrary locations along a planar nanowire ferromagnet, by using a circular field centered in close proximity to the nanowire (Fig. 32). The technique in Fig. 32, which passes current through
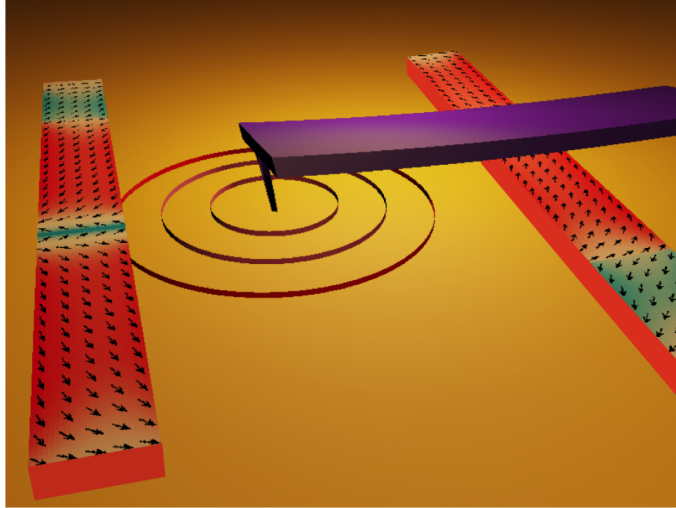
FIG. 32. Nucleation of a 360° DW by using a circular field

the tip of an AFM, evades any contact with the nanowire, where the data is being stored, and thus avoids energy alteration due to contact such as via heat transfer.[2] A more realistic device would have fixed wires at points, where we wanted to pass current. In order to investigate the feasibility of our design, we suppose we use the flexibility of the AFM tip given that we can do this in the lab.

A. Background

1. Previous work

In this subsection, we discuss a few commonly cited examples of DWs in data storage and present the cases of highest density packing of DWs that have been reported.

Racetrack memory, which we explained in the introduction, proposes to use transverse 180° DWs at a density that is about one 180° DW per 2.5 μm.[18,19] Due to their closed flux, 360° DWs have been proposed for use in racetrack devices.[13]

There exist a couple proposals that consider data storage via 360° DWs, by a rotating in-plane field and an injection pad[15,20,21,22] or by additional nanowires in contact with the ferromagnet.[23] The work of Gonzalez-Oyarce et al. that is captured in Fig. 33 inspired us to consider nucleating 360° DWs by using an in-plane circular magnetic field.[23]
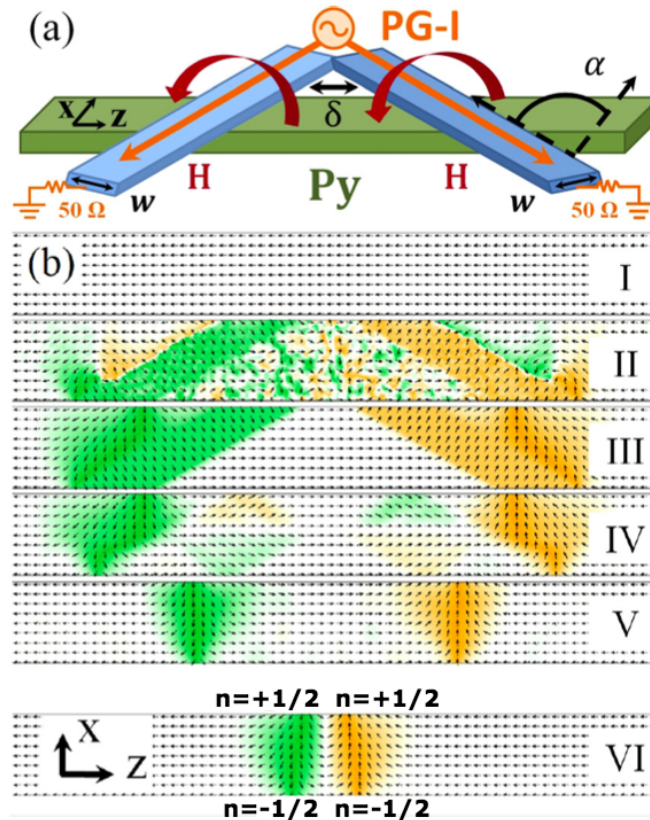
FIG. 33. Injection mechanism of a 360° DW[13] (a) The permalloy ferromagnet is in green and typically of 4000 nm length and $w = 200$ nm width. δ is the separation of nanowires on the permalloy, and α is the angle between the nanowire and the permalloy. PG-I is the electrical pulse generator that is connected to both nanowires and is grounded at the end of the nanowires as shown. As the current (orange) flows through the blue nanowires, it generates a magnetic field (red). (b) The magnetic field re-adjusts the direction of moments on the ferromagnet and injects a 360° DW on the permalloy ferromagnet. Green marks moments that point in $-\hat{x}$ and yellow marks those in $\hat{x}$.

In Fig. 33 the magnetic field generated by passing current through two additional nanowires aligns the moments into the state in Fig. 33$bIII$. The moments then relax to the state in

F. I. Kaya

Fig. 33VI with a 360° DW.

We intended to replicate the moment pattern in Fig. 33$bIII$ by using an in-plane circular field rather than the blue nanowires in the figure.
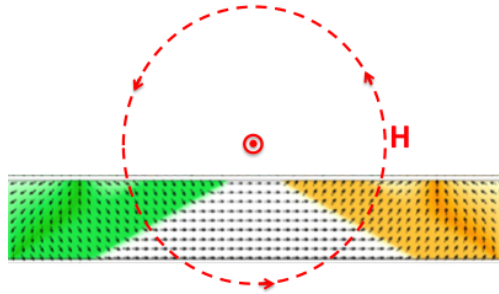
FIG. 34. Nucleation mechanism of a 360° DW via an in-plane circular field centered in proximity of the ferromagnet[13]

We predicted that we could nucleate a 360° DW on a ferromagnet by solely using a circular field and no additional nanowires. Hence, we devised a mechanism as shown in Fig. 34: By applying an in-plane magnetic field on a saturated nanowire (Fig. 33bI), we supposed that if we could rotate some of the moments along the ferromagnet into a state as in Fig. 33$bIII$, the moments would then relax into a state as in Fig. 33bVI, and hence we would nucleate a 360° DW on the ferromagnet. Our proposal did work in simulations, and we explain the physics of our mechanism in the following sections.

2.   Simulation details

Our simulations involve nanowires of varying length (in $\hat{x}$), of 100 nm width (in $\hat{y}$), and of 4 nm thickness (not shown in plots). The cell size is 4 nm along each of the three axes. In cases that involve notches, the notches are $16 \times 16 \times 4$ nm^3 unless stated otherwise. All notches are evenly spaced along the nanowire.

FIG. 35. Sample nanowire with notches

Fig. 35 shows a sample linear ferromagnet with given body and notch dimensions. We initialize each run in $-\hat{x}$ by using an in-plane field at 160 mT or higher. The circular field, applied past initialization, diminishes as $1/r$, where $\vec{r}$ points from the field center towards the point of measurement.
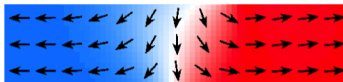
FIG. 36. Sample OOMMF color plot of magnetization of a nanowire section. Red points to the right ($\hat{x}$), blue to the left ($-\hat{x}$).

In this section, we use OOMMF magnetization plots of ferromagnets in their given state, where the color scale indicates the orientation of the moments along the x-axis: Red points to the right ($\hat{x}$), blue to the left ($-\hat{x}$) (Fig. 36), unless otherwise stated.

B.   Nucleation of $360°$ DWs by using a circular field

In Fig. 37 we display our mechanism for nucleating a 360° DW. We apply a 21 mA current 48 nm above the nanowire, which we previously initialized. This simulated current acts as if applied via an infinitely long wire, e.g., flowing out of the page and creating a CCW circular field (Fig. 37a). We may construct a device to realize what is shown in our simulations by placing nanowires normal to the plane of the ferromagnet but not contacting it. We can also realize the circular field by passing current through the tip of an AFM. The field
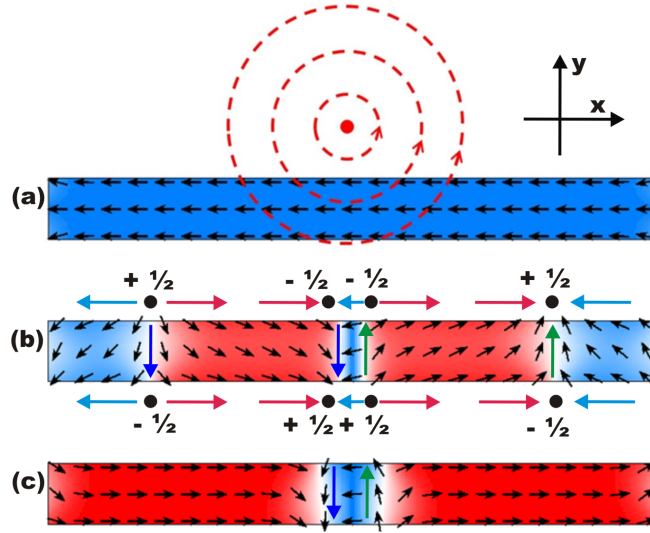
FIG. 37. Nucleation of a 360° DW by using a circular field[24] (a) Initialization of the nanowire and top-down view of the circular field (b) Snapshot showing the nucleation of a 360° DW and two 180° DWs. The numbers in black account for the TED charges of the DWs. (c) Relaxed state of a single 360° DW. Green and blue arrows help identify the topological winding of the DWs.

created corresponds to 87.5 mT at the top edge of the nanowire. It exerts a torque on the moments except where the relative difference in angle between the field and the moment is zero, directly below the field center. This dynamic results in the nucleation of a 360° DW below the field center and, due to topology,[25] two 180° DWs emerging left and right from the 360° DW (Fig. 37b).

Let us examine the underlying topology of Fig. 37b in more detail. The simultaneous nucleation of two 180° DWs with the 360° DW is a consequence of topology, more precisely, of TED charges adding up to zero on the nanowire boundaries. With the nucleation of the 360° DW, two TEDs are created on the upper boundary of the nanowire, each holding a −1/2 charge, and two TEDs are created on the lower boundary of the nanowire, each holding a +1/2 charge. With the simultaneously created 180° DWs, each with charge +1/2 on the upper boundary of the nanowire and charge −1/2 on the lower, the sum of the TED

charges on all boundaries of the nanowire add up to zero. This cancellation of TED charges is a topological necessity.

Again looking at Fig. 37b, regarding the 180° DWs around the 360° DW and the 180° DWs constituting it, we see that when a down 180° DW joins with another down 180° DW, their TED charges cancel, and the DWs annihilate. Likewise, if an up 180° DW joins with another up 180° DW, they annihilate.

Moving from Fig. 37b to c, the 180° DWs under the CCW field move towards the end of the nanowire and annihilate; e.g., they 'slide' off of the nanowire. Then, as the field is turned off, the wire relaxes to the state in Fig. 37c. On longer nanowires, before 180° DWs reach at the ends of the wire, the 360° DW slides towards one of the 180° DWs and annihilates into a single 180° DW as some of the TED charges cancel.

To overcome the sliding of the 360° DWs and hence to have better control over the 360° DWs, we introduce notches onto the nanowire. DW length (in $\hat{y}$) is reduced at notches. This lowers the energy cost of the DWs so that notches act as pinning sites.

C.   Packing $360°$ **DWs of opposite circulation on a nanowire**

In this subsection we focus on packing 360° DWs of opposite circulation at adjacent notches on a nanowire, e.g., a CW 360° DW next to a CCW 360° DW.

We have been able to pack opposite circulation 360° DWs as dense as one 360° DW in every 240 nm of the nanowire, which corresponds to 4 DWs per micron, by using $16 \times 16 \times 4 \ nm^3$

F. I. Kaya

notches.

1. *Packing mechanism*
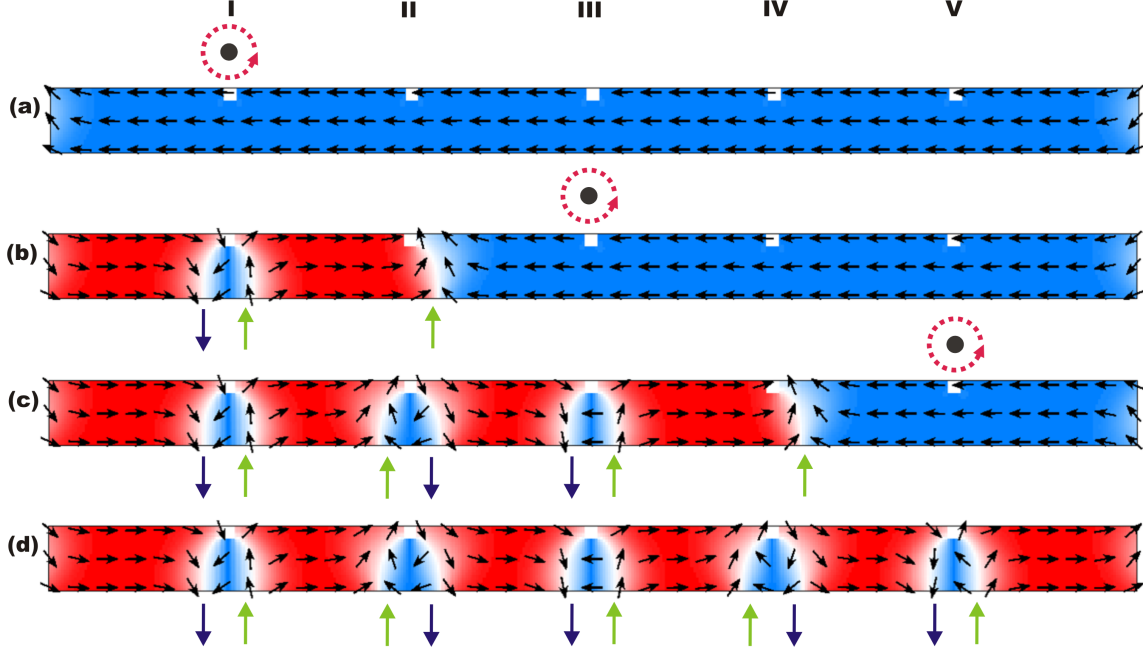
FIG. 38. The sequence of steps for packing 360° DWs of opposite circulation at adjacent notches.[24] Black points indicate the center of the circular magnetic field, and the red dotted arrows indicate it is CCW. (a) Initialization (b) Resulting state after applying 21 mA above notch **I** (c) Resulting state after applying 21 mA above notch **III**, creating a second 360° DW directly below, and two 180° DWs, one of which joins the 180° DW at notch **II** to form a 360° DW (d) Resulting state after applying 21 mA above notch **V**

Fig. 38 shows the sequence of steps we need to pack 360° DWs of opposite circulation at adjacent notches. The notch dimensions are 16×16 nm^2. (The notch thickness is 4 nm in $\hat{z}$; we keep it fixed for all trials involving notches). The inter-notch distance is 280 nm. We inject the first 360° DW at notch **I** by applying the current directly above it (Fig. 38a).[26] Two 180° DWs are nucleated concurrently with the 360° DW. The up 180° DW pins at notch **II** as the down 180° DW annihilates by sliding off of the wire. We then nucleate the second 360° DW at notch **III** by a similar procedure. The simultaneously nucleated up 180° DW pins at notch **IV** as the simultaneously nucleated down 180° DW joins the up

53

F. I. Kaya

180° DW that is pinned at notch **II**, thus nucleating a third 360° DW. By the same proce-
dure, we inject a fourth 360° DW at notch **V** and a fifth by adjoining 180° DWs at notch **IV**.

In the end, we have successfully packed 360° DWs of opposite circulation at adjacent notches;
a CW 360° DW at notch **I** is followed by a CCW 360° DW at notch **II**, which is followed by
a CW 360° DW at notch **III**, and so on (Fig. 38*d*).

2. *Failure mechanism*

With 16×16 nm^2 notches, our trials to pack 360° DWs of opposite circulation closer together
at adjacent notches result in failure at inter-notch distances ≤ 220 nm.
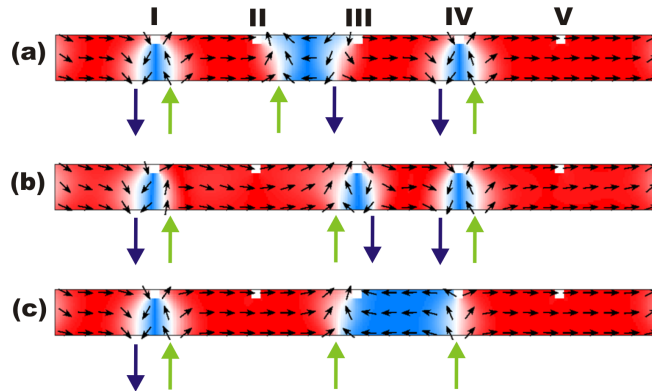
FIG. 39. Failure mechanism when packing opposite circulation 360° DWs at the inter-notch distance of 220 nm^2[24] (a)
360° DWs are formed at notches **I** and **IV**. The 180° DWs interact but do not adjoin at a single notch. (b) Temporarily
applying a CCW field above notch **II** pushes the two 180° DWs into a tight 360° DW at notch **III**. (c) When the field is
removed, the constituent down DWs are sufficiently close to interact and annihilate, leaving the two up DWs at their respective
notches.

Fig. 39 shows the failure mechanism for opposite circulation packing of 360° DWs. As the
inter-notch distance is too close for us to nucleate the second and third 360° DWs at notches
III and **II** respectively, we move one notch over and nucleate the second 360° DW at notch

F. I. Kaya
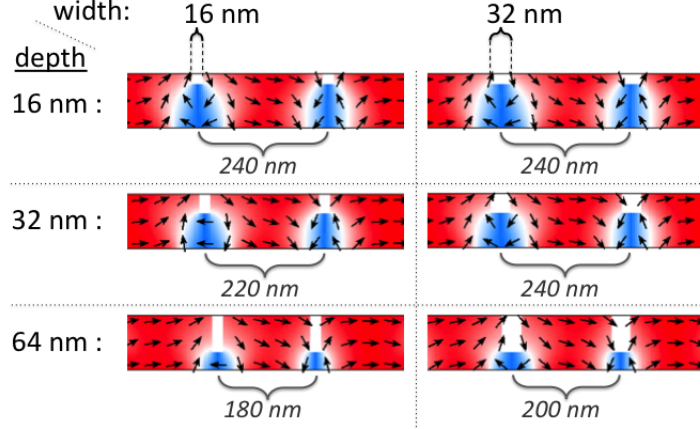
FIG. 40. Closest packing for 360° DWs of opposite circulation. The notch widths 16 nm and 32 nm are paired with notch depths 16 nm, 32 nm, and 64 nm. The wires continue along $\pm\hat{x}$.

IV. This, in turn, nucleates the third 360° DW between notches **II** and **III** (Fig. 39a). By using a CCW field centered above notch **III**, we try to pin the third 360° DW at notch **III**. However, as the 360° DW at notch **III** (Fig. 39b) relaxes, the 360° DWs at notches **III** and **IV** attract one another and annihilate, resulting in the state in Fig. 39c.

The procedure of pinning the third 360° DW at notch **III** works for larger inter-notch distances; the 360° DW becomes pinned at notch **III** as in Fig. 39b, and the structure relaxes to a state, where the three 360° DWs remain at notches **I**, **III**, and **IV**.

3. *Changing the notch geometry*

Using our nucleation procedure, we have achieved opposite circulation packing of 360° DWs at adjacent notches as close as 240 nm apart with square notches of dimensions 16×16 nm^2 (Fig. 40). We have furthermore simulated closest packing for other notch dimensions.

F. I. Kaya

In Fig. 40 we demonstrate the closest packing for the given notch dimensions with 360° DWs of opposite circulation. Closest packing refers to the highest density packing of 360° DWs at adjacent notches such that if we reduce the inter-notch distance by 20 nm, the packing procedure fails, via the mechanism we demonstrated previously, in the same way for all notch geometries in this section.
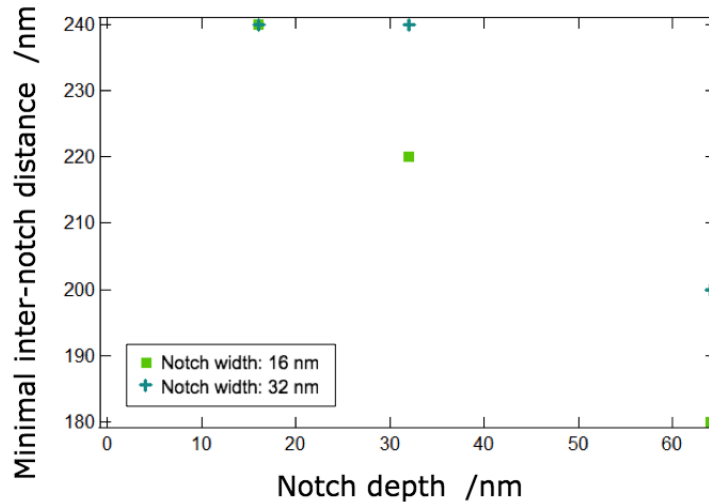
FIG. 41. Plot of inter-notch distance of highest density packing vs. notch depth

Fig. 41 shows a plot of the closest packing values we obtained as in Fig. 40. With notches of 16 nm width, the inter-notch distance that produces the closest possible packing is 240 nm for 16 nm depth, and it drops down to 180 nm for 64 nm depth (Fig. 40, Fig. 41). Although, we need to consider the trade off between notch depth and the amount of spin current we need to move the 360° DWs pinned at these notches. Due to this trade-off, using notches as deep as 64 nm is disadvantageous. It is hard to follow a similar trend for notches of 32 nm width, with only the given three points. Although the increase may not be as obvious for larger notches as it is for smaller ones, we infer that packing density increases with notch depth.

Notch Area / nm^2	Inter-notch Distance / nm					
$width \times depth$	160	180	200	220	240	260
16×16			X	X	√	√
16×32			X	√	√	
16×64	X	√				
32×16				X	√	
32×32		X	X	X	√	
32×64	X	X	√			

TABLE I. Close-packing statistics of opposite circulation 360° DWs for variable inter-notch distances and notch areas for rectangular notches. X indicates failure, and √ indicates successful packing at adjacent notches.

Table I summarizes all the trials we ran in order to acquire the data needed to create Fig. 40 and Fig. 41. The cross mark indicates failure and the check mark indicates successful packing of 360° DWs of opposite circulation at adjacent notches.

D. Obstacles in close-packing of 360° DWs

Once we start moving notches closer together, a few things arise that require attention:

- When a notch is too close to the edge of the wire, the field gradient at the edge inhibits the formation of 360° DWs at the notch.

- The simultaneously nucleated 180° DWs pin at a further notch.

- The center of the field to nucleate the second 360° DW needs to be farther away from the up 180° DW than only one notch.

F. I. Kaya

The field gradient might hinder the nucleation of a DW at the notches that sit horizontally close to the edge of the nanowire. For instance, in Fig. 42a, the down 360° DW slides off of the nanowire during nucleation.
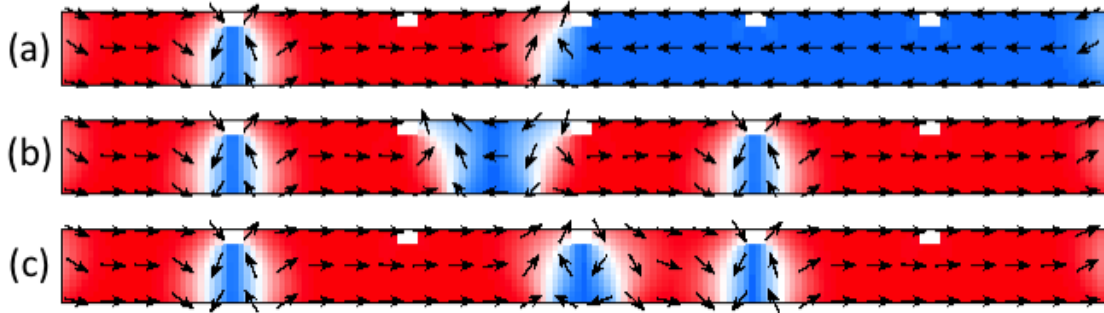
FIG. 42. Packing 360° DWs of opposite circulation on a nanowire of 32 × 16 nm notches and 240 nm inter-notch distance (a) The first 360° DW is nucleated. (b) The second 360° DW is nucleated, and the third 360° DW is nucleated between two notches. (c) By applying a CW field centered on top of one of the notches surrounding the unpinned 360° DW, we can pin it at that notch.

The strength of the field, during the nucleation of a 360° DW, is larger at a neighboring notch when the neighboring notch is closer. This causes the 180° DWs to pin at two or three notches over, depending on the inter-notch distance, the notch geometry, and the strength of the field we use to create them (Fig. 42b).

Furthermore, in very small inter-notch distances, the second 360° DW cannot be nucleated at the notch nearest to the up 180° DW (Fig. 42c). If we want to pack a couple of 360° DWs at neighboring notches, then the procedure requires moving 180° DW constituents of the 360° DWs separately; we cannot move the constituents via a circular field once they form a 360° DW and pin at a notch (see next subsection).

E. Packing $360°$ DWs of identical circulation on a nanowire

In this subsection, we focus on packing 360° DWs of the same circulation at adjacent notches on a nanowire, e.g., a CW 360° DW next to another CW 360° DW.

We have been able to pack two 360° DWs as dense as one 360° DW in every 100 nm of the nanowire, which corresponds to 10 DWs per micron and which has not been reported in simulations or experiments before. We have used $16 \times 32 \times 4$ nm^3 notches to do so.

1. *Topological advantage of identical circulation packing of* $360°$ *DWs*

Topological edge defect (TED) charges help us understand the topological consequences of bringing two 180° DWs together.
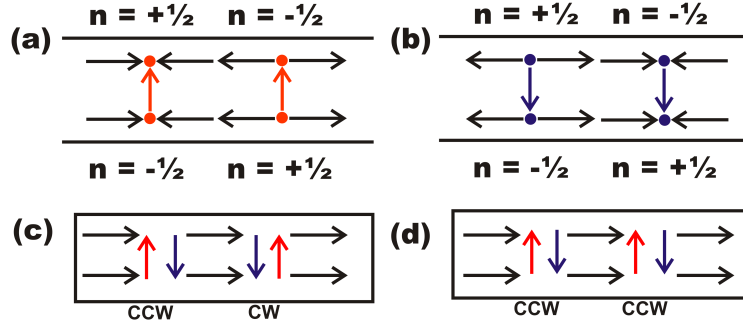
FIG. 43. Schematic representations of TEDs[27] (a) Two *up* DWs with opposite TEDs (b) Two *down* DWs with opposite TEDs (c) 360° DWs with opposite circulation and opposite TEDs (d) 360° DWs with identical circulation and identical TEDs

If two 180° DWs have opposite charges on a given boundary, e.g., along the top edge of the nanowire, as in Fig. 43*a* and *b*, then their union results in annihilation. Fig. 43*c* shows two 360° DWs of opposite circulation next to one another. If we push the two 360° DWs of opposite circulation together, the contributing 180° DWs, on the side of contact of the two

F. I. Kaya

360° DWs, annihilate. This limits the packing density of 360° DWs of opposite circulation.

We overcome the limit on packing density by using 360° DWs of identical circulation along the entire nanowire, e.g., only CCW.

Fig. 43d shows two 360° DWs of identical circulation next to one another. If we push two 360° DWs of the same circulation together, the contributing 180° DWs, on the side of contact of the two 360° DWs, have the same charges on each boundary. Therefore, they do not annihilate on contact, and we can pack them more closely than 360° DWs of opposite circulation.

2. *Packing mechanism*

Fig. 44 shows the sequence of steps we need to pack two 360° DWs of identical circulation at adjacent notches. The number of each time step during the procedure is marked on the top right corner of the nanowires. The notch dimensions are 16×16 nm^2. (The notch thickness is 4 nm in $\hat{z}$ but not shown here). The inter-notch distance is 120 nm.

Once the wire is saturated by an in-plane field in $-\hat{x}$, we apply a CCW field above notch **III** and create the first 360° DW (Fig. 44a). Next, we initialize the second 360° DW at notch **XIII**; we cannot initialize it any closer to notch **III** due to the proximity of notches and interaction between the stray field of the 180° DW that is pinned at **VIII** and the second-to-be-created 360° DW. As the second 360° DW is being nucleated at notch **XIII**, two 180° DWs emerge towards the surrounding notches. The up 180° DW annihilates by sliding off of the nanowire, while the down 180° DW moves towards the middle of the
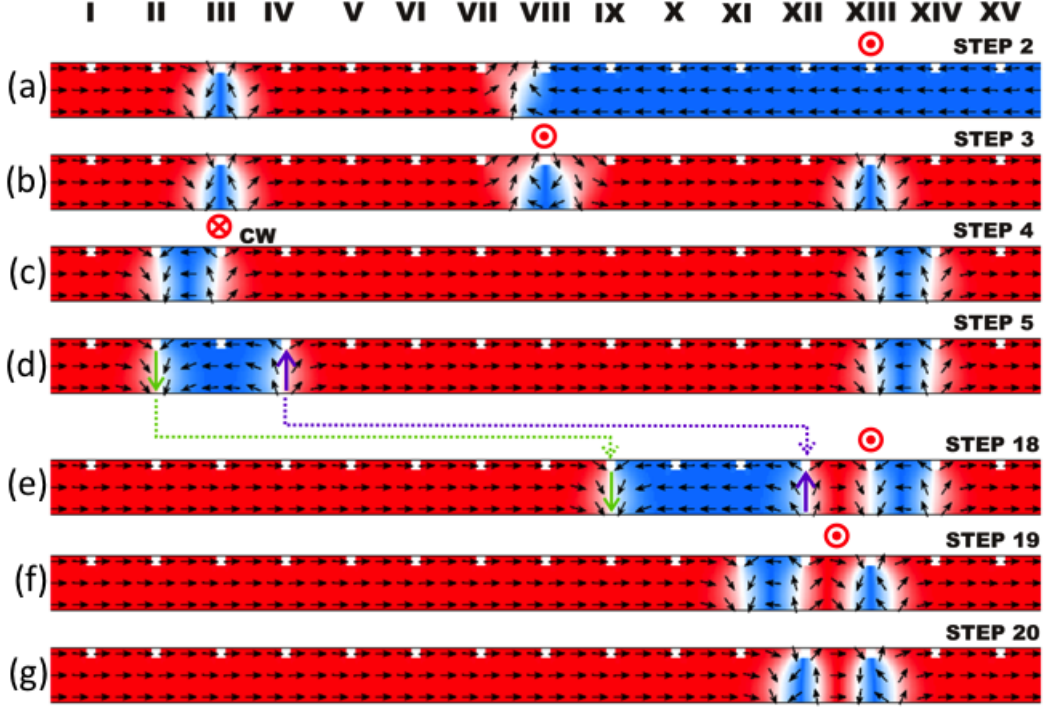
FIG. 44. The sequence of steps for packing 360° DWs of identical circulation at two adjacent notches spaced 120 nm apart[27] (a) Resulting state after applying a CCW field on the previous state initialized in $-\hat{x}$. The CCW field derives from a 21 mA current above notch **III**. (b) Resulting state after applying 21 mA above notch **XIII**, nucleating a second 360° DW directly below, and two 180° DWs, one of which joins the 180° DW at notch **VIII** to form a 360° DW. (c) Resulting state after applying 80 mA above notch **VIII**. The strong field annihilates the 360° DW directly below and unwinds the remaining 360° DWs into 180° DWs. (d) Resulting state after applying -15 mA above notch **III**. We continue to apply the -15 mA at subsequent notches to move the *up* 180° DW to notch **XII**, and then a CCW is used to move the *down* 180° DW at notch **II** sequentially to notch **IX**. These fifteen steps are not shown and the resulting state is depicted in (e). (f) Resulting state after applying 30 mA at notch **XIII**, forming the 360° DW directly below, and pinning the *down* 180° DW at notch **XI**. (g) Resulting state after applying 30 mA along between notches **XII** and **XIII**, forming the second 360° DW pinned at notch **XII**.

nanowire, joins the down 180° DW that is already pinned at notch **VIII**, and forms the third 360° DW pinned at notch **VIII**. Thereafter, we apply a CCW field above notch **VIII** that is strong enough to annihilate the 360° DW pinned there. This CCW field is strong enough to unpin the 360° DWs that are pinned at notches **III** and **XIII**. As a result, the constituent 180° DWs pin at notches **II** and **III** and at notches **XIII** and **XIV**. We then apply -15 mA above notch **III** and the generated CW field moves the up 180° DW one

notch over and pins it at notch **IV**.

Thenceforth, with each step forward we apply -15 mA above the notch, where the up 180° DW marked in purple in Fig. 44d is pinned, and the resultant CW field moves it one notch at a time towards notch **XII**. We then apply 15 mA above the notch, where the down 180° DW marked in green in Fig. 44d is pinned, and the resultant CCW field moves it one notch at a time towards notch **XI**. Once we obtain the configuration in Fig. 44e, we apply a CCW field centered above notch **XIII** that re-nucleates one of the 360° DWs and pins it there. Consequently by applying a CCW field centered along half-way between notches **XII** and **XIII**, we pin the remaining 360° DW at notch **XII**.

In the end, we have successfully packed 360° DWs of identical circulation at two adjacent notches, namely notch **XII** and notch **XIII**.

With 16×16 nm^2 notches let us consider what happens when we move the notches farther apart or closer together than as shown in Fig. 44. If we increase the inter-notch distance, then there exist less number of notches between the 180° DW and the first 360° DW, so we can nucleate all three 360° DWs less many notches apart. Thus, it takes less number of steps to achieve the adjacent packing of two 360° DWs of identical circulation. If we decrease the inter-notch distance, then the opposite happens and we need more number of steps. In addition, the magnetization does not evolve from Fig. 44f to g, and the packing fails.

3. Failure mechanism

The failure mechanism is simple. Continuing with Fig. 44, no matter where along $\hat{x}$ we place the center of the field above the nanowire and no matter what current value we apply, we cannot get the 180° DW at notch **XI** to join the 180° DW at notch **XII** and nucleate and pin a 360° DW there. In the case that we repeat Step 19 for a closer notch configuration, once we apply the CCW along between notches **XII** and **XIII**, the structure relaxes back to the state in f; e.g., the new Step 20 is identical to Step 19. The failure happens the same way for the other notch geometries we tested while packing 360° DWs of identical circulation.

4. Changing the notch geometry

Using our nucleation procedure, we have achieved identical circulation packing of 360° DWs at adjacent notches as close as 120 nm apart with square notches of dimensions 16 × 16 nm^2 (Fig. 44). We have furthermore simulated closest packing for other notch dimensions (Fig. 45).

Fig. 45a and b show closest packing for 16×16 nm^2 notches, with 360° DWs of opposite circulation and with those of identical circulation respectively, at adjacent notches. Moving from Fig. 45a to b, the packing density doubles by fixing the circulation of the 360° DWs to CW. Hence, we conclude that we can achieve much denser packing by using 360° DWs of identical circulation at adjacent notches than by using those of opposite circulation likewise.

Fig. 45c and d show the close packing we have achieved for identical circulation packing of 360° DWs, but not the closest possible packing. There is work to be done to test whether
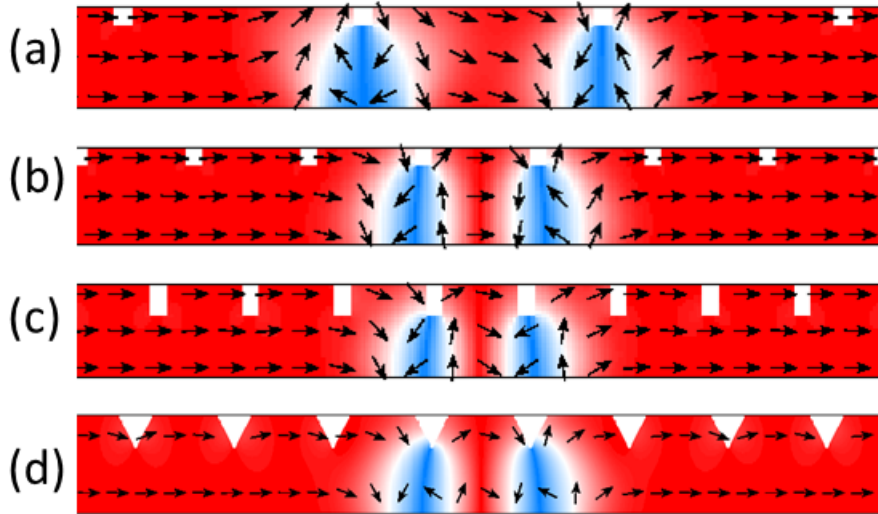
FIG. 45. Packing of 360° DWs at two adjacent notches[27] (a) Two 360° DWs of opposite circulation are packed on a wire with 16×16 nm^2 notches placed 240 nm apart. (b) Two 360° DWs of identical circulation are packed on a wire with 16×16 nm^2 notches placed 120 nm apart. (c) Two 360° DWs of identical circulation are packed on a wire with 16×32 nm^2 notches placed 100 nm apart. (d) Two 360° DWs of identical circulation are packed on a wire with triangular notches of 32 nm width ($\hat{x}$) and 32 nm depth ($\hat{y}$) placed 100 nm apart.[27]

successful packing of 360° DWs of identical circulation at adjacent notches can be achieved with smaller inter-notch distances.

The results in this section supports the hypothesis we constructed earlier while packing opposite circulation 360° DWs: Packing density increases with notch depth. Depth and area of notches both play a role in the closest packing.

F.   Data storage applications of 360° DWs

1.   Constructing data bits via 360° DWs

We can use the circulation of 360° DWs to code for data bits, e.g., 1 when a CW 360° DW is pinned at a given notch and 0 when a CCW 360° DW is pinned at the notch.

We can also use the presence or absence of a 360° DW at a notch to code for a 1 or a 0, e.g., 1 when a 360° DW (regardless of circulation) is pinned at the given notch and 0 when no 360° DWs are pinned at the notch.

In either case, we can pack as many bits on given nanowire as the number of 360° DWs we place on it. This number corresponds to the number of notches in the closest packing configurations we have formerly shown.

2. *Writing mechanism*

We have demonstrated the mechanisms for nucleating 360° DWs and for opposite circulation and identical circulation packing of 360° DWs. As we mentioned earlier, these mechanisms can be realized via the tip of an AFM or via placing nanowires perpendicular to the plane of the ferromagnet but not necessarily in contact with it. In realizing the mechanisms, the field values would need to be adjusted given that we set our simulations at 0 temperature, ignored any anisotropy and elasticity contributions, and did not include roughness.

3. *Reading mechanisms*

Constructing a reading mechanism for 360° DWs on a nanowire is challenging.

i) Suggestions for reading mechanisms

For a mechanism that detects the presence and absence of 360° DWs at a notch: We can use a magnetic junction unit, like that of racetrack memory[11], to detect changes in its tunnel magnetoresistance when a 360° DW, which is moving under spin current, crosses the read

pad.

We can also use a mechanism to detect resistance change on the nanowire whenever there is a 360° DW at a notch, since the resistance changes when there exists a 360° DW. We may call such mechanism a resistance-meter or, more concisely, a *resistometer*.

ii) Disadvantages of each mechanism

Given the depth and the area of notches, moving 360° DWs under spin current in order to read them may cost so much spin transfer torque and hence energy that the mechanism may render the device inefficient and disadvantageous in comparison to existent alternatives.

With regards to resistometers modern technology does not allow resistance readings at nanometric distances in an efficient way. Although we can devise a method using an AFM or an MFM, this is inefficient in energy and hence disadvantageous.

G.   Summary

Notches lower the energy along a nanowire and act as pinning sites. By using appropriate geometry of notches, we can very closely pack 360° DWs on a nanowire via only an in-plane circular field.

The packing procedure takes more number of steps, and hence more energy, for the identical circulation packing than for the opposite circulation packing, even though the identical circulation packing proposes a higher density information storage.

F. I. Kaya

III.   CURVATURE AND ITS EFFECTS ON DW PINNING

We can use curvature in order to control the pinning sites of DWs on a ferromagnetic nanoring. We have studied the effect of curvature on the pinning of DWs by using elliptical ring ferromagnets. We applied on each elliptical ring ferromagnet an elliptical field to move the DWs in the ferromagnet, while we recorded the energy attributed to each DW position. In order to do this we explored initializations along singular axes. We also explored vortex runs and de-pinning and re-pinning of 180° DWs at sites with different curvature.

A.   Background

1.   *Previous Work*

Scientists, who have written the relevant literature, have assumed that curvature on a nanowire implies pinning of DWs, although very limited work explicitly discusses pinning and curvature.

The pinning effects of curvature have previously been studied by Lewis et al., showing that curved sites on a wire act as potential wells and that it takes a higher pinning field to pin DWs at sites of lower (radius of) curvature.[28] In addition, Castano et al. have studied magnetization reversal in elliptical nano-metric ferromagnets and demonstrated switching of onion states (Fig. 46).[29] Although they use the higher curvature sites on an ellipse as DW pinning sites, as in Fig. 46, they do not present any conclusions regarding curvature or relevant DW pinning.
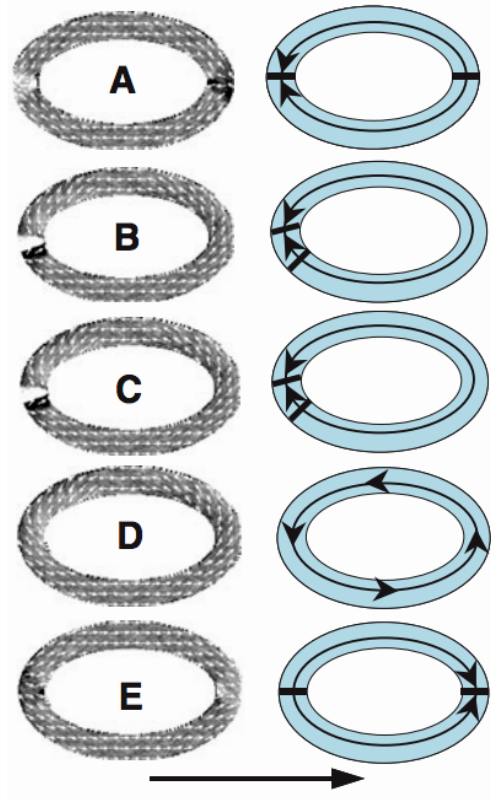
FIG. 46. Switching of onion states on an elliptical ring ferromagnet.[29] An in-plane field in $\hat{x}$ switches magnetization of the ferromagnet from the state in (A) to the state in (E). The 180° DWs in state (A) have their moments point mostly in $-\hat{x}$. The 180° DWs in state (E) have their moments point mostly in $\hat{x}$ as coerced by the in-plane field.

2. Simulation details

By using the term *ellipse*, we refer to structures with eccentricity $A/B \geq 1$, including circles. The elliptical ring nanowires in this section are all of 90 nm width, e.g., 900 nm outer diameter and 810 nm inner diameter for a circle (Fig. 47). r is a function of θ, the angle between the symmetrical center of the ellipse and the point of calculation on the elliptical ring. See Section 1 for details on curvature.

In this section, we use OOMMF plots of ferromagnets in their given state, where the color scale indicates the divergence of moments: Grey points along the structure, black towards the outside ($\hat{r}$), and white towards the center ($-\hat{r}$) (Fig. 48).

F. I. Kaya
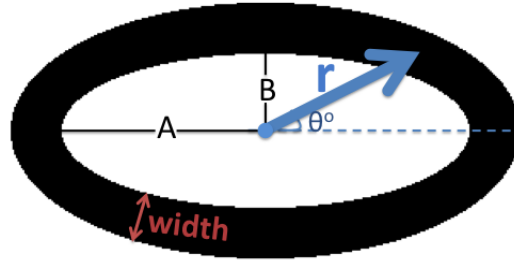
FIG. 47. Sample elliptical ring nanowire
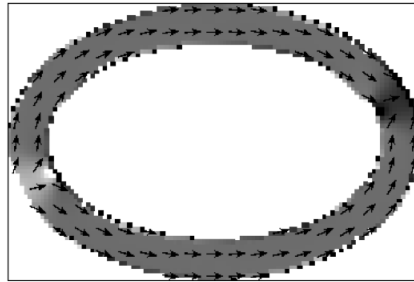
FIG. 48. Sample OOMMF divergence plot of an elliptical ring nanowire

B. Simulated Elliptical Field

In the remaining sections we mention elliptical fields, which we coded in OOMMF, which are useful to study elliptical ferromagnets, and which are not yet realizable. In thinking, we prefer to draw an analogy between a circular field created by passing current through a nanowire that is centered at the symmetrical center of the ellipse and an elliptical field that is centered likewise.

Fig. 49 is the OOMMF plot of an elliptical (Zeeman) field in-plane with the ferromagnet. The field decreases by $1/r(\theta)$, where $r(\theta)$ is the elliptical radius, as described in section 1. (See Appendix E for code details).

F. I. Kaya
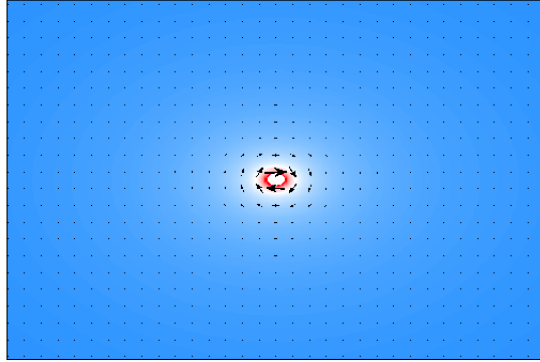
FIG. 49. Plot of Zeeman (external) field. The color scale varies from red (maximum field magnitude) to blue (minimum field magnitude).

C. Initializations and Relevant Energy Considerations

1. Initializations along singular axes

In this subsection we consider initializations along singular axes, that is at $\theta = 30°, 45°$ and $60°$ in polar coordinates.

A) Relaxation of DWs to sites of higher curvature

Let us consider a run initialized at $\theta = 60°$ (Fig. 50).

In Fig. 50 we capture a singular axis initialization at $\theta = 60°$. Initially, all moments point in random directions (Fig. 50a). Once the in-plane field is turned on, they line up with the field at $60°$ (Fig. 50b). Once the field is turned off, the moments relax to a state with two $180°$ DWs at a lower angle than $60°$ (Fig. 50c).

The red vector in Fig. 50 points from the symmetrical center of the ellipse to the outer edge of the ellipse; it points along a $180°$ DW. This red vector $\mathbf{r}$, as shown in Fig. 51, lies at

70
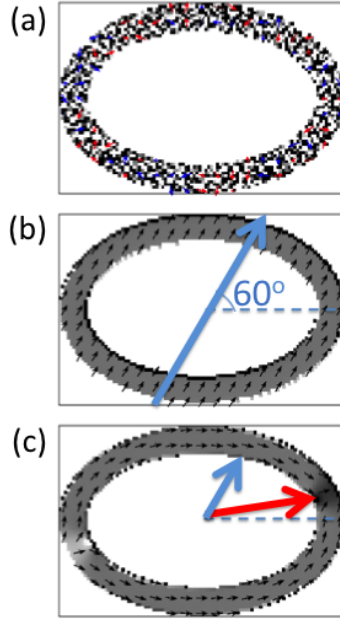
FIG. 50. FIG. Initialization at $\theta = 60°$ (a) Initially, each moment points in a random direction. (b) Moments line up with the in-plane field at 60° as marked with the blue arrow. (c) Moments relax to the state with two 180° DWs after the field is turned off. The 180° DWs sit at a lower angle (marked by the red arrow) than at 60° with the horizontal (marked by the blue arrow).

$\theta = 15°$ degrees with respect to $\hat{x}$ (at 0°). We refer to the angle $\theta = 15°$, at which the DW lies, as the *DW angle.*
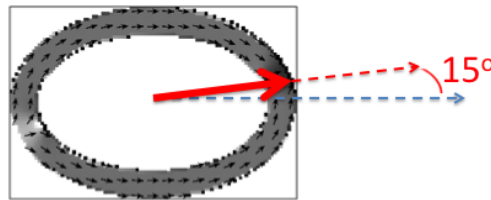
FIG. 51. DW angle at 15°. The red solid arrow points from the elliptical center towards $M_{z,max}$. The red dashed arrow points uni-directionally with the red solid arrow. The blue arrow points in $\hat{x}$. The divergence plot is of a relaxed run after being initialized at $\theta = 60°$ on an ellipse with $A/B = 1.5$.

Next we examine the initializations at $\theta = 60°$ for different A/B ratios (Fig. 52).

Observing the relaxed states after initialization at $\theta = 60°$ in Fig. 52, we can trace a pattern,
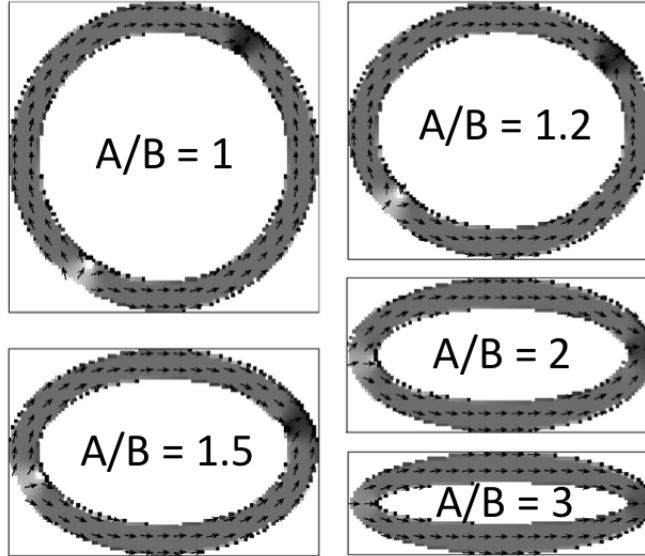
FIG. 52. Ellipses with variable A/B initialized at $\theta = 60°$. The divergence plots are of states after relaxation.

where the DW angle is lower for higher A/B.

The exponential pattern in Fig. 53 shows that as A/B ratio increases, DWs tend to pin at lower angles in the onion state right after initialization. The states correspond to those in Fig. 52.

For $A/B = 1$, the DWs remain at the initialization angle at $\theta = 60°$. Since curvature is constant along the entire conduit, the DWs have no preference to move to another site on the conduit. For $A/B = 1.2$, as the structure relaxes, DWs migrate to a site with higher curvature as a result of PEM. The same happens for higher A/B, except DWs move even lower on the vertical, eventually reaching approximately $\theta = 0°$ for $A/B = 3$.

We observe the same pattern for initializations along the other singular axes, namely at $\theta = 30°$ and $45°$, as well. We conclude that DWs prefer to pin at sites with higher curvature,
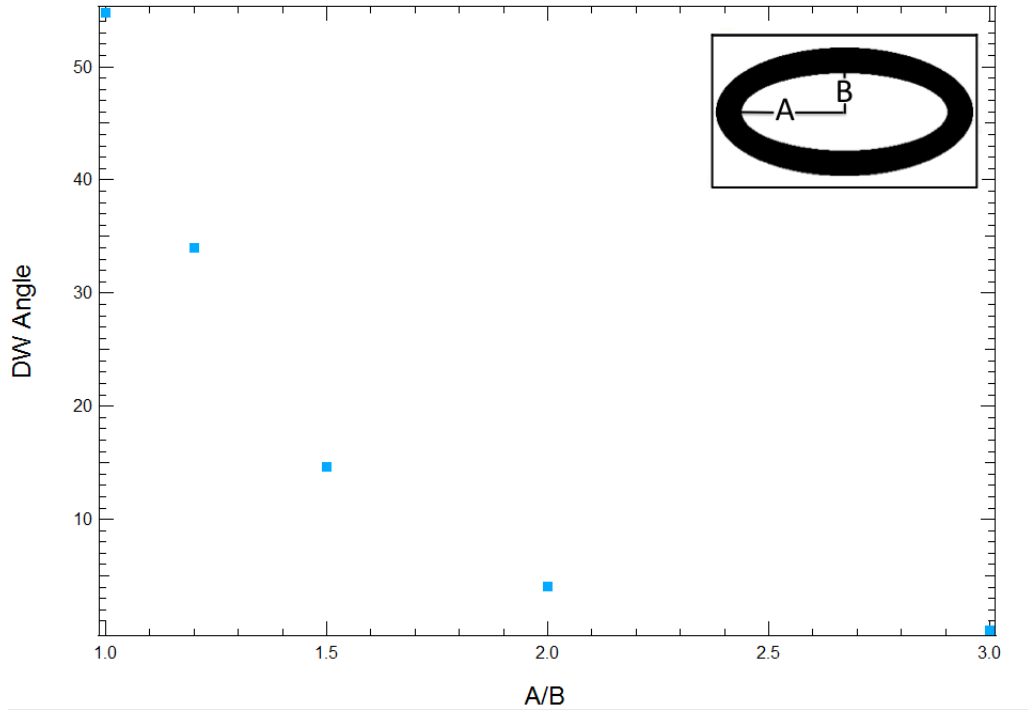
FIG. 53. Plot of DW angle vs. A/B ratio for 60° initializations. The DW angles are measured for $M_{z,max}$ on the outer half of the width of the elliptical conduits.

during initialization.

B) Energies after relaxation
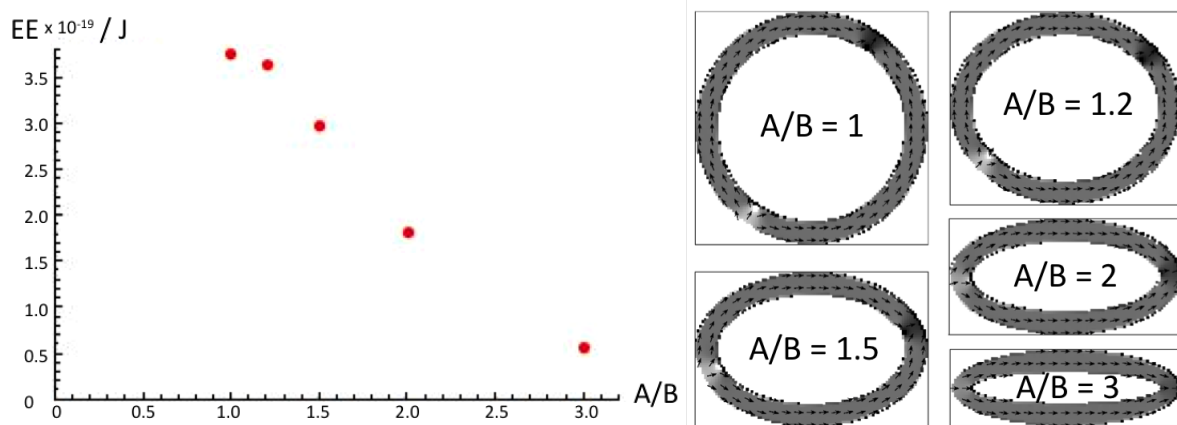
FIG. 54. Plot of EE vs. A/B Ratio for 60° initializations.

F. I. Kaya

Fig. 54 presents that EE, calculated at the conclusion of initialization runs, decreases as A/B increases. Hence, EE is lower when DWs pin at a lower curvature.

Looking at the results in this section and recalling the findings of Lewis et al.,[28] we predict that higher curvature means lower total energy. To test this, we further investigate energy as a function of A/B and curvature as follows.

2. Initializations along natural axes

In this subsection, we consider initializations along major and minor axes, that is at $\theta = 0°$ and $90°$ in polar coordinates. DWs initialized along natural axes stay along these axes.

A) Energies after relaxation
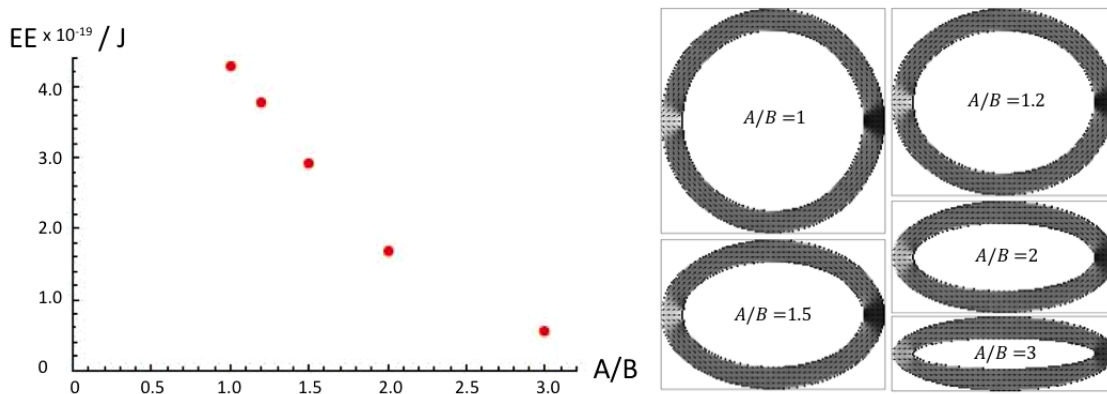
FIG. 55. Plot of EE vs. A/B Ratio for $0°$ initializations

In each of Fig. 55 and Fig. 56, we compare EE among 5 conduits with DWs pinned at the same angle. This lets us see a clear trend of EE decrease as curvature at DW pinning sites increases; the higher the curvature at where the DWs pin, the lower the EE. We contemplate

74
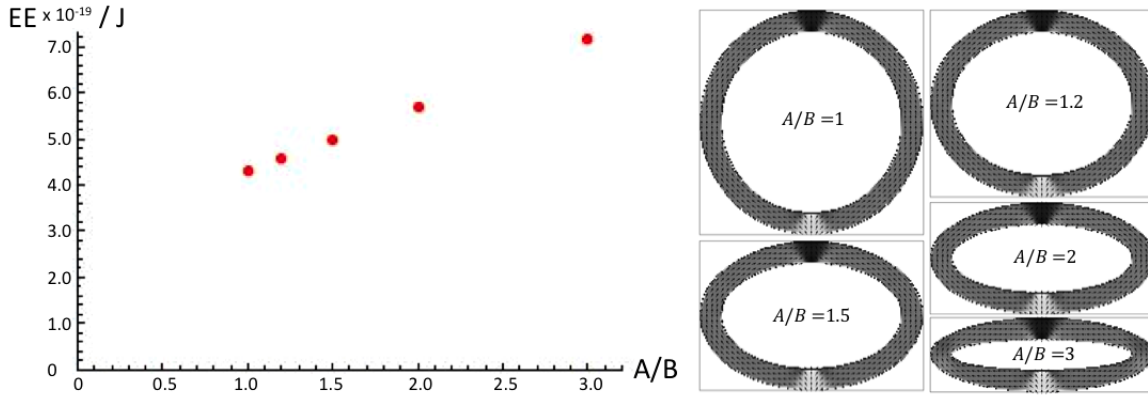
FIG. 56. Plot of EE vs. A/B Ratio for 90° initializations

the reason is that moments go through less rotation at a DW when curvature is higher at a pinning site.
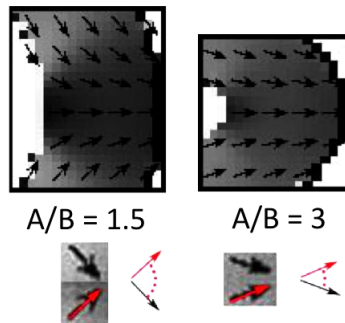
FIG. 57. Rotation of moments along a 180° DW on two conduits with different curvature

In Fig. 57 we observe that moments rotate less along a 180° DW when the DW is pinned at a higher curvature, e.g., along $\theta = 0°$ on an elliptical conduit with $A/B = 3$, than when it is pinned at a lower curvature, e.g., that with $A/B = 1.5$.

D. Vortices and Relevant Energy Considerations

In this section we consider EE and ME on ellipses with moments aligning entirely CCW. We aim to understand the energies in the ellipses without the DWs present so that once we read the energies with the DWs present, we can subtract the vortex energies in order to develop a better conclusion.
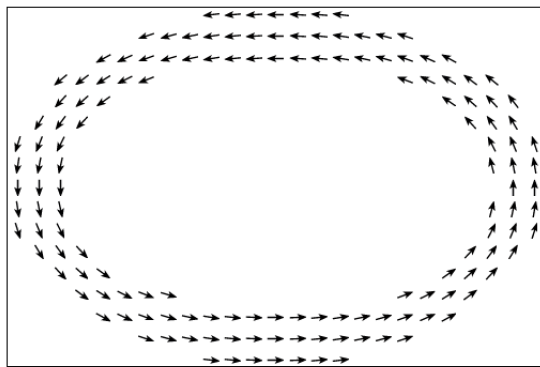
FIG. 58. CCW vortex state of elliptical conduit with $A/B = 1.5$

In Fig. 58 all moments align CCW. These states are simulated under CCW elliptical fields created by applying 18.1 mA at the center of each ellipse. We call this a CCW vortex. Next, we investigate elliptical conduits with the five A/B ratios we have been studying, separately for *fixed* (of constant length) major and minor axes.

Fig. 59 demonstrates all of the geometries we use in elliptical ring ferromagnet runs. Next we explore exchange and magnetostatic energies of these conduits.

In Fig. 60 and Fig. 61 exchange and magnetostatic energies of elliptical conduits in vortex states are plotted respectively; in both figures pluses represent ellipses with constant minor

F. I. Kaya
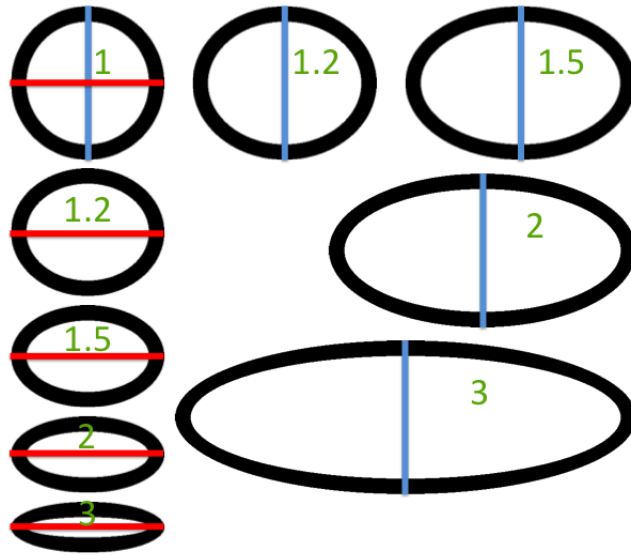
FIG. 59. Conduits with fixed minor axis diameter vs. those with fixed major axis diameter. The axis diameters are fixed at 900 nm. The eccentricities (A/B) are indicated in green. With increasing eccentricity: ME increases for fixed minor axis (blue) and decreases for fixed major axis (red), whereas EE increases for both.
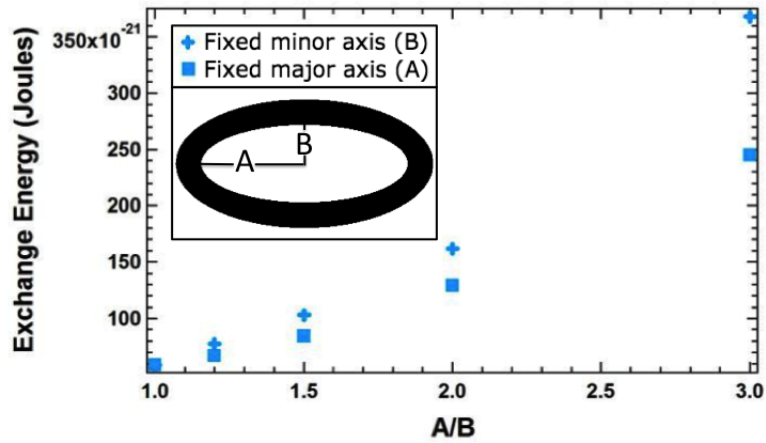
FIG. 60. Plot of EE vs. A/B of elliptical ferromagnets in vortex state. Pluses indicate elliptical ferromagnets of 900 nm minor axis diameter. Squares indicate those of 900 nm major axis diameter.

axis diameter. Squares represent constant major axis diameter. These plots suggest that without any DWs, the EE increases with increasing A/B. This makes sense since for instance, at $A/B = 3$ there is a greater rate of change of curvature between the major and
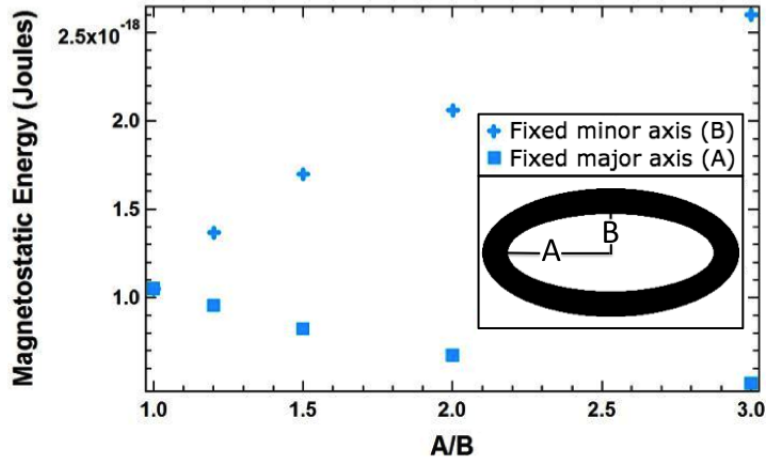
FIG. 61. Plot of ME vs. A/B of elliptical ferromagnets in vortex state. Pluses indicate elliptical ferromagnets of 900 nm minor axis diameter. Squares indicate those of 900 nm major axis diameter.

minor axes of the elliptical conduit, costing higher EE for the moments to align with one another. On the other hand, ME increases with increasing area of ferromagnet. At sites with changing curvature, moments do not completely line up with the geometry. Then, stray field exists as magnetization points outwards from the boundaries. Conduits with fixed minor have more area along which such stray field exists. Therefore, there is a higher ME cost for conduits with higher area at given A/B.

Via the studies in this section, we conclude that for fixed minor axis runs, ME and EE increase with increasing eccentricity, and that for fixed major axis runs, ME decreases and EE increases with increasing eccentricity. The cost of ME depends on the curved area of the nanowires, while moments tend to align with the geometry, whereas the EE cost is due to the rate of change of curvature, while moments tend to align with one another.

E.   Pinning Strength

In this section we investigate how the strength of the pining field changes with curvature. In order to do this, we first initialize the DWs along a natural axis, which nucleates two 180° DWs. Then, we apply an elliptical field to adjoin the two 180° DWs and record the energies as DWs move.

We start by calculating the depinning field, which is the field required to de-pin 180° DWs from their locations along natural axes, where they pin during initialization, to carry them successfully over to the next natural axis, and to re-pin them there.
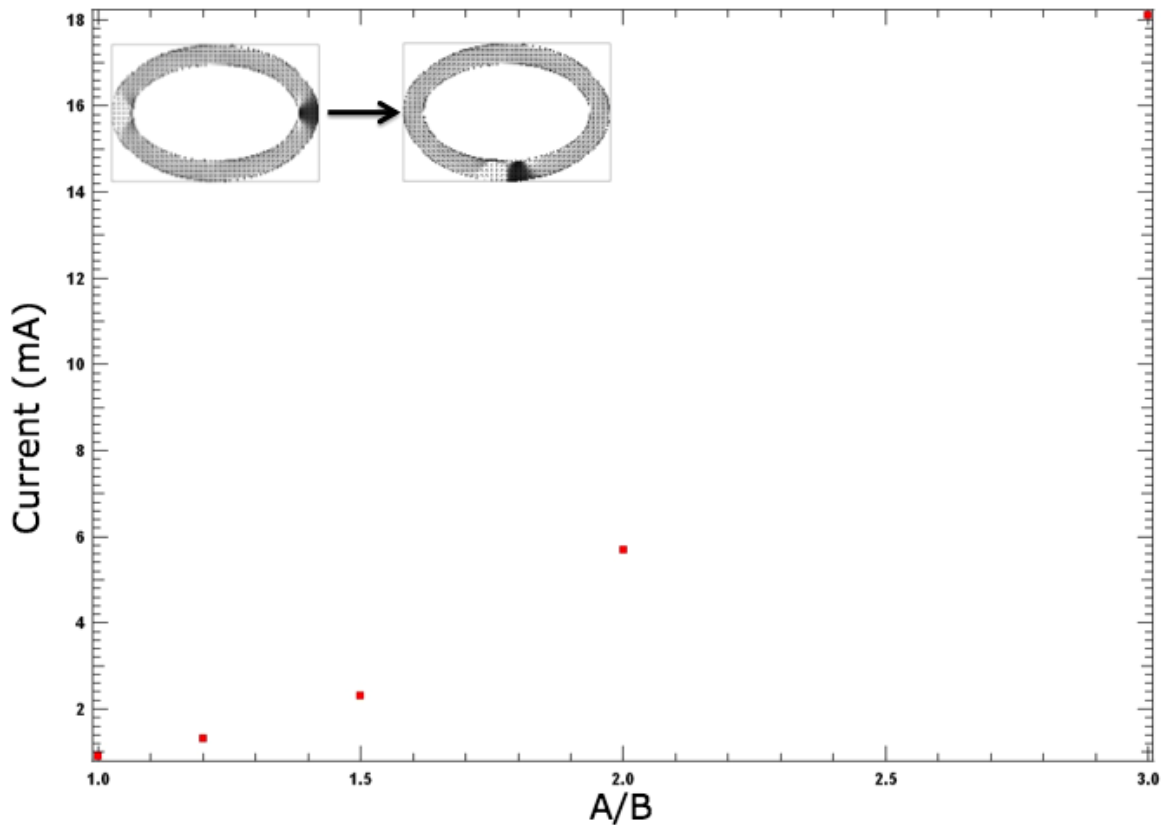
FIG. 62. Plot of depinning field strength vs. A/B on conduits with fixed major axis

F. I. Kaya

In Fig. 62 an increasing field strength is required as curvature at pinning sites increases; e.g., $A/B = 3$ has higher curvature along the major axis where the 180° DWs are pinned than $A/B = 1$.

On these depinning runs, we explore how EE changes. We apply 18.1 mA on each ellipse since we have calculated (as presented in Fig. 62) that it has sufficient strength to depin all of the ellipses in question.
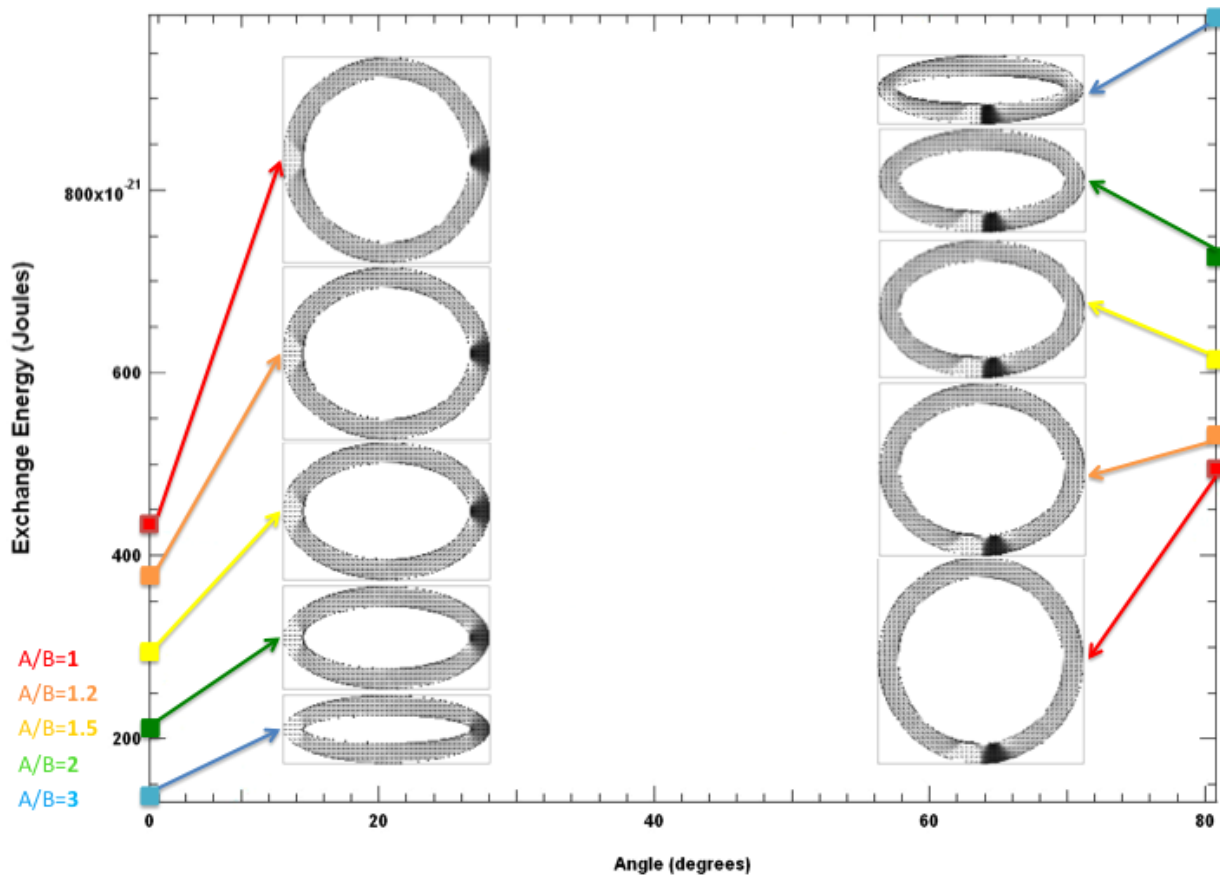
FIG. 63. Plot of EE vs. A/B for depinning runs on conduits with fixed major axis. In each run 18.1 mA is applied at the center of the ellipse, creating an elliptical CCW field and successfully depinning and subsequently re-pinning each 180° DW.

In Fig. 63 EE is plotted at the beginning and at the end of a depinning run for each of the five geometries. The major axis diameter is kept constant at 900 nm among the geometries

of elliptical conduits. The plot shows that EE increases for each depinning run as, at each geometry, 180° DWs move from the old pinning sites along the major axis to the new pinning site along the minor axis, where (the radius of) curvature is lower in comparison to that along the major axis. This agrees with our prediction that the higher the curvature, the lower the EE; moments along DWs rotate through smaller angles with increasing curvature.

Up until now, we have considered energies in the initial and final steps of a depinning run. At these two steps, the DWs we consider are relatively stable since they are pinned along the major or minor axes. Next, we want to explore states with de-pinned DWs.

F.   Curvature Effects on Energies of Depinned DWs

As we study depinned DWs, we aim to overcome the depinning energy barrier that exists between a state with pinned DWs and a state with depinned DWs. This energy barrier that exists between two *stable states*, between the state when DWs are pinned along natural axes and the state when DWs are depinned, is due to the depinning of DWs under the elliptical field, and it instigates what we call a *metastable state* of the system (Fig. 64 and Fig. 65).

To overcome the metastable state, and hence the energy barriers in Fig. 64 and Fig. 65, we skip to the 100th time step in each run. It is the time step at which each 180° DW is depinned and mobile, moving under the elliptical CCW field towards the next natural axis. This lets us avoid the metastable DW states that occur during depinning.

In order to draw a meaningful conclusion about the depinning energies, we next examine a combination of energy vs. curvature plots such as normalizing (dividing by the area of the
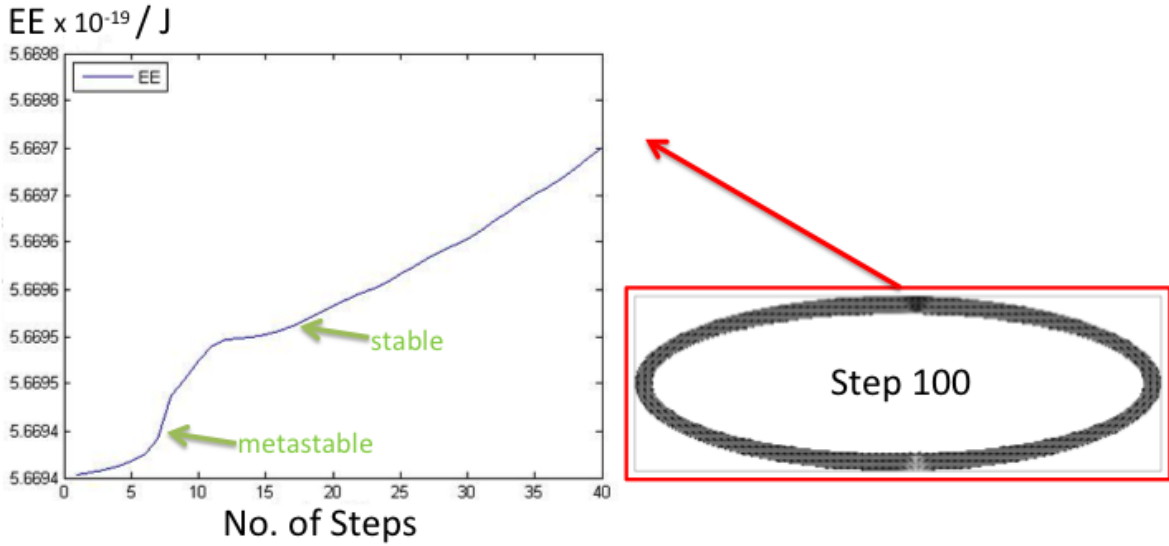
FIG. 64. EE of metastable DW state during depinning
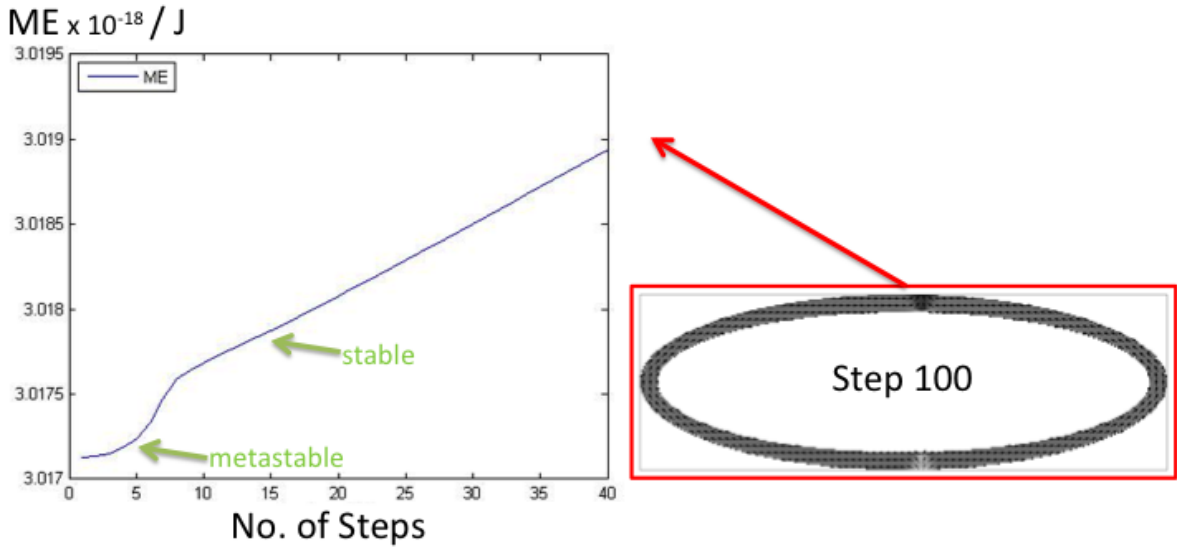
FIG. 65. ME of metastable DW state during depinning

ferromagnet) or subtracting the vortex state energies (to discount moments other than those along the DWs). The plots in the following sections are mostly a result of our trying to understand the energies with respect to curvature. Although we do not have the complete story regarding EE and ME as functions of curvature, we present our current conclusions. (See Appendix C for code details of plotting curvature and Appendix D for code details of

F. I. Kaya

plotting energies).

1. *Exchange Energy*
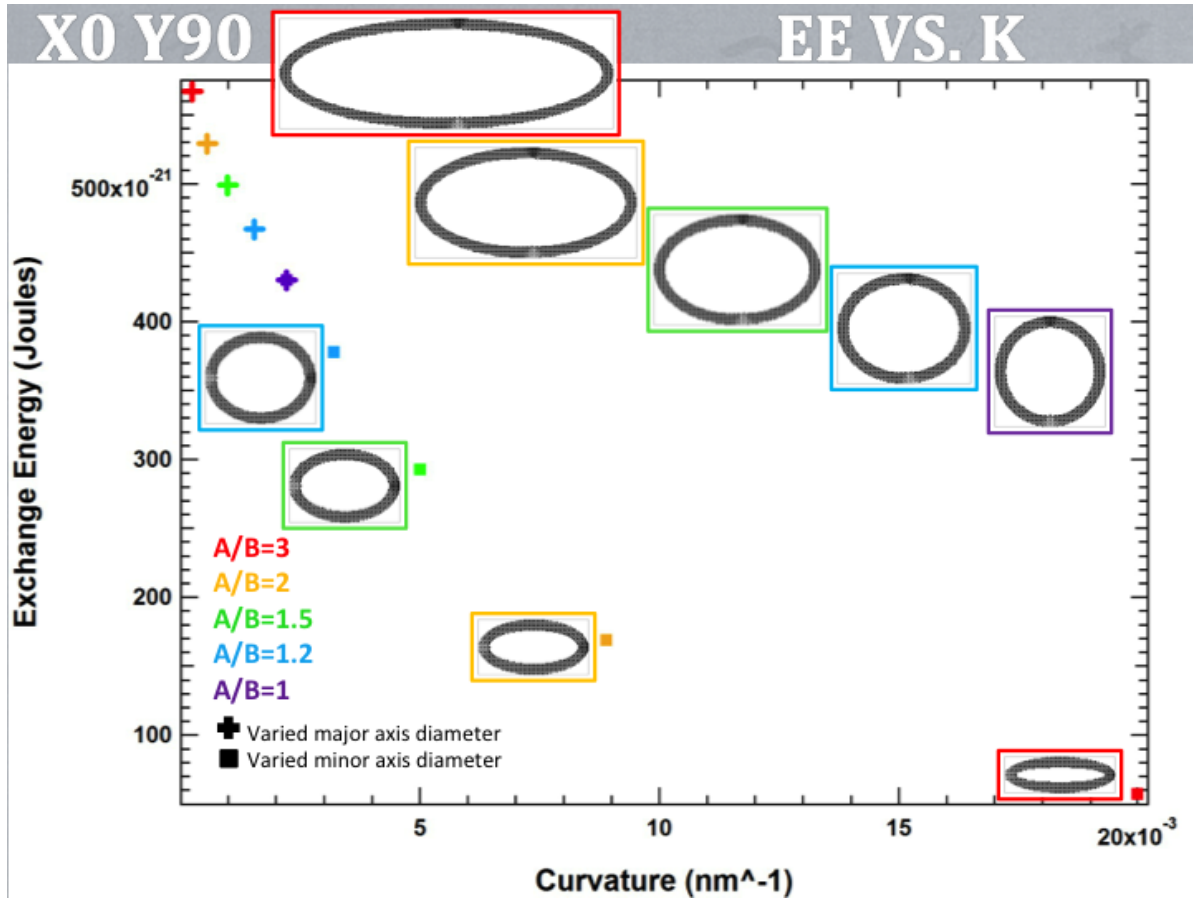
FIG. 66. Plot of EE (in J) vs. curvature (κ in nm^{-1}) for fixed major initializations along $\theta = 0°$ and fixed minor initializations along $\theta = 90°$. The divergence plot of each elliptical ferromagnet is given in proximity of its own EE vs. κ value, framed in the same color.

In Fig. 66 we present the plot of exchange energy (EE) vs. curvature for given initializations; along $\theta = 0°$ for fixed major ($X0$) and $\theta = 90°$ for fixed minor ($Y90$). By plotting $X0$ with $Y90$, we can study the gradual increase in curvature at DW sites. The plot pattern suggests that EE decreases with increasing curvature, agreeing with our prediction.

In Fig. 67 we present the plot of EE vs. curvature for all initializations; those along $\theta = 90°$
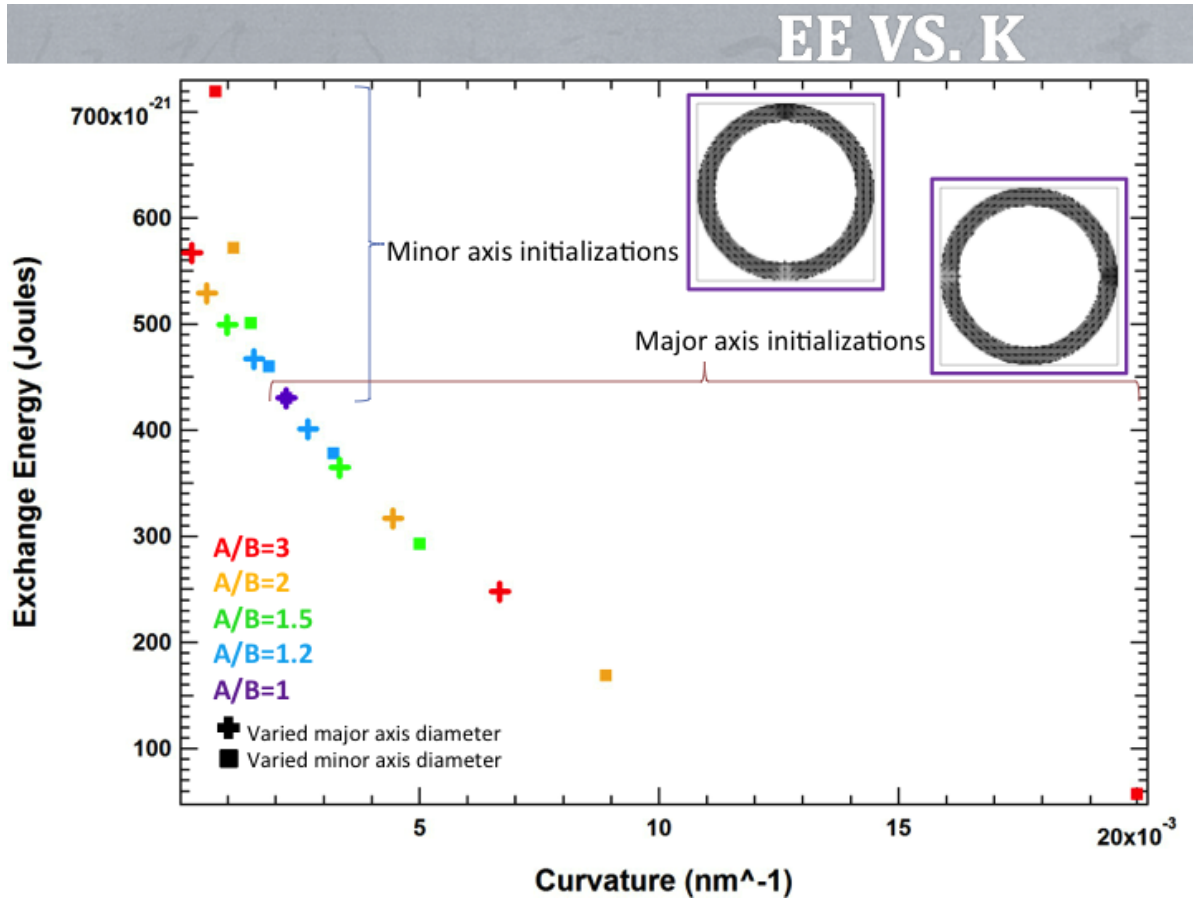
FIG. 67. Plot of EE (in J) vs. curvature (κ in nm^{-1}) for fixed major and minor initializations along $\theta = 0°$ and fixed major and minor initializations along $\theta = 90°$

for fixed major ($X90$) and $\theta = 0°$ for fixed minor ($Y0$) in addition to the ones captured in Fig. 66. In order to better understand the function that maps curvature to EE, we next fit an exponential to this plot.

In Fig. 68 we present the plot of EE vs. curvature for all initializations. The plot suggests that EE decreases exponentially with increasing curvature on elliptical ring ferromagnets of 90 nm width, 900 nm fixed diameter, and of variable area and A/B.

In Fig. 69 we present the plot of EE vs. curvature for all initializations after we normalize each EE by dividing it by the magnetized area (in nm^2) of each ferromagnet. The inner plot

84
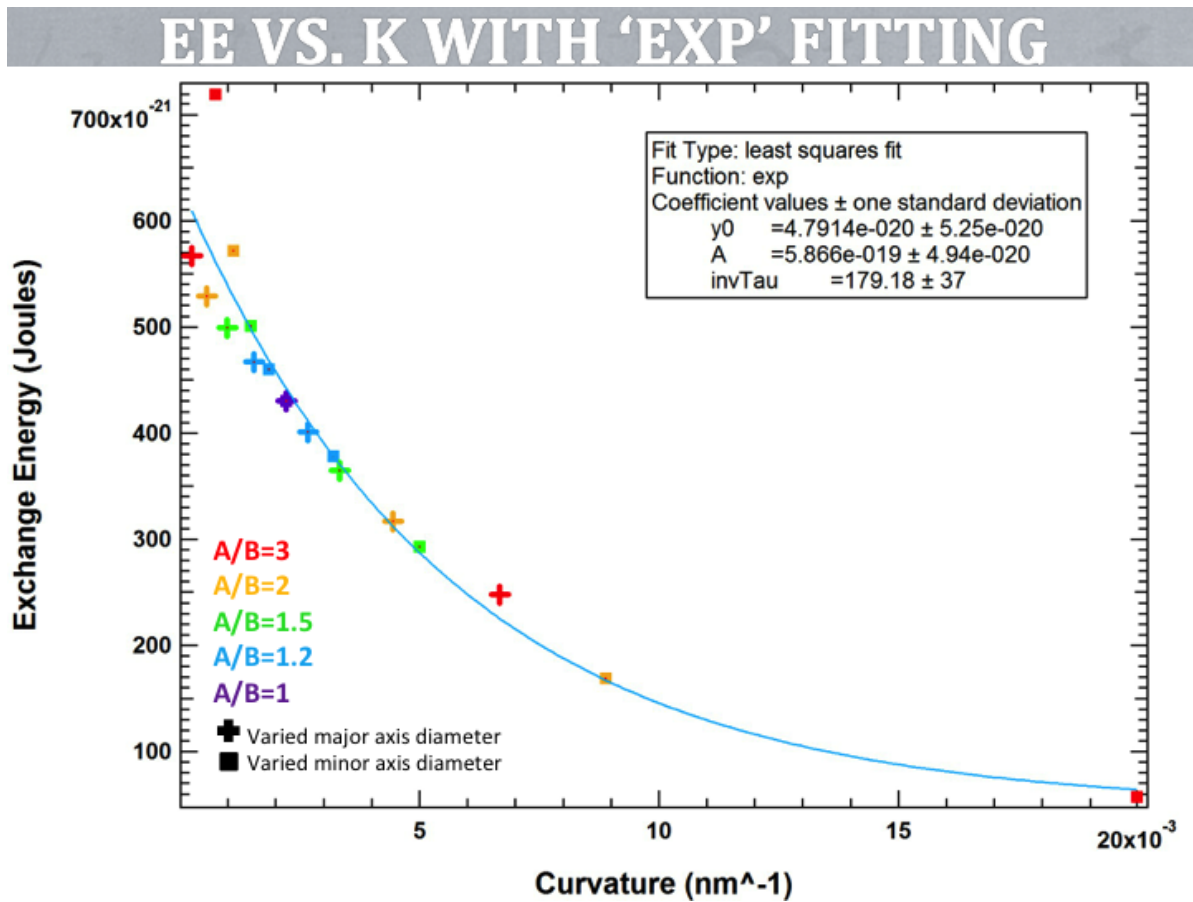
FIG. 68. Exponential fitting on the plot of EE (in J) vs. curvature (κ in nm^{-1}) for all initializations

isolates the plots of $X90$ and $Y0$, which seem to trace an exponential pattern of their own.

We suppose the curving of $Y90$ (marked with plus signs on the lower right side of the larger plot) may be due to curvature not being apparent at the site of DWs at 100th step as a consequence of geometry (during this step, the DWs are at sites of low curvature); e.g., the pixelation of the program we use may not have been sufficient for accurate curvature. (See Appendix F for the code that plots the geometry).

In Fig. 70 we present the plot of EE vs. curvature for all initializations after we subtract the EE of the vortex run of each geometry. We attribute the curving of $Y90$ to the program we use to create the simulation geometries. Subtracting the vortex EE lets us discount the EE
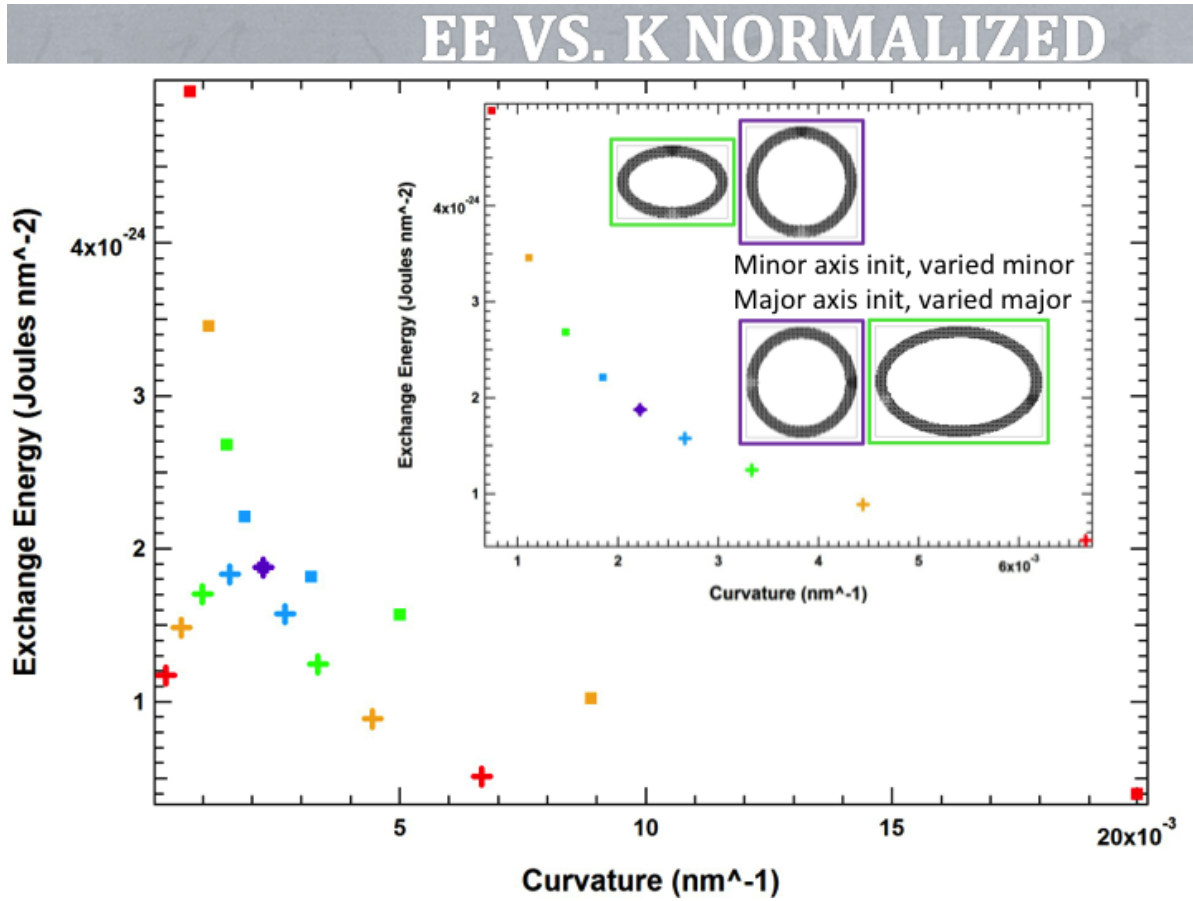
FIG. 69. Normalized plot of EE (in J) vs. curvature (κ in nm^{-1}) for all initializations

risen by moments along the ellipses that align, e.g., as the moments in a vortex state. This way, we focus only on the DW contribution in the EE. Subtracting the vortex EE reduces the exponential nature of the EE vs. κ plot and lets us conclude that EE along DWs decrease -almost linearly- with increasing curvature.

2. Magnetostatic Energy

In Fig. 71 we present the plot of magnetostatic energy (ME) vs. curvature for given initializations that are along $\theta = 0°$ for fixed major ($X0$) and $\theta = 90°$ for fixed minor ($Y90$). By plotting $X0$ with $Y90$, we study the gradual increase in curvature at DW sites. The plot pattern suggests that ME decreases with increasing curvature although not linearly. Again,
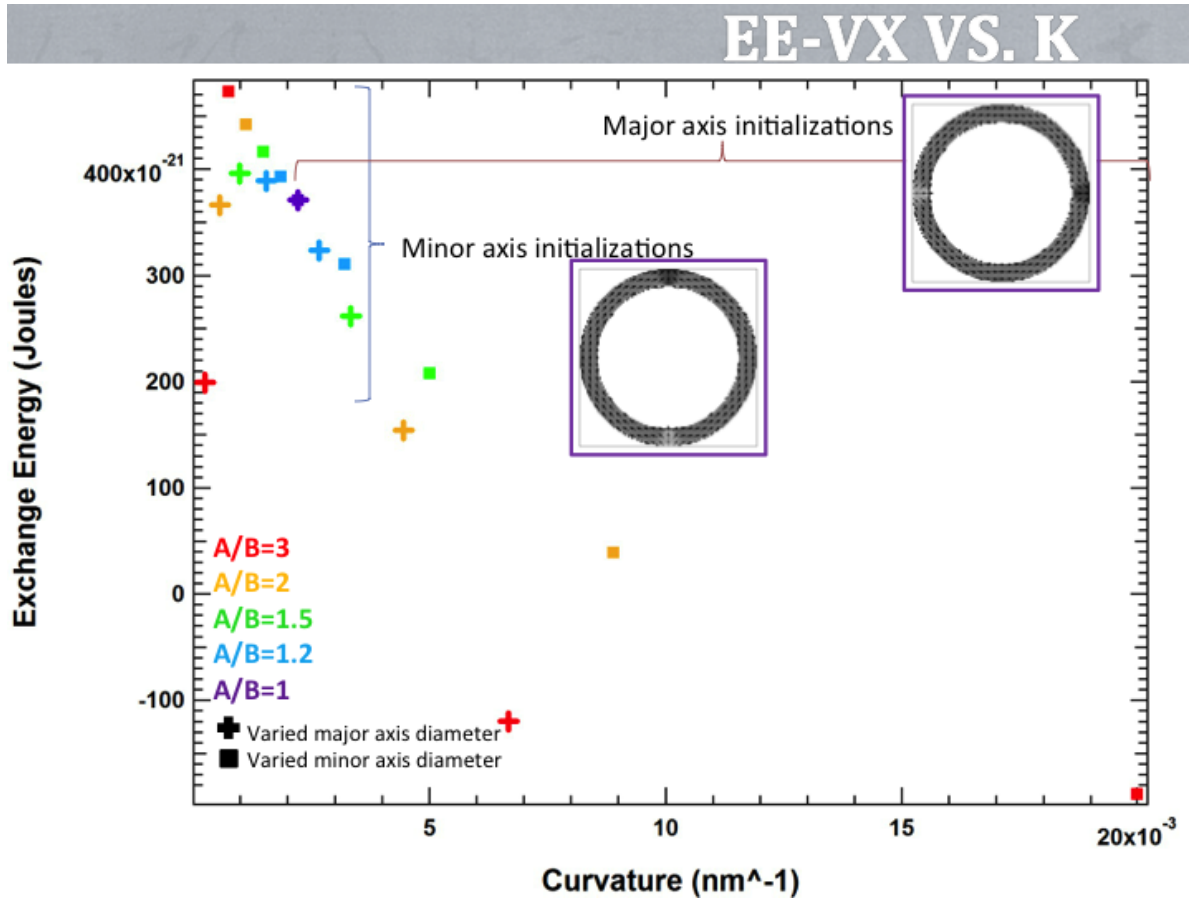
FIG. 70. Plot of EE with subtracted vortex EE (in J) vs. curvature (κ in nm^{-1}) for all initializations

the curving of the data points (see the plus marks on the upper left corner) may be due to a glitch in the program we use to create the simulation geometries. We intend to further investigate ME patterns, although so far, after subtraction of vortices and normalization on either of $X0$, $X90$, $Y0$, and $Y90$, the only noteworthy pattern we have found is the one in Fig. 71.

G. Summary

EE decreases as curvature increases, and so DWs pin at sites of higher curvature. DWs move as they form, and they lower their energy by moving towards the major axis, which has higher curvature and hence lower EE. By varying curvature along a nanowire, we can create pin-
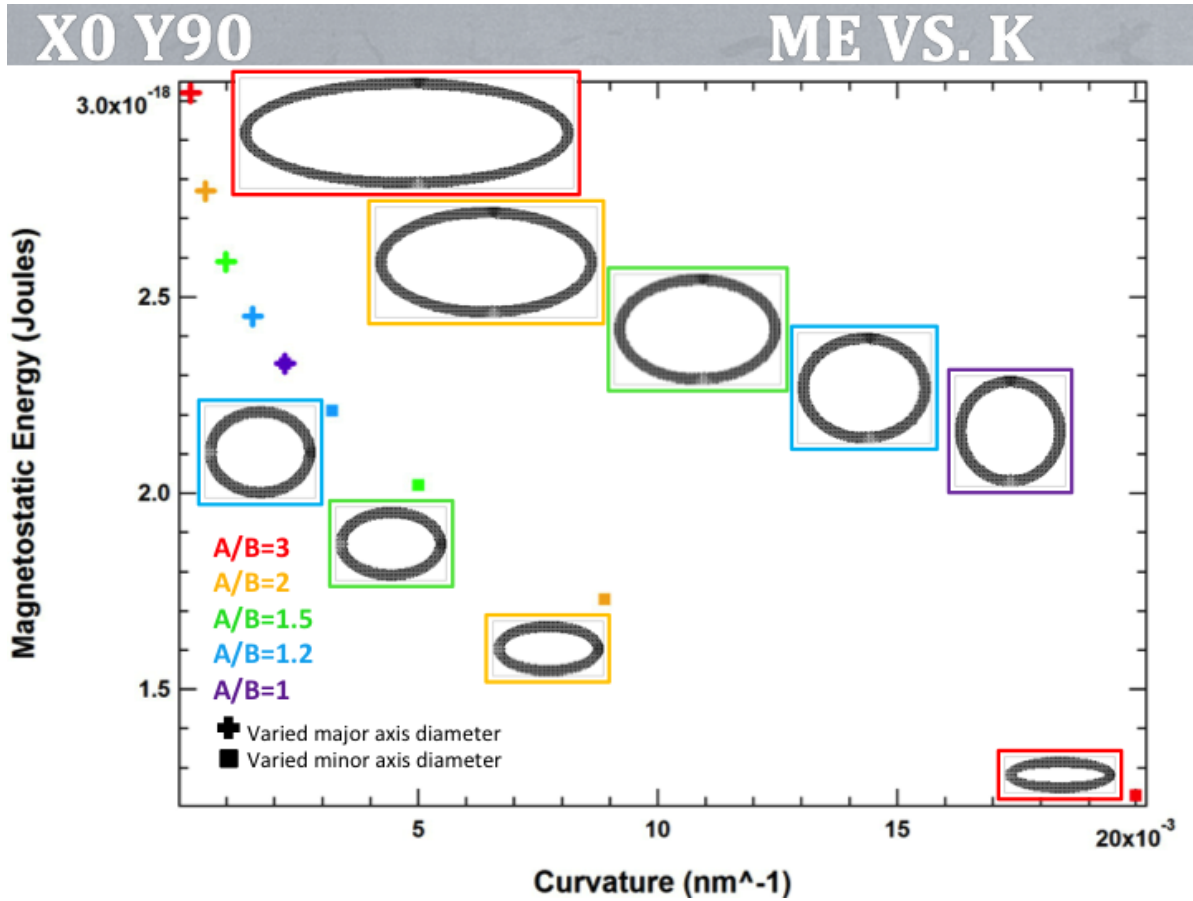
FIG. 71. Plot of ME (in J) vs. curvature (κ in nm^{-1})

ning sites of varying pinning strength, e.g., which we can then use as multistate memory bits.

We aim to continue studying ME as a function of curvature in order to complete our under-standing of ME with respect to curvature.

IV.   CONCLUSION

In this thesis, we examined the physics encompassing the Domain Walls (DWs) in linear and curved nanowire ferromagnets. Via simulations: We demonstrated our new technique of nucleating 360° DWs and explained the topological phenomena surrounding both 180° DWs and 360° DWs during their nucleation. Nucleation of a 360° DW proceeds via a circular

F. I. Kaya

magnetic field and does not require contact: We can achieve high-density data storage on a ferromagnet by applying a combination of circular magnetic fields in the vicinity of the ferromagnet. Furthermore, we studied the consequences when we introduce notches and curvature to the nanowires; Exchange Energy is lowered where there are notches or higher curvature than the surroundings. Consequently, we inspected the trade-off of energies along sites with notches or high curvature and displayed how DWs pin at these areas, mostly due to the lowering of Exchange Energy.

REFERENCES

[1] M. J. Donahue and D. G. Porter, *OOMMF User's Guide, Version 1.0* (Interagency Report NISTIR 6376 (National Institute of Standards and Technology), MD, USA, 1999).

[2] T. Yang, N. R. Pradhan, A. Goldman, A. S. Licht, Y. Li, M. Kemei, M. T. Tuominen, and K. E. Aidala, Appl. Phys. Lett. **98** (2011).

[3] S. Blundell, *Magnetism in Condensed Matter* (Oxford University Press Inc., NY, USA, 2001).

[4] A. S. Licht, *A Computational Micromagnetic Study of Controlling Vortex Chirality in Ferromagnetic Nanorings* (Mount Holyoke College, 2011).

[5] C. L. Chien, F. Q. Zhu, and J. G. Zhu, Phys. Today **60** (2007).

[6] A. Pushp, T. Phung, C. Rettner, B. P. Hughes, S. Yang, L. Thomas, and S. S. P. Parkin, Nat. Phys. **9** (2013).

[7] S. Zhang, Q. Zhu, C. Mu, Y. Zhang, Q. Liu, and J. Wang, Journal of Mag. and Mag. Mat. **347** (2013).

[8] E. Barati, M. Cinal, D. M. Edwards, and A. Umerski, Phys. Rev. B **90** (2014).

[9] S. Konishi, IEEE Trans. Magn. **19** (1983).

F. I. Kaya

[10] J. Zhu, Y. Zheng, and G. A. Prinz, J. Appl. Phys. **87** (2000).

[11] S. S. P. Parkin, M. Hayashi, and L. Thomas, Science **320** (2008).

[12] C. B. Muratov and V. V. Osipov, IEEE Trans. Magn. **45** (2009).

[13] A. L. Gonzalez-Oyarce, Y. Nakatani, and C. H. W. Barnes, Phys. Rev. B **87** (2013).

[14] G. Hrkac, J. Dean, and D. A. Allwood, Phil. Trans. R. Soc. A **369**, 3214–3228 (2011).

[15] M. Diegel, R. Mattheis, and E. Halder, IEEE Trans. Magn. **40**, 2655–2657 (2004).

[16] A. Kunz, Appl. Phys. Lett. **94** (2009).

[17] M. D. Mascaro and C. A. Ross, Phys. Rev. B **82** (2010).

[18] M. Hayashi, L. Thomas, R. Moriya, C. Rettner, and S. S. P. Parkin, Science **320** (2008).

[19] L. Thomas, M. Hayashi, R. Moriya, C. Rettner, and S. Parkin, Nat. Commun. **3** (2012).

[20] Y. Jang, S. R. Bowden, M. Mascaro, J. Unguris, and C. A. Ross, Appl. Phys. Lett. **100** (2012).

[21] L. D. Geng and Y. M. Jin, J. Appl. Phys. **112** (2012).

[22] T. Chen, C. Kuo, A. K. Mishra, B. Das, and J. Wu, Phys. B Condens. Matter **476**, 161–166 (2015).

[23] A. L. Gonzalez-Oyarce, J.Llandro, and C. H. W. Barnes, Appl. Phys. Lett. **103** (2013).

[24] F. I. Kaya, A. Sarella, D. Wang, M. Tuominen, and K. E. Aidala, arXiv:1511.00167v1 (2015).

[25] J. E. Bickel, S. A. Smith, and K. E. Aidala, J. Appl. Phys. **115** (2014).

[26] The nucleation works up to 1/6th of the inter-notch distance away from the target notch.

[27] F. I. Kaya, A. Sarella, D. Wang, M. Tuominen, and K. E. Aidala, AIP Advances **6** (2016).

[28] E. R. Lewis, D. Petit, L. Thevenard, A. V. Jausovec, L. O'Brien, D. E. Read, and R. P. Cowburn, Appl. Phys. Lett. **95** (2009).

[29] F. J. Castano, C. A. Ross, and A. Eilez, J. Phys. D: Appl. Phys. **36** (2003).

Appendix A: Complementary Energy Formulations

Fikriye Idil Kaya[1]

Department of Physics, Mount Holyoke College, South Hadley, MA, 01075,

USA

(Dated: 28 Dec 2015)

I.   DERIVATIONS OF ZEEMAN, EXCHANGE, AND MAGNETOSTATIC ENERGIES

Let us note here that we refer to *Free energy* as the energy contained within the volume of the ferromagnet, available to do work. Mostly, the work done consists of heat dissipated to the environment. Mathematically, the integral over the ferromagnet's volume (for any of the energies described in this Appendix) is equivalent to the integral over all space, since $\mathbf{M}$ is zero outside of the ferromagnet. Thus, we avoid attaching V to the integrals, meaning integrals are over all space unless specified otherwise.

A.   Zeeman Energy

The *Zeeman energy* (ZE) arises from the interaction of a moment with the external field.

Using Maxwell's equation of magnetic fields, namely $\vec{\nabla} \cdot \mathbf{B} = 0$, which implies

$$\vec{\nabla} \cdot (\mu_0(\mathbf{H}_{ext} + \mathbf{M})) = 0 \quad ,$$

we derive

$$\vec{\nabla} \cdot \mathbf{H}_{ext} = -\vec{\nabla} \cdot \mathbf{M} \quad .$$

This equation is important as it gives the relationship between magnetization and the external field; the divergence of the external field lies in the negative direction to the divergence of the magnetization. As a representation, think of a point in space and its infinitesimally close surroundings in a sphere. All of the magnetization vectors in these surroundings point towards the point, so their integral flows into the sphere (is positive as a sum over the spherical surface), whereas the external field vectors point outwards, so their integral flows

out of the sphere (is negative as a sum over the spherical surface).

ZE is minimized when the magnetization of the material aligns with the external field. Over all space, we can write ZE as

$$U_{Zee} = -\mu_0 \int \mathbf{H}_{ext} \cdot \mathbf{M} \, d\tau \quad .$$

As a summary, whenever there is an external magnetic field, $\mathbf{B}_{ext}$, in the vicinity of the material, it costs energy to not have the magnetic moment align with the field. The ZE is sometimes called the *orientation energy E_{ori}*, and we can describe it separately for the spin and orbital components of the magnetic moment such that

$$U_{Zee,s} = -\vec{\mu}_s \cdot \mathbf{B}_{ext} \quad ; \quad U_{Zee,o} = -\vec{\mu}_o \cdot \mathbf{B}_{ext} \quad ,$$

where the negative sign ensures that the more aligned the magnetic moment and the field are (the greater the dot product is in magnitude), the less the energy cost is.

B.   Exchange Energy and Interaction

The reason for ferromagnetism is the phenomenon named *exchange coupling.* Exchange coupling is the interaction between the spin due to all electrons of a particular atom in a material and the spin due to the electrons of the neighboring atoms in the material. The exchange coupling of the magnetic moments of the atoms directly affects the alignment of the moments such that the moments align in the state that minimizes the energy. This energy due to the interaction of adjacent moments is known as the *exchange energy* (EE).

There exists an inherent length scale that sustains exchange coupling; across this length,

exchange coupling has evident effect. This *exchange length* is equivalent to

$$l_{exc} = \left(\frac{2a}{\mu_0}\right)^{1/2} \frac{1}{M_{sat}} \quad,$$

where a is the exchange stiffness constant.[1] The stiffness constant is characteristic of the ferromagnetic material, and the saturation magnetization is the maximum magnetization gained by the material (e.g., when all moments align in parallel with a uniform linear external magnetic field during initialization).[1]

EE is minimized when two moments align in parallel. The contributions to EE can be divided into two; the spin and the orbital. Most text books only give derivations for the spin contribution, and below we discuss these.

The discrete Hamiltonian of the spin exchange energy is

$$\hat{U}_{exc,s} = -\sum_{i>j} 2J_{ij}\, \mathbf{S}_i \cdot \mathbf{S}_j \; d\tau \quad,$$

where J_{ij} is the positive exchange constant between the ith and jth spins, $\mathbf{S}_i$ is the ith spin, and $\mathbf{S}_j$ is the jth spin. This Hamiltonian is named the *Heisenberg Hamiltonian* after Heisenberg generalized the interaction between two spins as a sum of all such interactions.[1,2]

For two spins, we can write

$$\hat{U}_{exc,s} = -2J\, \mathbf{S}_i \cdot \mathbf{S}_j = 2JS^2\, \mathbf{m}_i \cdot \mathbf{m}_j \quad,^{[1]}$$

and integrating over the entire material, we obtain the overall EE such that

$$U_{exc,s} = \int 2JS^2\, (\vec{\nabla} \cdot \mathbf{m})^2 \; d\tau \quad,$$

4

where J is the exchange constant, and the magnetization direction is given by $\mathbf{m} = \mu_0 \mathbf{M}/M_{sat}$

for saturation magnetization M_{sat} and for permeability of free space μ_0.[3]

For the quantum mechanical derivation of J_{ij} and J from spatial and spin states of two elec-

trons besides a through study of quantum mechanics of magnetic materials, see Blundell.[?]

C.   Magnetostatic Energy and Interaction

Magnetostatic interaction of a material is encompassed in its *magnetostatic field, H_{mag}*. The

magnetostatic contribution to total energy arises from the interaction of a moment with the

stray field caused by other moments (Fig. 1). Hence, the magnetostatic field is also called

the *stray field* or the *demagnetization field*.
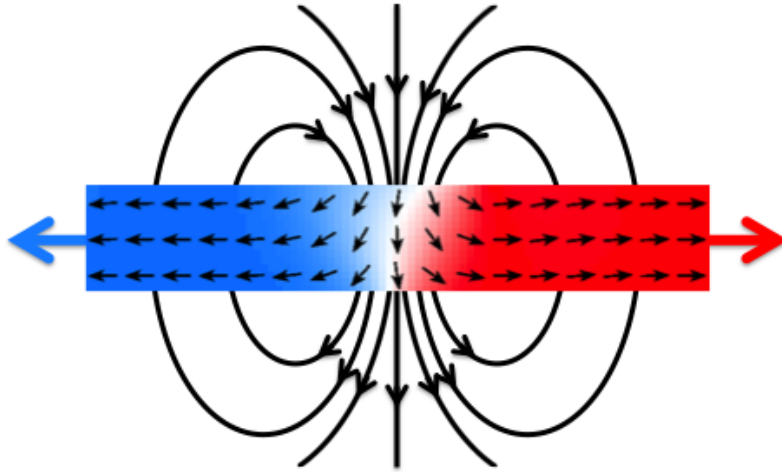
FIG. 1. Approximate stray field diagram of a domain wall on a ferromagnet model. The stray field due to moments outside

of the domain wall is omitted from the figure. Suppose the ferromagnet continues in $-\hat{x}$ and in $+\hat{x}$.

Using Maxwell's equation of magnetic fields, namely $\vec{\nabla} \cdot \mathbf{B} = 0$ for any magnetic field, and

by replacing the external field contribution by stray field contributions, we obtain

$$\vec{\nabla} \cdot (\mu_0(\mathbf{H}_{mag} + \mathbf{M})) = 0 \quad ,$$

from which we derive

$$\vec{\nabla} \cdot \mathbf{H}_{mag} = -\vec{\nabla} \cdot \mathbf{M} \quad .$$

This equation is important as it gives the relationship between magnetization and the magnetostatic field; the divergence of the magnetostatic field arises to cancel the divergence of the magnetization. Thinking of a point in space and its infinitesimally close surroundings in a sphere, the net flow of magnetostatic field vectors is into the sphere and the net flow of magnetization vectors is outwards.

For any magnetic field $\mathbf{B}$, we know that the potential energy stored in $\mathbf{B}$ is

$$U_B = \int \frac{\mathbf{B}^2}{2\mu_0} \, d\tau \quad .$$

For the derivation of U_B, see section III of this Appendix.

Similarly, we write for a magnetostatic field that

$$U_{mag} = \int \frac{\mu_0}{2} \, \mathbf{H}^2_{mag} \, d\tau \quad ,$$

where the integral is over all of space. We can specify this integral on the volume of the ferromagnet such that by combining it with $\mathbf{H}_{mag} = -\mathbf{M} + \mathbf{B}/\mu_0$ we obtain

$$U_{mag} = \frac{\mu_0}{2} \, \mathbf{H}_{mag} \cdot \left(\frac{\mathbf{B}}{\mu_0} - \mathbf{M} \right) d\tau \quad .$$

This becomes

$$U_{mag} = -\mu_0 \int \frac{1}{2} \, \mathbf{H}_{mag} \cdot \mathbf{M} \, d\tau \quad ,$$

where we assume along the ferromagnet that $\mathbf{B}$ is orthogonal to $\mathbf{H}_{mag}$.

F. I. Kaya ,   *Appendix A*

The *magnetostatic energy* (ME) of a system is minimized when the magnetization aligns with the stray field component; the stray field component tends to align with the boundaries of the ferromagnet unless there is a domain wall at which the stray field points outwards from the boundaries (as in Fig. 1). Thus, each domain wall has a high ME cost, whereas ME is minimized when moments align with the structure.

II. ADDITIONAL TOTAL ENERGY CONTRIBUTIONS

The complete *total energy* (TE) of the system is a sum of interactions within the material such that

$$E_{tot} = U_{exc} + U_{Zee} + U_{mag} + U_{ani} + U_{str} + U_{mst}   ,$$

where U_{exc} is the *exchange energy*, U_{Zee} is the *Zeeman* (or *external field*) *energy*, U_{mag} is the *magnetostatic* (or *stray field*) *energy*, U_{ani} is the *anisotropy energy*, U_{str} is the *external stress energy*, and U_{mst} is the *magnetostrictive energy.*[3]

As we have previously elaborated on the exchange, the Zeeman, and the magnetostatic energies, now we move forward to explain the anisotropy, the external stress, and the magnetostrictive energies.

A. Anisotropy Energy

The *Anisotropy energy* of a system depends on the alignment of moments with structural axes such as those of a crystal. We ignore the contribution of the anisotropy energy to the total energy since its contribution is small in comparison to that of the other three energy

terms for the Nickel-Iron (Ni-Fe) structures we consider.[1]

$$U_{ani} = \int F_{ani}(\mathbf{m}) \, d\tau \quad ,$$

where F_{ani} is the force created by all anisotrpic contributions.[3] It is a function of the magnetization direction, which is given by

$$\mathbf{m} = \mu_0 \frac{\mathbf{M}}{M_{sat}} \quad .$$

B.   Magneto-elastic Interactions

As we choose a Ni-Fe ferromagnet to study, we ignore all magneto-elastic contributions to the total energy. These include U_{str} and U_{mst}.

The *external stress energy* is

$$U_{str} = -\int \sigma_{ext} \cdot \vec{\varepsilon}^0(\mathbf{m}) \, d\tau \quad ,$$

where σ_{ext} is a symmetric tensor that accumulates stresses that are free of magnetic interactions, and where $\vec{\varepsilon}^0(\mathbf{m})$ is the free magneto-elastic deformation function. Hence, U_{str} embodies the energy due to a non-magnetic stress field.

The *magnetostrictive self energy* is

$$U_{mst} = \int \left(\frac{1}{2}(\mathbf{p}_e - \vec{\varepsilon}^0(\mathbf{m})) \cdot \mathbf{c} \cdot (\mathbf{p}_e - \vec{\varepsilon}^0(\mathbf{m})) \right) d\tau \quad ,$$

where $\mathbf{p}_e$ is an asymmetric tensor that indicates the distortion from the initial non-magnetic state, which tends to approach the free magneto-elastic deformation $\vec{\varepsilon}^0$,[3] and $\mathbf{c}$ is the elastic constant tensor. The double spatial terms in the integral account for non-local energy terms. They are needed in order to include the elastic interaction energies along all axes, hence to account for elastic-interaction torques on moments from all other moments.

III.   DERIVATION OF THE POTENTIAL ENERGY STORED IN A MAGNETIC FIELD

Consider a simple RL circuit, where the power supply (e.g., battery), a resistor, and an inductor are connected in series, in a closed loop.

The sum of potential differences equals zero by Kirchoff's 2nd rule such that

$$\varepsilon - iR - L\frac{di}{dt} = 0 \quad,$$

where ε is the emf of the power supply, i is the current that runs through the circuit, R is the resistance (of the resistor), L is the inductance (of the inductor), and t is time.

Multiplying each side by i, we get

$$i\varepsilon - i^2R - iL\frac{di}{dt} = 0 \quad.$$

In this latter equation,

$$i\varepsilon = \varepsilon\frac{dq}{dt}$$

is the rate at which the power supply feeds emf into the circuit; $\varepsilon \, dq$ equals the work done by the power supply. Moreover, i^2R corresponds to the dissipation rate of thermal energy, due to emf. The only term left is $iL\frac{di}{dt}$, corresponding thus to the rate at which energy is stored in the system as potential energy. This potential energy, U_B, is stored in the the magnetic field of the inductor, so that

$$\frac{dU_B}{dt} = iL\frac{di}{dt} \quad,$$

which implies

$$\int dU_B = \int iL \, di \quad,$$

9

and so

$$U_B = \frac{1}{2} i^2 L \quad .$$

The density of potential energy is therefore $u_B = U_B/V$, where V is the volume of the material.

If we consider a long solenoid with a cross-sectional area A, length l, and so volume $V = Al$, we can write the density as

$$u_B = \frac{U_B}{Al} = \frac{i^2 L}{2} \frac{1}{Al} \quad .$$

We can simplify this by substituting for L/l. In order to do this, let us consider the inductance of a solenoid inductor:

$$L = \frac{N\phi_B}{i} \quad ,$$

where $N = nl$ is the total number of turns of wire in the solenoid for n is the number of turns per length, and $\phi_B = BA$ is the magnetic flux through the central region of the solenoid for B is the magnetic field magnitude. In a solenoid, $B = \mu_0 i n$. Thus, we obtain

$$L = \frac{N\phi_B}{i} = \frac{nlBA}{i} = \frac{nl\mu_0 i n A}{i} = l\mu_0 n^2 A \quad ,$$

which implies

$$\frac{L}{l} = \mu_0 n^2 A \quad .$$

Now, substituting into u_B, we get

$$u_B = \frac{i^2}{2A} \frac{L}{l} = \frac{i^2}{2A} \mu_0 n^2 A = \frac{1}{2} i^2 \mu_0 n^2 = \frac{B^2}{2\mu_0} \quad .$$

Hence, we can obtain the the potential energy stored in a magnetic field such that

$$U_B = \int u_B \, d\tau = \int \frac{B^2}{2\mu_0} \, d\tau \quad .$$

F. I. Kaya ,   *Appendix A*

REFERENCES

[1]A. P. Guimaraes, *Principles of Nanomagnetism* (Springer, NY, USA, 2009).

[2]S. Blundell, *Magnetism in Condensed Matter* (Oxford University Press Inc., NY, USA, 2001).

[3]A. Hubert and R. Schafer, *Magnetic Domains* (Springer, NY, USA, 1998).

Appendix B: The Angle Finder

Fikriye Idil Kaya[1]

Department of Physics, Mount Holyoke College, South Hadley, MA, 01075,

USA

F. I. Kaya ,   *Appendix B*

This appendix explains how to run a sample *Angle Finder* code, which we use to plot angles of domain walls (DWs) on elliptical nanowires.

A sample Angle Finder MatLab code with the name K_angFinder.m can be accessed at:

\\ambr\faculty\kaidala\simulations\K\matlab_K

I. IMPORTING .OMF FILES ONTO MATLAB WORKSPACE

.omf is the type of the input files.

For .omf files in bulk:

To import files in bulk, we use the MatLab import code created by Jesica E. Bickel.

The steps to follow are:

- Copy all .omf files into a single folder.

  While doing this, make sure each folder has single geometry of ellipses (with constant A/B) and that the .omf files are in sequential order.

- Note the number of the last step of the .omf files.

  Assuming that in your folder you have .omf files that advance as ..., $*$_0338500.omf, $*$_0339000.omf, $*$_0339243.omf so that the $*$_0339243.omf is the last .omf file in your folder, the *last step no* is 339243.

- Note the *incrementation factor* for the remaining .omf step numbers.

  Note how many iterations go between two .omf files in your folder (except between the last .omf and the one previous to last if the last step number does not follow the

sequence); e.g., if the files listed in the folder are $*\_0333500$.omf, $*\_0334000$.omf,... and so on, then the *incrementation factor* is 500.

- Copy JEB_importfile.m into the same folder.

  You can find this code in \\ambr\faculty\kaidala\simulations\K\matlab_K

- Run JEB_importfile.m on MatLab.

  No modification is needed. The code will import all the .omf files in the folder onto the Workspace of Matlab, assigning them new names, e.g., data00, data01, etc..

- Note down the number of data files in the Workspace.

  Scroll the Workspace up or down to spot the data file with the highest number concatenated to the word 'data' in the Workspace. This number will be our *noDataMax*. Warning: The number usually does not correspond to the data number in the first or last line of the list in Workspace.

For fewer .omf files:

In times such that you only need to look at one .omf file and plot its angle, it may save time to import the .omf by hand (meaning, not by importfile.m).

The steps to follow are:

- Open the .omf using a simple text reader (I prefer Notepad++).

- Clip the header and the footer lines.

  This means delete the lines other than those of three digit vector coordinate lines; these non-vector lines are usually the first 38 and the last 3.

- Save the clipped file.

- Open MatLab and import the clipped .omf to MatLab Workspace.

  You can do this by drag & drop. Import as 'Matrix'. Check that the number of cells reported in 'Range:' is the same as the number of pixels in your .omf matrix (e.g., A1 to C450000 meaning 450,000 cells for ellipse with $A/B = 2$ and 300 pixels along the major axis).

- Rename the .omf matrix on Workspace.

  data00 if single file; data00, data01, etc. for multiple.

- Note down the number of data files in the Workspace.

  Scroll the Workspace up or down to spot the data file with the highest number concatenated to the word 'data' in the Workspace. This number will be our *noDataMax*. If the highest numbered data has name 'data05', for instance, then *noDataMax* is 5; if 'data12', then 12.

II.   MODIFYING THE CODE

Before we run the Angle Finder, here is how we open and modify it.

The steps to follow are:

- Copy K_angFinder.m into the folder you want to place the output in.

  You can find this code at \\ambr\faculty\kaidala\simulations\K\matlab_K

- Open K_angFinder.m on MatLab.

- Enter *noDataMax*.

  Edit lines 3 and 19. Edit line 18 to be *noDataMax+1*.

- Enter the *incrementation factor* and the *last step no.*

  Edit line 7 and line 21 respectively.

  If you are dealing with .omf files with random step numbers, then edit lines 6-27 accordingly.

- Enter the *A/B ratio.*

  Edit line 34 by entering the *A/B ratio* of the elliptical ferromagnets contained in the .omf files.

- Define the intended half of the ellipse, where the DW is located.

  There are two ways to do this: Either choose to work on vertical halves or on horizontal halves. Then, edit lines 158-190 by commenting out the code for the undesirable orientation.

- Enter the number of the intended elliptical half.

  Edit line 37. In the vertical orientation, 1 corresponds to the left half and 2 to the right half. In the horizontal orientation, 1 corresponds to the upper half and 2 to the lower half.

- Enter the number of the intended half of the width.

  Edit line 40. If this is set to 1, then the program will find the location of the magnetization in the z direction (which corresponds to the center of the DW and lets calculate the DW angle) on the outer half of the width of the elliptical ring.

- Enter the number of pixels along the x axis.

  Edit line 45.

- If running in bulk, then comment out lines 93-96.

This code plots the geometries with the DWs. When running in bulk, it may slow the program down.

- Run K_angFinder.m.

III.   INTERPRETING THE OUTPUT

Four .txt files will appear in the folder you run the K_angFinder.m:

- The coreAngleOutput.txt contains the step numbers, the DW angles, the x coordinates of *zMax*, which is the magnitude of the maximum magnetization in the z direction, the y coordinates of *zMax*, and the values of *zMax* pertaining to the .omf files in the Workspace, in this order in its columns.

- The coreSingleAngleOutput.txt contains the DW angles in a single column.

- The coreSingleXOutput.txt contains the x coordinates of *zMax* in a single column.

- The coreSingleYOutput.txt contains the y coordinates of *zMax* in a single column.

Appendix C: The Curvature Finder

Fikriye Idil Kaya[1]

Department of Physics, Mount Holyoke College, South Hadley, MA, 01075,

USA

(Dated: 28 Dec 2015)

F. I. Kaya ,   *Appendix C*

This appendix explains how to run a sample *Curvature Finder* code, which we use to obtain curvature values on elliptical nanowires, along Domain Walls (DWs).

The Curvature Finder calculates curvature as a function of DW angle, which is the angle along an elliptical nanowire at which a DW is located. It is implied that each elliptical nanowire has a constant A/B ratio within the work that has been done for this thesis.

A sample Curvature Finder MatLab code with the name K_curFinder.m can be accessed at:
\\ambr\faculty\kaidala\simulations\K\matlab_K

I.   IMPORTING ANGLE VALUES ONTO MATLAB WORKSPACE

The steps to follow are:

- Make a .txt file with numerical angle values in each line.

  We can either custom make one or use angles previously calculated by the Angle Finder. Let us choose the latter and use the curvatureOutput.txt file, which is outputted by the Angle Finder at each run.

- Open MatLab.

- Import the .txt to MatLab Workspace.

  You can do this by drag & drop. Import as 'Matrix'. Check that the number of cells reported in 'Range:' is the same as the number of pixels in your .omf (e.g., A1 to A600).

- Rename it on Workspace.

  daFile is the default name for the imported file matrix.

II.   MODIFYING THE CODE

Before we run the Curvature Finder, here is how we open and modify it.

The steps to follow are:

- Copy K_curFinder.m into the folder you want the output to be in.

  You can find this code at \\ambr\faculty\kaidala\simulations\K\matlab_K

- Open K_curFinder.m on MatLab.

- Enter A/B ratio.

  Edit line 2 by entering the *A/B ratio* of the elliptical nanowire in question.

- Run K_curFinder.m.

III.   INTERPRETING THE OUTPUT

A .txt file named 'curvatureOutput.txt' will appear in the folder, in which you run the K_curFinder.m. Each of its lines contains the curvature value at the angle that is given in the corresponding line of the .txt file.

Appendix D: The Energy Finder

Fikriye Idil Kaya[1]

Department of Physics, Mount Holyoke College, South Hadley, MA, 01075,

USA

F. I. Kaya ,   *Appendix D*

This appendix explains how to run a sample *Energy Finder* code, which we use to plot energies of the system in an elliptical nanowire.

A sample Energy Finder MatLab code with the name K_eneFinder.m can be accessed at:

\\ambr\faculty\kaidala\simulations\K\matlab_K

I.   BRIEF INTRODUCTION TO THE .ODT FILE

An .odt file contains information regarding the energies of the system at each step. In ascending order, each numeric line contains the energies of a single step, from step 0 to the last step. Columns 1, 7, 11, and 16 respectively correspond to *Total*, *Zeeman*, *Exchange*, and *Demagnetization* (a.k.a. *Magnetostatic*) Energies.

II.   IMPORTING AN .ODT FILE ONTO MATLAB WORKSPACE

The steps to follow are:

- Open the .odt using a simple text reader (I prefer Notepad++).

- Clip the header and the footer lines.

  This means delete the lines other than those of three digit vector coordinate lines; these non-vector lines are usually the the first 5 and the last 2 lines.

- Save the clipped file.

  E.g., save it as '[original filename]_clipped.odt' to distinguish it from the original file.

- Open MatLab.

- Import the clipped .odt to MatLab Workspace.

2

You can do this by drag & drop. Import as 'Matrix'. Check that the number of cells reported in 'Range:' is the same as the number of pixels in your .omf (e.g., A1 to X15445 including the energy information of all 15,445 steps).

- Rename it on Workspace.

  daFile is the default name for the imported file matrix.

III.   MODIFYING THE CODE

Before we run the Energy Finder, here is how we open and modify it.

The steps to follow are:

- Copy K_angFinder.m into the folder you want the output to be in.

  You can find this code at \\ambr\faculty\kaidala\simulations\K\matlab_K

- Open K_angFinder.m on MatLab.

- Run the code.

  This will generate the energy plot of all of the 100th time steps contained in the .odt file.

- (Zoom in)

  Fix the code using your MatLab skills in order to zoom in on the part of the graph you want.

Appendix E: OOMMF

Fikriye Idil Kaya[1]

Department of Physics, Mount Holyoke College, South Hadley, MA, 01075,

USA

F. I. Kaya ,   *Appendix E*

This appendix contains instructions for using OOMMF on a remote server (Harvard University's *Odyssey* cluster) and details of the input and output files.[1]

The instructions are user specific, in this case specific to me, and there may be ways easier than what I suggest.

I.   INSTRUCTIONS

To log into Odyssey on Mac:

- Run JAuth.jar on your computer.

  This will open an authenticator GUI that generates a six digit code that changes every minute and is in synchronization with only your personal password.

- Open a new *terminal* window on your Mac.

- Type in: ssh [your username]@odyssey.fas.harvard.edu

- Enter your password at the prompt 'Password:'.

- Enter the code on the authenticator GUI at the prompt 'Verification code:'.

  By now, you should be in your personal folder at Harvard's Odyssey cluster.

  A few explanations and shortcuts:

  To view your current directory, type 'ls'.

  To change directory, type 'cd [directory listed in your current directory]', or type 'cd ../' to go back to the encompassing directory.

  If the file has a beginning or ending that is unique among the other files in the same folder, instead of typing '[name of file]' you can simply type '*[the unique ending]',

type '[the unique beginning]*', or type '[the unique beginning]' and press **tab** on the keyboard. Examples: Type '*.mif' instead of 'reg.mif'. Instead: Type 'reg' and press **tab**.

To make a copy, type 'cp [copied file name] [name of the copy]' or 'cp [copied file's name] [address of target directory]/[copy's name]'.

To move a file from one directory to another, type 'mv [file name] [address of target directory]'.

To submit an OOMMF run at Odyssey:

- Log into Odyssey.

- Upload OOMMF.

  You can upload the modules of the version of the OOMMF you want by manually typing 'module load [name of the OOMMF module]' on the current directory, or you can go back to the home directory and edit the relevant code file to make Odyssey do it for you; see below for details.

- Create a folder for your run and copy the input files into this folder.

  See below for details on how to secure-copy files from your computer.

  It is prudent to have original input files from a run that worked before and then edit them on Odyssey via your terminal. This way, you will not generate sideline codes depending on the program that opens the input files.

- Edit your input files.

  Type 'emacs [name of file]'.

- Save the edited file.

  On your keyboard, simultaneously press **control**, **X**, and **S**.

- Exit the edited file.

  Simultaneously press **control**, **X**, and **C**.

- (Optional:) Get rid of the versions of the edited files that Odyssey saved for you, each with the name '[original file name]$\sim$'; e.g.' reg.mif$\sim$'.

- Submit the run.

  Type 'sbatch [name of your .sbatch file]'.

To automatically load the OOMMF modules in your directory at Odyssey:

- Log in to Odyssey.

- Go to your home directory.

  Type 'cd /'.

- Make a copy of the system file you are about to alter, for safety.

  Type 'cp .bashrc .bashrc-old3'.

- Open and edit the '.bashrc' file.

  At the end of the code line, add the module load commands: Type 'module load [the OOMMF module you want]'. Typically, you need multiple modules. Type the module load command for each additional module on a new line.

- Save and exit.

- Log out and log in to check that the process is complete.

  The module load commands should appear on the *terminal* window at login.

To secure-copy files from your computer to Odyssey or vice versa on Mac:

F. I. Kaya , *Appendix E*

- Open a new *terminal* window.

  E.g., if the terminal is already running, then simultaneously press **command** and **N**.

- Secure copy.

  Type in 'scp [address of the file(s) to be copied] [address of target directory]'.

  The address of your home directory at Odyssey is '[your username]@odyssey.fas.harvard.edu: /'.

- Enter your password at the prompt 'Password:'.

- Enter the code on the authenticator GUI at the prompt 'Verification code:'.

  Consequently, the details of the data transfer shall appear on your *terminal* window.

II.   INPUTS

A.   Mask

We call *mask* to the geometry of the ferromagnet you submit to OOMMF (Fig. 1). It is typically a bitmap image constructed in black and white, where the black codes for ferromagnetic portion and the white for non-magnetic.
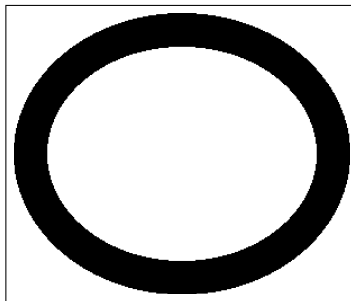

FIG. 1. Sample mask. The black portion is magnetized and white not magnetized. The black rectangular frame is added to show the mask boundaries and is not magnetized.

For details on how to make a mask, see Appendix *F*.

B.   .mif

The .mif file is where we detail the properties of the magnetic field we want to simulate and the ferromagnet that will be exposed to this field.

This .mif format is in Tcl/Tk and is specified for the intended OOMMF package.

For details, see the OOMMF User's Guide for the version you use.

You can find sample .mif files at

\\ambr\faculty\kaidala\simulations\K\odyssey_K

C.   .bsub

The .bsub file tells Odyssey how to run a simulation.

For details, see the Running Jobs section at the resources page of FAS at Harvard.[2]

D.   .omf

In order to run a simulation on an existing .omf file, we can include the .omf in the input and address it in the .mif code as input. This is useful, e.g., if the run times out before ending.

See next section for code details.

III.   OUTPUTS

The .err and .out appear as default outputs of Odyssey.

To obtain .odt, .omf, or .ohf outputs, you need to enter the relevant output request code into the .mif file.

A.   .err

This file details the errors that have occurred during the run if there are any.

B.   .out

This file details the simulation and whether or not it is complete. Depending on your .mif code, this file may contain some output data you have requested.

C.   .odt

This file gives a wide range of information for each time-step of the simulation, including energies, in a matrix format.

We only consider the columns that contain information on the Exchange, Zeeman, Magnetostatic, and Total energies.

For details on how to locate and compute the energies, see Appendix *D*.

F. I. Kaya , *Appendix E*

D.   .omf

This file gives the magnetization vectors in 3D, in a matrix format.

For details on how to plot the magnetization

by using OOMMF Tools, see Licht 2011;[3]

by using the MMM simulation on MatLab, see Goldman 2010;[4] or

by using MatLab, see Angle Finder in Appendix *B*.

E.   .ohf

This file gives field vectors in 3D, in a matrix format.

You can plot an .ohf file by using the same procedure you use to plot an .omf file, depending
on the field you require, e.g., demagnetization or Zeeman.

REFERENCES

[1]M. J. Donahue and D. G. Porter, *OOMMF User's Guide, Version 1.0* (Interagency Report
NISTIR 6376 (National Institute of Standards and Technology), MD, USA, 1999).

[2]Anon., *Running Jobs* (<https://rc.fas.harvard.edu/resources/running-jobs/>, accessed on
19 Dec. 2015).

[3]A. S. Licht, *A Computational Micromagnetic Study of Controlling Vortex Chirality in Ferromagnetic Nanorings* (Mount Holyoke College, 2011).

[4]A. Goldman, *Evolution of Magnetic States in Ferromagnetic Nanorings* (Mount Holyoke
College, 2011).

Appendix F: The Mask Maker

Fikriye Idil Kaya[1]

Department of Physics, Mount Holyoke College, South Hadley, MA, 01075,

USA

(Dated: 28 Dec 2015)

F. I. Kaya ,   *Appendix F*

This appendix explains how to run a sample Mask Maker code, which we use to create geometries, e.g. elliptical ring, for the ferromagnets that we feed into the simulation program, namely OOMMF.

A sample file with the name MaskEllipse.m can be accessed at:

\\ambr\faculty\kaidala\simulations\K\matlab_K

In the following sections we elaborate on what a mask is, how to design a mask, how to make a mask file, and how to convert the mask file into bitmap.

I.   SAMPLE MASK

A *mask* is a black and white image of the geometry we submit to OOMMF, on which black codes for magnetized and white for non-magnetized.

FIG. 1. Sample mask. The black portion is magnetized and white not magnetized. The black rectangular frame is added to show the mask boundaries and is not magnetized.

II.   DESIGNING A MASK

- Open a sample Mask Maker file on MatLab.

  E.g., open MaskEllipse.m at \\ambr\faculty\kaidala\simulations\K\matlab_K

- 'Save as' the program into your output folder, in which your mask will be located.

Make sure that the Mask Maker you are running is in the folder, in which you want your output folder to be, e.g., not in my server folder.

- Edit the mask.

  At this step, I suggest that you run the program once. By doing so, you can see the contemporary plot and then use your MatLab skill set to adjust the geometry to obtain the shape you desire.

III.   MAKING A MASK FILE

- Run the program.

  Just push play. This should generate a figure with the intended geometry that is rotated by 90° (the orientation will be fixed automatically, during the upcoming conversion procedure). Once run, the program will prompt you to enter a 'filename to save?'.

- Save the figure.

  Enter what you want the figure's name to be, e.g., 'ell3'. Do not type '.bmp' or any other file type specification after the 'filename to save'. At the completion of this step, the figure will be saved into the same folder as the Mask Maker.

IV.   CONVERTING TO BITMAP

These instructions are specific to Windows.

- Make sure *Perl* is installed in your computer.

- Copy 'data2bmp' and 'sample.bmp' from \\ambr\faculty\kaidala\simulations\K\maskMat into your output folder.

- Open Command Prompt and change directory to your output folder.

  Type 'cd Desktop\[address from Desktop to output folder]'.

- Run Perl.

  Type 'perl data2bmp' on Command Prompt.

- Enter the filename.

  At the prompt 'Enter the data file name:', type the filename of the MatLab figure; e.g., type 'ell3'. Hit enter.

- Enter '[filename].bmp'.

  At the prompt 'Enter the output ¡bitmap¿ file name:', type the mask's full bitmap name; e.g., type 'ell3.bmp'. Once you hit enter, the bitmap image of your mask, in the right orientation, shall appear in your output folder.